UNIVERSITY OF NOVA GORICA
GRADUATE SCHOOL

# INITIAL STAGES OF ORGANIC SEMICONDUCTOR THIN FILM GROWTH

DISSERTATION

**Primož Rebernik Ribič**

Mentor: Prof. Dr. Gvido Bratina

Nova Gorica, 2009

# Acknowledgments

I would like to thank my advisor Prof. Dr. Gvido Bratina for his guidance and support throughout my research. His suggestions regarding experimental design during our group meetings were particularly valuable.

I am grateful to Alen Batagelj, Andraž Petrović, Dr. Egon Pavlica, Mag. Peter Krkoč, and Dr. Polona Škraba for helpful discussions and for creating a friendly working atmosphere.

I would also like to thank the members of the Frisbie group at the Department of chemical engineering and materials science (CEMS), University of Minnesota, who provided me with the necessary training during my visit. Thanks to Prof. C. Daniel Frisbie for giving me the opportunity to visit his laboratory and for his guidance during my stay at CEMS.

I want to express my gratitude to my parents Smilja and Drago and to my girlfriend Mirjana for their unconditional support throughout my studies.

# Abstract

We investigated the growth of ultrathin organic semiconductor films on inorganic and organic substrates by atomic force microscopy (AFM). In the first part of the work emphasis was placed on growth of pentacene, 3,4,9,10-perylenetetracarboxylic dianhydride (PTCDA), rubrene, and $N,N'$-bis(3-methylphenyl)-$N,N'$-diphenylbenzidine (TPD) on vicinal (0001) sapphire surfaces with a terrace-and-step morphology. Sapphire surfaces with well-defined terraces separated by nanometer-size steps were obtained by annealing sapphire substrates at 1500°C for periods of up to 120 h. Our results show that the influence of the substrate features on the morphology of vacuum deposited organic thin films depends on the conformation of the organic molecule. In the case of planar molecules (pentacene and PTCDA), which nucleate in the form of two-dimensional (pentacene) or three-dimensional (PTCDA) islands, the surface steps act as preferred nucleation sites for these islands under suitable deposition conditions. Increasing the nominal thickness of the deposited material results in an increase of the average island size. In the case of pentacene the monolayer islands eventually coalesce and form a continuous pentacene film. The nucleation of subsequent pentacene layers also proceeds at the sapphire steps. In thicker PTCDA films there is no significant increase in the correlation between the island positions or orientations and the step direction. Steps on the sapphire surface have a more dramatic effect on the morphology of organic films in the case of non-planar rubrene and TPD molecules. Both TPD and rubrene nucleate in the form of three-dimensional islands. While TPD islands immediately assume positions at the sapphire steps, rubrene islands also nucleate on terraces. In both cases the morphology of the films evolves over time by ripening. The density of rubrene and TPD islands decreases with time while the average island size increases. Ripening of TPD islands is confined exclusively to the sapphire steps. On the other hand, rubrene islands that have nucleated on terraces decay while their material is incorporated into islands located at the steps. We found that the ripening rate of TPD is almost an order of magnitude faster than rubrene island ripening. We associate the faster ripening rate of TPD to the wealth of rotational degrees of freedom in TPD molecules as opposed to only a twisting degree of the tetracene backbone in rubrene. We achieved growth of wire-like linear structures with sub-micron lateral dimensions that follow the step direction on the sapphire surface by increasing the amount of deposited rubrene and TPD. Our results showed that these rubrene and TPD structures are unstable and eventually decay into three-dimensional islands with their centers at the sapphire steps. By studying the morphological time evolution of thin rubrene films on as-received sapphire substrates we found

that the process of island ripening is strongly temperature dependent. At 50°C, the process can be described by classical Ostwald ripening, with the interface transfer as the limiting mechanism. At room temperature, defects on the sapphire surface have a profound influence on the dynamics of the ripening process.

The second part of the work focused on deposition of monolayer and submonolayer pentacene films on organic polymeric substrates. Pentacene growth on polystyrene - PS, poly($\alpha$-methylstyrene) - P$\alpha$MS, and poly(methyl methacrylate) - PMMA was studied by tapping-mode AFM and transverse shear microscopy (TSM). For comparison we also performed growth studies of pentacene on $SiO_2$. In the submonolayer regime pentacene nucleates in the form of two-dimensional islands on hydrophilic surfaces (PMMA, $SiO_2$), while on hydrophobic surfaces (PS, P$\alpha$MS) we also observe a small fraction of three-dimensional nucleation at temperature above $\approx$ 30°C. The results show that, on all types of surfaces, there is a transition from the complete to the initially incomplete condensation regime at temperatures above $\approx$ 45°C. We calculated the activation energies for surface diffusion of pentacene molecules on all substrates. TSM was used to map individual crystalline grains in coalesced monolayer-thick pentacene films. We correlated the surface hydrophlicity of the substrate with the growth mode of pentacene. While on hydrophobic surfaces there is a transition from two-dimensional to three-dimensional growth at temperatures above $\sim$ 50°C, on hydrophilic surfaces smooth, continuous growth can be obtained even at temperatures as high as $\approx$ 65°C.

# Keywords

organic semiconductors, thin films, vicinal surfaces, thermal evaporation, organic molecular beam deposition, atomic force microscopy, transverse shear microscopy, nucleation, Ostwald ripening

# ZAČETNE FAZE RASTI TANKIH SLOJEV ORGANSKIH POLPREVODNIKOV

## Razširjen povzetek

### Uvod

Zaradi vedno večje težnje po miniaturizaciji elektronskih in optoelektronskih naprav, ki temeljijo na tankih slojih polprevodnikov, so se razvile metode, ki omogočajo natančen nadzor nad nanosom tankih polprevodniških plasti. Elektronske in optične lastnosti tankih polprevodniških slojev so v splošnem odvisne od njihove strukture in morfologije. Ena izmed obetavnih metod nanosa tankih slojev, ki sta jo v poznih šestdesetih letih 20. stoletja izumila J. R. Arthur in A. Y. Cho v Bellovih laboratorijih, se imenuje epitaksija z molekularnimi curki (ang. molecular beam epitaxy - MBE). Nanos tankih slojev polprevodnikov, kovin ali izolatorjev z MBE poteka v vakuumu. Pri tej metodi eden ali več curkov molekul ali atomov zadane podlogo (substrat), katere temperatura je ponavadi višja od sobne. Atomi oz. molekule lahko reagirajo med sabo ali s površino podloge, pri tem pa na podlogi nastane tanka urejena plast. Zaradi majhnih hitrosti rasti ($\sim$1 nm/s) lahko proces nadzorujemo na atomskem oz. molekularnem nivoju. MBE so najprej uporabili za preučevanje tankih slojev GaAs. Kasneje so s pomočjo MBE izdelali bolj zapletene polprevodniške heterostrukture, na katerih temelji večina današnjih elektronskih in optoelektronskih naprav.

Z odkritjem organskih polprevodnikov se je odprlo popolnoma novo raziskovalno področje. Potencialne prednosti organskih polprevodnikov pred anorganskimi so: nastavljiva valovna dolžina emisijskih črt v vidnem spektru, upogljivost tankih organskih slojev, enostaven način izdelave organskih elektronskih naprav, nizki stroški proizvodnje, itd. Širok emisijski spekter in visok izkoristek organskih svetlečih diod (ang. organic light emitting diode - OLED) sta že omogočila razvoj organskih svetlečih zaslonov, ki bodo lahko v prihodnosti zamenjali tekočekristalne zaslone. Gibljivost nosilcev naboja v organskih materialih je že dosegla gibljivost nosilcev naboja v amorfnih slo-

jih silicija, kar je omogočilo razvoj organskih tankoslojnih tranzistorjev (ang. organic thin-film transistor - OTFT). OLED in OTFT bodo v prihodnosti najverjetneje služili kot gradniki barvnih upogljivih zaslonov.

Podobno kot pri anorganskih polprevodnikih so elektronske in optične lastnosti tankih organskih slojev močno odvisne od njihove strukture ter morfologije. Metoda nanašanja tankih organskih slojev je odvisna predvsem od tipa organske molekule. Tanki polimerni sloji se običajno pripravijo z metodo kapljičastega nanašanja z vrtenjem (ang. spin coating), medtem ko tanke organske sloje iz aromatičnih ali heterocikličnih molekul običajno nanašamo z eno izmed metod parnega transporta kot je nanos organskega materiala z molekularnimi curki (ang. organic molecular beam deposition - OMBD). Kadar istočasno nanašamo na podlogo le en tip organskega materiala, namesto izraza OMBD uporabimo kar izraz naparevanje organskih slojev.

Pomemben korak pri proizvodnji elektronskih naprav je izdelava površinskih vzorcev (npr. elektrod, "eno" ali "nič-dimenzionalnih" struktur, itd.) na podlogah. Običajno ta poteka z metodo vrste "od zgoraj navzdol" (ang. top-down), kot sta litografija ali pisanje. Pisanje z elektronskim curkom (ang. electron-beam writing) in litografija z rentgenskimi žarki (ang. x-ray lithography) omogočata izdelavo površinskih vzorcev z dimenzijami pod 100 nm. Kljub temu bodo metode vrste "od zgoraj navzdol" v prihodnosti dosegle spodnjo fizikalno mejo velikosti vzorcev. V nasprotju s to tehniko, metoda "od spodaj navzgor" (ang. bottom-up) izkorišča samodejno ureditev atomov ali molekul v površinske strukture med nanosom materiala. Pri procesu samodejne ureditve atomov ali molekul v vzorce igra glavno vlogo difuzija atomov oz. molekul na površini podloge. Difuzija omogoča atomom ali molekulam, da najdejo mesta z najnižjo energijo, kar vodi v rast površinskih struktur, ki so odvisne od fizikalni in/ali kemijskih lastnosti podloge. Pri metodah "od spodaj navzgor" se spodnja fizikalna meja velikosti vzorcev približa velikosti samih atomov oz. molekul. Metoda, ki se izkorišča za rast nizko-dimenzionalnih anorganskih struktur in se šele v zadnjem obdobju uporablja za preučevanje organizacije organskih molekul na površinah, je nanos materiala na atomsko dobro-definirane površine (ang. atomically well-defined surfaces).

Jedro disertacije predstavljajo raziskave začetnih faz rasti tankih slojev organskih polprevodnikov na stopničastih površinah (ang. vicinal surface) safirja. Stopničasta površina je ena izmed vrste dobro-definiranih površin, za katero so značilne terase, ki so ravne na atomskem nivoju. Posamezne terase so med seboj ločene s stopnicami. Glavni cilj našega raziskovalnega dela je bil preučiti organizacijske lastnosti organskih molekul na stopničastih površinah safirja z orientacijo (0001).

Prednosti kot je npr. upogljivost tankih organskih slojev lahko v celoti izkoristimo le, če organske materiale nanašamo na upogljive podloge. V drugem delu naših raziskav smo se zato osredotočili na rast tankih slojev organskega polprevodnika pentacena na polimernih površinah. Preučili smo morfologijo in strukturo tankih slojev pentacena v odvisnosti od hitrosti nanašanja (naparevanja) in temperature podloge.

V drugem poglavju so predstavljene glavne fizikalne in strukturne lastnosti organskih materialov (3,4,9,10-perilen-dianhidrid-tetrakarboksilna kislina (PTCDA), pentacen, $N, N'$-bis(3-metilfenil)-$N, N'$-difenil benzidin (TPD) in rubren), ki smo jih uporabili v naših raziskavah.

V tretjem poglavju sta opisani dve glavni eksperimentalni metodi, s katerimi smo pripravili in karakterizirali vzorce. Tanke organske sloje smo nanesli z OMBD v vakuumski komori. Morfologijo in strukturo slojev smo preučili z mikroskopom na atomsko silo (ang. atomic force microscope - AFM). Večino eksperimentov smo opravili v Laboratoriju za epitaksijo in nanostrukture Univerze v Novi Gorici. Del eksperimentov, pri katerih smo preučevali rast pentacena na polimernih površinah, je bilo izvedenih na Oddelku za kemijski inženiring in znanosti o materialih, na Univerzi v Minnesoti (Department of chemical engineering and materials science, University of Minnesota), pod vodstvom prof. C. Daniela Frisbieja.

V četrtem poglavju so predstavljeni rezultati raziskav vpliva visokotemperaturnega segrevanja na morfologijo površine safirja z orientacijo (0001). Ugotovili smo, da lahko z izbiro primerne temperature in časa segrevanja dobimo dobro-definirane stopničaste površine s tipično širino terase nekaj 100 nm in tipično višino stopnice nekaj nm.

V petem poglavju sledijo preliminarni rezultati raziskav rasti organskega polprevodnika rubrena na stopničastih površinah safirja. Na podlagi AFM slik morfologije tankih slojev rubrena smo predlagali mehanizem organizacije molekul rubrena na stopnicah.

V naslednjih dveh poglavjih smo raziskave začetnih faz rasti tankih slojev organskih polprevodnikov razširili še na pentacen, PTCDA in TPD. Podrobno smo preučili vpliv temperature podloge in geometrijo organske molekule na morfologijo.

Osmo poglavje je namenjeno preučevanju časovne odvisnosti morfologije tankih slojev rubrena po končanem naparevanju. Sistematično smo raziskali zorenje otokov rubrena v odvisnosti od časa in temperature podloge.

V devetem poglavju so predstavljeni rezultati raziskav rasti pentacena na različnih polimernih podlogah. S pomočjo meritev gostote in pokritosti pentacenovih otokov v odvisnosti od temperature podlog smo identificirali režim kondenzacije in izračunali aktivacijske energije za difuzijo molekul na vseh vrstah podlog. Preučili smo tudi sloje pentacena debeline približno

ene molekularne plasti s pomočjo relativno nove eksperimentalne metode imenovane transverzalna strižna mikroskopija (transverse shear microscopy - TSM).

V zadnjem poglavju so podani zaključki in predlogi za nadaljnje poskuse, s katerimi bi lahko dosegli rast nanostrukturiranih vzorcev na površinah.

## Materiali

Pri raziskavah smo se osredotočili na rast tankih slojev pentacena, 3,4,9,10-perilen-dianhidrid-tetrakarboksilne kisline (PTCDA), $N, N'$-bis(3-metilfenil)--$N, N'$-difenil benzidina (TPD) in rubrena.

### PTCDA

PTCDA ($C_{24}H_8O_6$) je planarna molekula (Slika 2.1) velikosti 14.2 Å× 9.2 Å , z relativno molekulsko maso 392. Sestavlja jo pet benzenovih obročev, ki tvorijo perilenovo jedro, in dve anhidridni skupini na koncih molekule. V molekuli so zasedena elektronska stanja vse do najvišje zasedene molekulske orbitale (ang. highest occupied molecular orbital - HOMO). Molekulske orbitale nad HOMO so nezasedene. Najnižja nezasedena molekulska orbitala (lowest unoccupied molecular orbital - LUMO) je 2.48 eV nad HOMO. Kristalna struktura PTCDA je monoklinska (Slika 2.2). Obstajata dve znani modifikaciji kristalne strukture ($\alpha$ in $\beta$), s parametri osnovne celice, ki so podani v Tabeli 2.1. V obeh kristalnih strukturah se molekule uredijo v plasteh, ki so vzporedne z (102) kristalno ravnino. Razdalja $d_{102}$ med sosednjimi plastmi za obe kristalni strukturi je podana v Tabeli 2.1.

### Pentacen

Pentacen ($C_{22}H_{14}$) je planarna molekula z dimenzijami 14.21 Å × 5.04 Å in relativno molekulsko maso 278. Sestavljena je iz petih benzenovih obročev (Slika 2.3). Energijska razlika med HOMO in LUMO v kristalu pentacena znaša 2.2 eV. Kristalna struktura pentacena je triklinska (Slika 2.4). Obstajata dve znani modifikaciji kristalne strukture, s parametri osnovne celice, ki so podani v Tabeli 2.2. V obeh kristalnih strukturah se molekule uredijo v plasteh, ki so vzporedne z **ab** kristalno ravnino. Razdalja $d_{001}$ med sosednjimi plastmi za obe kristalni strukturi je podana v Tabeli 2.2.

### Rubren

Rubren ($C_{42}H_{28}$), v nasprotju s pentacenom in PTCDA, ni planarna molekula. Geometriji molekule v plinastem in trdnem stanju sta prikazani na

Sliki 2.5. Molekula je sestavljena iz tetracenove hrbtenice (štirje benzenovi obroči) in dveh fenilnih skupin na vsaki strani molekule. V plinastem stanju je tetracenova hrbtenica zvita (Slika 2.5(a)). Kristalna struktura rubrena je ortorombska (Slika 2.6), z dolžinami robov osnovne celice a = 14.44 Å, b = 7.18 Å in c = 26.97 Å . Molekule se uredijo v plasteh vzporednih z **ab** kristalno ravnino. Razdalja $d_{001}$ med sosednjimi plastmi je 1.34 nm.

### TPD

Geometrija molekule TPD ($C_{38}H_{32}N_2$) je tridimenzionalna (Slika 2.7). Sestavljena je iz osrednjega bifenilnega dela in štirih arilnih obročev. Bifenilni del je zvit, tako da je kot med dvema osrednjima aromatskima obročema enak 33.8°. Po drugi strani lahko na molekulo gledamo kot tvorbo iz dveh trifenilaminskih delov. Koti, ki jih oklepajo posamezne fenilne skupine z ravnino, ki jo določajo tri N-C vezi, so enaki 42.0°, 40.6° in 42.3°. Energijska razlika med HOMO in LUMO v TPD je enaka $\approx 3$ eV. Kristalna struktura TPD je ortorombska, z dolžinami robov osnovne celice a = 11.07 Å, b = 14.47 Å in c = 17.82 Å . V trdnem stanju se koti med različnimi aromatskimi obroči znatno spremenijo. Poleg tega v trdnem stanju obstajata dve različni konformaciji molekule.

## Eksperimentalne metode

### Nanos organskega materiala z molekularnimi curki

Pri nanosu organskega materiala je zaželeno, da je gostota nečistoč (molekul vode, kisika, itd.) v organski plasti čim manjša. Zaradi tega OMBD poteka v vakuumski komori pri tlakih od $\sim 10^{-5}$ Pa do $\sim 10^{-9}$ Pa. Shema vakuumske komore je prikazana na Sliki 3.1. Organski material (ponavadi v obliki prahu) vstavimo v celice, katerih temperaturo kontroliramo s pomočjo grelca in temperaturnega senzorja. Material segrejemo do sublimacijske temperature. Organske molekule v obliki curka zadenejo podlogo, na kateri se kondenzira tanek sloj organskega materiala. Debelino organske plasti merimo s kvarčnim merilnikom debeline. Čas naparevanja lahko natančno določimo s pomočjo zaslonke, ki lahko v relativno kratkem času prekine curek organskih molekul.

Pri naših raziskavah smo za nanašanje tankih organskih slojev uporabili vakuumsko komoro sestavljeno iz predkomore in glavne komore. Glavna komora je bila opremljena z dvema celicama in kvarčnim merilnikom debeline. Vsaka komora je bila povezana s svojim črpalnim sistemom, katerega sestavni del sta bili rotacijska in turbomolekularna črpalka. Komori sta bili med sabo

ločeni z ventilom. Tlak v glavni komori med naparevanjem je znašal okoli $\approx 1 \times 10^{-6}$ Pa ($\approx 1 \times 10^{-8}$ mbar). Nosilec s podlogami smo vstavili v predkomoro in ga prenesli v glavno komoro z magnetno roko. Na ta način smo v glavni komori lahko nepretrgoma vzdrževali visok vakuum. Nosilec vzorcev smo pritrdili na manipulator, ki je omogočal premikanje in rotacijo podlog okoli treh translacijskih in dveh rotacijskih osi. Na ta način smo lahko podloge postavili natančno pred curek molekul. Razdalja med odprtino celice in podlogo je bila okoli $\approx 10$ cm. V primeru polimernih podlog smo vzorce vstavili neposredno na nosilec v glavno komoro. Temperaturo podlog smo kontrolirali s pomočjo grelnega/hladilnega bloka, ki je bil pritrjen na nosilec vzorcev.

### Mikroskopija na atomsko silo

Mikroskopijo na atomsko silo (ang. atomic force microscopy - AFM) uporabljamo za karakterizacijo površin na nanometrski skali. Metoda temelji na merjenju sil med površino vzorca in ostro konico. Konica je pritrjena na en konec vzvoda, ki igra vlogo senzorja. Odklon vzvoda zaradi interakcije med površino in konico ponavadi merimo tako, da na vzvod svetimo z laserskim žarkom. Žarek se od vzvoda odbije pod določenim kotom, iz katerega lahko nato izračunamo odklon vzvoda. Shema merjenja odklona vzvoda je prikazana na Sliki 3.3. Obstaja več načinov mikroskopiranja z AFM, ki temeljijo na merjenju statičnega odklona vzvoda ali sprememb njegovih dinamičnih lastnosti (frekvence in amplitude nihanja), zaradi interakcije med konico in površino vzorca.

Pri kontaktnih načinih mikroskopiranja je konica mikroskopa ves čas v stiku s površino vzorca. V osnovnem kontaktnem načinu se konica mikroskopa premika po površini pri konstantnem odklonu vzvoda. Ko konica naleti na izboklino ali vdolbino na površini, se odklon vzvoda uporabi kot vhodni signal v povratno zanko. Povratna zanka je povezana s cevjo iz piezoelektrične snovi, ki premika vzorec v vertikalni smeri, dokler odklon vzvoda ne zavzame začetne vrednosti. Vertikalni premik vzorca nam da topografsko sliko površine.

Poleg osnovnega kontaktnega načina obstaja vrsta drugih načinov mikroskopiranja, s pomočjo katerih lahko izvemo pomembne podatke o površini vzorca. Eden izmed teh načinov je transverzalna strižna mikroskopija (ang. transverse shear microscopy - TSM). Pri TSM se konica premika po površini vzorca v smeri, ki je vzporedna daljši osi vzvoda. Zaradi strižnih sil med konico in površino vzorca pride do torzijskega zvijanja vzvoda okoli daljše osi. S pomočjo TSM lahko opazujemo orientacijo in obliko zrn v tankih polikristalnih organskih slojih oligoacenov. Metoda temelji na anizotropnih

elastičnih lastnostih teh materialov. Shema delovanja TSM je prikazana na Sliki 3.6.

Pri dinamičnih načinih mikroskopiranja je konica zelo kratek čas (ali pa sploh ni) v stiku s površino vzorca. Ta način mikroskopiranja se uporablja za karakterizacijo "mehkih" vzorcev kot so npr. tanke organske plasti in biološki vzorci. V dinamičnem načinu AFM je konica vzbujena, tako da niha s frekvenco, ki je blizu njene resonančne frekvence. Amplituda nihanja konice znaša od nekaj do nekaj deset nanometrov, tipična frekvence nihanja pa so od 100 do 400 kHz. Sliko topografije vzorca dobimo tako, da se konica pomika preko površine vzorca. Ko konica naleti na izboklino ali vdolbino na površini, se sprememba frekvence ali amplitude nihanja, zaradi spremembe razdalje med konico in površino, uporabi kot vhodni signal v povratno zanko. Povratna zanka je povezana s piezoelektrično cevjo, ki kontrolira razdaljo med površino in vzorcem. Kot pri kontaktnem načinu mikroskopiranja, nam tudi tukaj vertikalni premik vzorca da topografsko sliko površine. Dva glavna dinamična načina AFM sta nekontaktni način (ang. non-contact AFM (NC-AFM)) in dinamični kontaktni način (ang. intermittent contact AFM (IC-AFM) ali tapping AFM). Pri nekontaktnem načinu konica ne pride v stik s površino vzorca. Ta metoda se uporablja predvsem v vakuumu, kjer so možne natančne meritve premikov frekvence nihanja vzvoda. Pri običajnih pogojih mikroskopiranja na površini vzorca nastane plast vode, ki lahko povzroči pojav artefaktov v topografskih slikah. Temu se izognemo z dinamičnim kontaktnim načinom. Pri IC-AFM konica na koncu vsakega nihaja pride v stik s površino vzorca in prodre skozi plast vode.

Pri naših raziskavah smo za karakterizacijo vzorcev uporabili kontaktni način, TSM in dinamični kontaktni način. AFM slike morfologije tankih organskih slojev smo posneli v dinamičnem kontaktnem načinu z mikroskopom Veeco CPII. Za karakterizacijo slojev pentacena debeline natanko ene molekularne plasti pa smo uporabili TSM in kontaktni način mikroskopiranja. TSM slike so bile posnete z mikroskopom Veeco Nanoscope IIIA multimode AFM.

## Vpliv visokotemperaturnega segrevanja na morfologijo površine safirja z orientacijo (0001)

Z namenom, da bi dobili dobro-definirane površine, primerne za rast tankih organskih plasti, smo preučili vpliv visokotemperaturnega segrevanja na morfologijo (0001) površine safirja. Vzorce z orientacijo (0001) + $\beta$ ($\beta$=0.1° in 0.2°) proti [11$\bar{2}$0] smo segrevali na 1200 in 1500°C. Morfologijo vzorcev smo posneli z mikroskopom na atomsko silo v načinu IC-AFM.

Že na neobdelanih površinah so na obeh tipih vzorcev ($\beta$=0.1° in $\beta$=0.2°) prisotne terase, ki so ločene s stopnicami višine 0.21 nm (Slika 4.1), kar ustreza razdalji med sosednjima ravninama kisikovih atomov v monokristalu safirja. Robovi teras niso dobro definirani, poleg tega so na vzorcih prisotni defekti v obliki konic višine $\sim$ 1 nm. Širina terase na vzorcih z $\beta$=0.1° je enaka $(133 \pm 19)$ nm, na vzorcih z $\beta$=0.2° pa $(57 \pm 6)$ nm.

Po enournem segrevanju obeh tipov vzorcev na 1200°C postanejo robovi teras dobro definirani (Sliki 4.2 in 4.3). Na površini opazimo tudi lokalno združevanje stopnic višine 0.21 nm v stopnice, ki merijo v višino $i \times 0.21$ nm, kjer je $i$ celo število (tipično $2 \leq i \leq 7$). Na vzorcih z $\beta$=0.2° je združevanje stopnic prisotno na večjem delu površine. Pri obeh tipih vzorcev se na terasah, kjer pride do združevanja stopnic, pojavijo otoki, ki v višino merijo 0.2 ali 0.4 nm. Pojav združevanja stopnic in nastanka otokov pripisujemo transportu materiala z robov teras pravokotno na smer stopnic. Zaradi tega se nekatere terase zožijo, pri tem pa se sosednji stopnici združita. Material se lahko kondenzira v obliki otokov na terasah. Zaradi ožjih teras je na vzorcih z $\beta$=0.2° ta pojav hitrejši. Po štiriurnem segrevanju združevanje stopnic opazimo na celotni površini (Sliki 4.4 in 4.5(a)). Poveča se delež stopnic z višino 0.4 nm (na vzorcih z $\beta$=0.2° te stopnice prevladujejo), poleg tega se poveča tudi gostota otokov na terasah. Združevanje stopnic se kaže tudi v večanju povprečne širine terase. Po štiriurnem segrevanju opazimo, da na površini ni več stopnic z višino več kot $3 \times 0.21$ nm. To pomeni, da so višje stopnice, ki so bile prisotne le na majhnem deležu površine, razpadle na račun združevanja stopnic po celotni površini. Po šestnajsturnem segrevanju vzorcev z $\beta$=0.2° opazimo, da se pokritost površine z otoki močno zmanjša (Slika 4.5(b)). Otoki namreč začnejo razpadati. Material, ki pri tem nastane, se vgradi v terase. Zaradi vgradnje materiala v terase se pojavi tudi majhen delež stopnic z višino 0.21 nm, ki nekoliko zmanjšajo povprečno višino stopnice na površini. Kljub temu so po šestnajsturnem segrevanju na 1200°C na površini vzorcev v glavnem prisotne stopnice z višino 0.4 nm.

Pri segrevanju na 1500°C že po eni uri opazimo združevanje stopnic po celotni površini (Slika 4.6(a)). Zaradi povečane difuzije atomov na površini je povprečna višina stopnic (0.85 nm) večja kot pri segrevanju na 1200°C. Če vzorce segrevamo še dodatne 3 h, se povprečna višina stopnic še poveča (Slika 4.6(b)). Podobno kot pri vzorcih obdelanih na 1200°C se na terasah pojavijo otoki, ki pa po šestnajsturnem segrevanju razpadejo. Po razpadu otokov se povprečna višina stopnic zmanjša, podobno kot pri segrevanju vzorcev na 1200°C. Po šestnajsturnem segrevanju dobimo dobro-definirano površino; terase so ravne na atomskem nivoju in so ločene s stopnicami višine $i \times 0.21$ nm, kjer je $i$ celo število.

Rezultati kažejo na to, da je morfologija (0001) površine safirja pri segre-

vanju odvisna tako od temperature kot od časa segrevanja. Povprečna širina terase in višina stopnice naraščata z naraščajočo temperaturo segrevanja. Po drugi strani povprečna višina stopnice najprej naraste s časom segrevanja in nato po dolgem času pade. Takšno obnašanje je posledica razpada otokov in vgradnja nastalega materiala v terase.

## Rast nanožic rubrena na stopničastih površinah safirja

V tem poglavju so predstavljeni preliminarni rezultati raziskav rasti organskega polprevodnika rubrena na stopničastih površinah iz safirja. Vzorce safirja z orientacijo (0001) + 0.55° proti $[11\bar{2}0]$ smo predhodno segrevali na temperaturi 1500°C tudi po več deset ur. Površina safirja, ki smo ga segrevali 120 h na 1500°C, je prikazana na Sliki 5.1. Na vzorcu opazimo terase, ki so ravne na atomskem nivoju. Povprečna širina teras je 350 nm. Terase so med sabo ločene s stopnicami s povprečno višino 2.8 nm.

Na tako pripravljene površine smo z OMBD nanesli tanke sloje rubrena. Morfologija nominalno 10 nm debelega sloja rubrena, naparjenega pri hitrosti 1 nm/min, je prikazana na Sliki 5.2(a). Iz slike je razvidno, da stopničasta površina safirja deluje kot šablona za rast linearnih struktur v obliki žic. Na terasah lahko opazimo le majhno število tridimenzionalnih (3D) otokov rubrena. Tipična širina in višina struktur znašata 150 in 20 nm. Razdalja med sosednjima žicama je določena s povprečno širino terase (v našem primeru 350 nm). Na Slikah 5.2(b) in 5.2(c) (tridimenzionalni prikaz Slike 5.2(b)) si lahko podrobno ogledamo eno izmed žic, ki je prekinjena. Opazimo, da je večji del žice na nižji terasi.

Preferenčno nukleacijo rubrena na stopnicah lahko pojasnimo, če upoštevamo geometrijo molekule in morfologijo površine safirja. Monokristal safirja vzdolž smeri (0001) lahko opišemo kot zaporedje ravnin kisikovih atomov, ki so vstavljene med dve ravnini aluminijevih atomov. V osnovni celici safirja, ki v višino meri 1.3 nm, je 6 takšnih kisikovih ravnin. Pri segrevanju safirja na površini pride do združevanja stopnic, ki lahko v višino merijo tudi nekaj nm. Na ta način ob stopnicah pride do razkritja velikega števila ravnin kisikovih atomov. Kisikovi atomi ob stopnicah najverjetneje predstavljajo mesta, kamor se lahko vežejo fenilne skupine molekule rubrena. To ugotovitev potrjuje tudi dejstvo, da se večji del žice na Sliki 5.2(b) nahaja na nižji terasi, kjer molekule rubrena lahko pridejo v stik s kisikovimi atomi.

Ugotovili smo, da se molekule rubrena vežejo tudi na defekte na površini safirja. Na Sliki 5.3 je prikazana površina podloge iz safirja, ki smo jo segrevali 100 h na 1500°C. Na podlogi so poleg teras in stopnic tudi otoki (v nadaljnjem besedilu defekti) s tipičnim premerom nekaj deset nm in tipično višino od 1 do 1.5 nm. Morfologija tankega sloja rubrena, ki smo ga naparili na takšno

podlogo je prikazana na Sliki 5.4. Poleg že znanih rubrenovih žic na sliki opazimo tudi večje število 3D otokov rubrena, ki so najverjetneje posledica nukleacije na defektih.

## Vpliv morfologije podloge na rast tankih organskih slojev

V tem poglavju bomo primerjali morfologiji tankih slojev pentacena in rubrena na stopničastih površinah safirja. Podloge safirja, z orientacijo (0001) + 0.55° (0.20°) proti $[11\bar{2}0]$, smo pred nanašanjem organskega sloja segrevali od 72 do 120 h na 1500°C. Tipična morfologija površine safirja po segrevanju je prikazana na Sliki 6.1. Na safirju so prisotne terase, ki so ravne na atomskem nivoju. Terase so med sabo ločene s stopnicami, ki v višino tipično merijo nekaj nm. Tipične širine teras so nekaj 100 nm.

Na takšne podloge smo naparili sloje pentacena z nominalno debelino 0.5 nm (Slika 6.2). Nominalna hitrost naparevanja je znašala 0.5 nm/min. Za tako tanke sloje pentacena je značilna nukleacija dvodimenzionalnih (2D) otokov, ki v višino merijo $\approx 1.5$ nm. Ta višina se relativno dobro ujema z dolžino molekule pentacena, kar pomeni, da molekule v otokih na površini safirja zavzamejo pokončen položaj. Otoki pentacena prekrivajo manjši delež površine safirja ($\sim 1/3$). Iz Slike 6.2 je razvidno, da so središča večine otokov na stopnicah, kar pomeni, da stopnice predstavljajo preferenčna nukleacijska mesta za molekule pentacena. Morfologija nominalno 1.7 nm debelega sloja pentacena je prikazana na Sliki 6.3. Iz slike je razvidno, da se 2D otoki prve plasti pentacena združijo (puščica 1). Otoki v drugi plasti so večji, kot otoki v prvi plasti. Opazimo, da stopnice predstavljajo tudi nukleacijska mesta za tretjo (puščica 2) in višje (puščica 3) plasti pentacena.

Kot smo ugotovili že v prejšnjem poglavju, imajo stopnice večji vpliv na morfologijo rubrena. Rubren raste v obliki linearnih struktur (žic), ki so vzporedne s stopnicami (Slika 6.4(a)). V primeru sloja debeline 10 nm so tipične širine in višine teh struktur enake 150 in 20 nm, medtem ko je razdalja med njimi določena s širino terase. Iz Slik 6.4(b) in 6.4(c) ugotovimo, da se nukleacija žic prične ob stopnicah.

Vzrok za različni morfologiji pentacena in rubrena sta različni geometriji molekul. Medtem, ko je pentacen planarna molekula, je geometrija molekule rubrena 3D (Slika 6.5). Molekule pentacena difundirajo po površini, dokler ne najdejo mesta z lokalno najnižjo energijo, kjer se prične nukleacija. Preferenčna nukleacijska mesta so stopnice na površini safirja. Po začetni fazi nukleacije se molekule raje vežejo na obstoječe otoke kot pa na stopnice. Vzrok je večja interakcija (najverjetneje zaradi relativno dobrega prekriva-

nja $\pi$ orbital med sosednjimi molekulami pentacena v otoku) med molekulo in otokom kot med molekulo in stopnico. Z večanjem debeline naparjenega materiala otoki rastejo, se začnejo stikati in se nazadnje združijo. Nukleacija višjih plasti poteka podobno. Po drugi strani se molekule rubrena preko fenilnih skupin vežejo na stopnice. Relativno močna interakcija med molekulami rubrena in stopnicami je vzrok za rast linearnih struktur, ki so vzporedne s stopnicami.

## Začetne faze rasti organskih polprevodnikov na stopničastih površinah safirja

Raziskave iz prejšnjih dveh poglavij smo razširili še na rast PTCDA in TPD. Kot bodo pokazali rezultati, igra geometrija molekule ključno vlogo pri začetnih fazah nukleacije organskih slojev na stopničastih površinah safirja. Podloge safirja smo ponovno pripravili z visokotemperaturnim segrevanjem (72 do 120 h na 1500°C).

V prvem delu bomo opisali začetne faze rasti tankih slojev iz 2D molekul (pentacen, PTCDA). Morfologija 0.5 nm debelega sloja pentacena v odvisnosti od temperature podloge je prikazana na Sliki 7.1. Nominalna hitrost naparevanja je znašala 0.3 nm/min. Opazimo, da stopnice predstavljajo preferenčna nukleacijska mesta za 2D otoke pentacena pri vseh temperaturah podloge. Višina otokov znaša $(1.7 \pm 0.3)$ nm, kar ustreza pokončni legi molekul v otokih. Iz zaporedja Slik 7.1(a), (b) in (c) je razvidno, da gostota otokov pentacena pada z naraščajočo temperaturo. Pri višjih temperaturah so nekateri otoki podaljšani v smeri stopnic. Pri debelejših slojih pride do združevanja 2D otokov prve plasti pentacena (puščica 1 na Sliki 7.2). Stopnice predstavljajo nukleacijska mesta tudi za tretjo (puščica 2) in višje (puščica 3) plasti pentacena.

Stopnice na površini safirja imajo manjši vpliv na nukleacijo tankih slojev PTCDA. Morfologija nominalno 0.3 nm debelega sloja PTCDA, naparjenega pri 0.7 nm/min in sobni temperaturi podloge, je prikazana na Sliki 7.3. Za PTCDA je značilna nukleacija 3D otokov. Pri sobni temperaturi je nukleacija naključna, kar pomeni, da stopnice ne predstavljajo preferenčna nukleacijska mesta, kot se je izkazalo v primeru pentacena. Z višanjem temperature podloge se situacija spremeni. Slika 7.4 prikazuje morfologijo slojev PTCDA z nominalno debelino 0.3 nm, 1.6 nm in 3.3 nm, naparjenih pri temperaturi podloge 135°C in hitrosti 0.7 nm/min. Opazimo, da pri tankih slojih (0.3 nm) nukleacija večine otokov poteka na stopnicah. Z večanjem debeline pride tudi do nukleacije na terasah. Otoki z večanjem debeline naparjenega materiala rastejo. Pri debelini 3.3 nm opazimo tudi podolgovate otoke. Ti

otoki rastejo v smereh, ki niso vzporedne ali pa so celo pravokotne na smer stopnic.

Pri tankih slojih iz 3D molekul opazimo drugačno morfologijo kot v primeru pentacena in PTCDA. Morfologija 2.3 nm debelega sloja rubrena, naparjenega pri sobni temperaturi podloge in hitrosti 0.3 nm/min, je prikazana na Sliki 7.5. Morfologija na Sliki 7.5(a) je bila posneta 30 min po naparevanju. Na površini opazimo 3D otoke rubrena. Nukleacija je skoraj naključna po celotni površini, kljub temu opazimo znake preferenčne nukleacije na stopnicah. Iz zaporedja Slik 7.5(a), (b) in (c) je razvidno, da se morfologija rubrena s časom spreminja. Gostota otokov s časom pada, njihova povprečna velikost pa narašča. Količina materiala na površini se s časom ne spreminja. Temu pojavu pravimo zorenje otokov. Po 23,5 h (Slika 7.5(b)) so vsi otoki rubrena na stopnicah. Po 48 h se morfologija rubrena stabilizira. Z večanjem debeline naparjenega materiala se 3D otoki rubrena združijo v linearne strukture, ki rastejo ob stopnicah (Slika 7.6). Takoj po naparevanju je znaten delež materiala tudi na terasah. Po nekaj urah pa molekule rubrena zavzamejo položaje izključno ob stopnicah. Linearne strukture s časom razpadejo v 3D otoke, katerih središča so na stopnicah.

Podoben proces nukleacije kot pri rubrenu opazimo tudi pri TPD. Morfologija 0.3 nm debelega sloja TPD, naparjenega pri sobni temperaturi podloge in hitrosti 0.6 nm/min, je prikazana na Sliki 7.7(a). Slika je bila posneta 20 min po naparevanju. Opazimo, da otoki TPD takoj zavzamejo položaje na stopnicah. Zaporedje Slik 7.7(a), (b) in (c) prikazuje zorenje otokov TPD s časom. Zorenje poteka izključno ob stopnicah na površini safirja. Iz Slike 7.7 je razvidno, da je zorenje otokov za red velikosti hitrejše kot v primeru rubrena. Z večanjem debeline naparjenega materiala se 3D otoki združijo v linearne strukture, ki rastejo ob stopnicah (Slika 7.8). Pri nominalni debelini sloja 2.8 nm sta tipična višina in širina struktur enaka 100 in 6 nm. Linearne strukture s časom razpadejo v 3D otoke, katerih središča so na stopnicah.

Ena izmed glavnih razlik v morfologijah različnih organskih slojev je način nukleacije (2D pri pentacenu in 3D pri PTCDA, rubrenu in TPD). To razliko lahko pojasnimo s predpostavko, da je v primeru 2D nukleacije interakcija molekul s površino večja v primerjavi z interakcijo med molekulami v sosednjih molekularnih plasteh. Pod drugi strani je pri 3D nukleaciji medmolekulska interakcija večja kot interakcija molekule s površino podloge. Očiten je tudi različen vpliv stopnic na morfologijo različnih organskih slojev. V začetnih fazah rasti stopnice predstavljajo preferenčna nukleacijska mesta za molekule pentacena. Kasneje se molekule, zaradi relativno šibke interakcije s stopnicami, raje vežejo na že obstoječe otoke. Za razliko od pentacena, molekule PTCDA pri sobni temperaturi podloge niso dovolj gibljive, da bi našle lokalno najnižja energijska stanja na površini. Pri povišani temperaturi pod-

loge se poveča difuzija molekul PTCDA po površini. Molekule dosežejo stopnice, ki predstavljajo preferenčna nukleacijska mesta. Pri večanju količine naparjenega materiala se molekule, podobno kot v primeru pentacena, raje vežejo na že obstoječe otoke. Na nadaljnjo rast otokov ne vpliva več interakcija s stopnicami ampak relativno močnejše medmolekulske sile. Pri rubrenu in TPD je situacija drugačna. Obe molekuli se relativno prosto gibljeta po površini, dokler ne naletita na stopnice, kjer se začne nukleacija otokov. 3D geometrija rubrena in TPD najverjetneje omogoča nastanek dodatnih vezi med molekulo in stopnico. V primeru rubrena nukleacija otokov poteka tudi na terasah, vendar otoki, ki pri tem nastanejo, niso stabilni. Njihov material se s časom vgradi v otoke na stopnicah. Ti otoki so zaradi relativno močne interakcije molekul s stopnicami bolj stabilni. Zorenje otokov je po eni strani znak visoke gibljivosti molekul po površini, po drugi strani pa kaže na to, da so molekule relativno šibko vezane na površino 3D otokov. Hitrejše zorenje otokov TPD pripisujemo večjemu številu rotacijskih prostostnih stopenj v molekuli TPD, v primerjavi z molekulo rubrena, kjer pride samo do zvijanja tetracenove hrbtenice.

## Zorenje otokov rubrena

V nadaljevanju si bomo podrobno ogledali proces zorenja otokov rubrena na safirju. Da bi se izognili preferenčni nukleaciji otokov na stopnicah, smo uporabili neobdelane podloge safirja. Opazovali smo časovno odvisnost morfologije nominalno 1.6 nm debelih slojev rubrena pri 50°C in sobni temperaturi podloge.

Na Sliki 8.1 je prikazana odvisnost morfologije tankega sloja rubrena od časa, ki je pretekel od naparevanja. Temperatura vzorca med opazovanjem je bila 50°C. Za proces nukleacije rubrena so značilni 3D otoki. Iz slike je razvidno, da se gostota otokov s časom manjša, medtem ko njihova povprečna velikost narašča. Na Sliki 8.2 je prikazana časovna odvisnost gostote otokov rubrena za vzorec, ki je bil ves čas opazovanja na 50°C in za vzorec, ki je bil med opazovanjem na sobni temperaturi. Polna črta je rezultat numeričnega prilagajanja enačbe $\rho(t) \propto t^{-1}$ na krivuljo časovne odvisnosti gostote otokov rubrena za vzorec pri 50°C. Koeficient $a = 1.05 \pm 0.02$ je zelo blizu teoretični vrednosti $a = 1$, ki velja za klasično Ostwaldovo zorenje, pri katerem je limitni proces odcepitev molekul rubrena s površine otokov. Otoki s polmerom večjim od kritičnega polmera rastejo, medte ko otoki s polmerom manjšim od kritičnega razpadejo, njihov material pa se vgradi v večje otoke. Kritični polmer s časom raste in je odvisen od povprečne koncentracije prostih molekul na površini in od koncentracije molekul ob otokih.

Pri vzorcu, ki je bil med opazovanjem na sobni temperaturi, zorenje ne

moremo opisati z enostavnim modelom $\rho(t) \propto t^{-1}$. Iz grafa na Sliki 8.2 vidimo, da se gostota otokov na začetku relativno počasi spreminja, po $\approx 7$ h pa začne hitro padati ($\sim 3$ krat hitreje kot v primeru vzorca pri 50°C). Vzrok za tako obnašanje so najverjetneje defekti na površini safirja. Pri sobni temperaturi defekti vplivajo na nukleacijo otokov. Iz Slike 8.3(b) je razvidno, da je po $\approx 30$ h večji del velikih otokov rubrena na defektih, ki jih na AFM sliki površine opazimo v obliki ravnih ali rahlo ukrivljenih črt. Ti defekti, katerih globina lahko sega tudi do 1 nm, so najverjetneje posledica poliranja površine safirja. Defekti predstavljajo preferenčna nukleacijska mesta za molekule rubrena. Večina otokov na defektih je stabilna in s časom rastejo. Ko kritični polmer postane večji od tipičnega polmera otokov, ki niso nastali na defektih, začnejo ti otoki hitreje razpadati. To se odraža v hitrem padanju gostote otokov s časom po $\approx 7$ h.

Vpliv površinskih defektov na proces zorenja otokov se odraža tudi v časovni odvisnosti porazdelitve velikosti otokov (Slika 8.4). Pri sobni temperaturi je ob času 1,67 h porazdelitev otokov po velikosti skoraj simetrična, po 7,33 h pa se vrh porazdelitve pomakne k manjšim polmerom. To pomeni, da se po $\approx 7$ h pojavi večje število manjših otokov na površini safirja. Ker je njihov polmer manjši od kritičnega, ti otoki hitro razpadejo, kar se kaže v nenadnem padcu gostote otokov s časom po $\approx 7$ h. Po drugi strani porazdelitev otokov po velikosti pri 50°C s časom ohranja obliko, kar je značilno za Ostwaldovo zorenje.

## Rast ultratankih slojev pentacena na polimernih podlogah

V nadaljnjih raziskavah smo se osredotočili na rast tankih slojev organskega polprevodnika pentacena na naslednjih polimernih podlogah: polistiren - PS, poli($\alpha$-metilstiren) - P$\alpha$MS in poli(metil metakrilat) - PMMA. Za primerjavo smo preučili tudi rast pentacena na $SiO_2$.

Za vse podloge smo izračunali površinske energije z merjenjem kontaktnih kotov različnih tekočin na površini (Tabela 9.1). V Tabeli 9.1 so podani tudi kontaktni koti vode na vseh površinah. Glede na kontaktni kot vode bomo površine razvrstili v dve skupini: hidrofilne površine - sem spadata PMMA in $SiO_2$, ter hidrofobne površine - sem spadata PS in P$\alpha$MS. S pomočjo IC-AFM mikroskopije smo izmerili tudi površinsko hrapavost (ang. root-mean-square roughness oz. RMS roughness) podlog in ugotovili, da je za vse polimerne podloge enaka $2.8 \pm 0.1$ Å. Po drugi strani je hrapavost $SiO_2$ podlog nekoliko manjša in znaša $2.1 \pm 0.1$ Å.

Slika 9.1 prikazuje morfologije 0.4 nm debelih slojev pentacena, napar-

jenih pri temperaturi podloge 30°C in hitrosti 0.4 nm/min, na PS, P$\alpha$MS, PMMA in $SiO_2$. Na vseh podlogah opazimo nukleacijo 2D otokov pentacena s povprečno višino 1.5 nm. Otoki so bolj kompaktni na PS in PMMA v primerjavi z otoki na P$\alpha$MS in $SiO_2$, kar je znak, da je na PS in PMMA difuzija molekul ob robovih otokov hitrejša kot na P$\alpha$MS in $SiO_2$. Zaradi hitrejše difuzije molekule najdejo energijsko bolj ugodna mesta ob robovih otokov, ki so zaradi tega bolj kompaktni. Najmanjšo gostoto otokov opazimo na $SiO_2$, temu sledita PS in P$\alpha$MS. Gostota otokov je največja na PMMA. Na vseh polimernih podlogah opazimo majhno število 3D otokov.

Na vseh podlogah smo izmerili temperaturno odvisnost pokritosti prve in višjih plasti pentacena ter temperaturno odvisnost gostote otokov v območju od 10°C do 60°C, pri hitrosti naparevanja 0.4 nm/min. Pokritost prve plasti predstavlja pokritost površine z otoki, medtem ko je pokritost višjih plasti merilo za stopnjo 3D nukleacije. Rezultati so prikazani na Sliki 9.2. Iz grafa na Sliki 9.2(a) vidimo, da se na vseh podlogah v temperaturnem območju od 10°C do 45°C pokritost prve plasti počasi spreminja s temperaturo. Pokritost je zaradi različnih kemijskih lastnosti površin manjša na hidrofobnih podlogah v primerjavi s hidrofilnimi podlogami. Po drugi strani začne pokritost prve plasti močno padati, če temperaturo podlog dvignemo nad $\approx$ 45°C. Pri temperaturi okoli 70°C pokritost pade na nič (ni prikazano na grafu). Pokritost druge in višjih plasti pentacena je na hidrofilnih podlogah konstantna na celem temperaturnem območju ($\approx 0$). Pokritost nekoliko naraste pri temperaturah pod $\approx$ 20°C, kar kaže na to, da se na hidrofilnih površinah 3D otoki pojavijo zaradi nukleacije na defektih. Po drugi strani na hidrofobnih podlogah (posebej na P$\alpha$MS) pokritost druge in višjih plasti začne naraščati pri temperaturi večji od $\approx$ 30°C. Nukleacija 3D otokov na hidrofobnih površinah pri višjih temperaturah je znak, da je interakcija pentacena s temi površinami manjša kot interakcija pentacena s hidrofilnimi površinami. To je nekoliko v nasprotju s podatki v Tabeli 9.1, iz katerih bi pričakovali, da je interakcija pentacena s P$\alpha$MS večja kot s PMMA, vendar moramo imeti v mislih, da so absolutne napake površinskih energij v Tabeli 9.1 relativno velike. Poleg tega je površinska energija makroskopska količina, ki nam ne pove dosti o obnašanju molekul na površini na mikroskopski skali.

Iz grafa na Sliki 9.2(b) vidimo, da gostota otokov pentacena hitro pada s temperaturo. Eksperimentalni podatki se ujemajo z matematičnim modelom, ki ga je razvil J. A. Venables s sodelavci. Ta pravi, da se gostota otokov spreminja s hitrostojo naparevanja $R$ in temperaturo podloge $T_S$ po Enačbi 9.1, kjer je $k_B$ Boltzmannova konstanta, $E_{Nucl}$ pa aktivacijska energija za nukleacijo, ki je odvisna od aktivacijskih energij za različne procese na površini (difuzija - $E_{diff}$, desorbcija - $E_A$ in nastanek otoka s kritično velikostjo $i$ z vezavno energijo $E_i$). Tako $E_{Nucl}$ kot $\delta$ sta odvisna od režima

kondenzacije (J. A. Venables in ostali), kritične velikosti otoka (otok z $i+1$ molekulami je stabilen) in dimenzionalnosti otokov (2D ali 3D). Iz grafa na Sliki 9.2(a) sklepamo, da je v območju od 10°C do 45°C desorbcija molekul zanemarljiva. Kadar lahko desorbcijo molekul s površine zanemarimo, lahko nukleacijo opišemo z modelom popolne kondenzacije. V režimu popolne kondenzacije molekule, ki prispejo na podlogo, po njej difundirajo, dokler ne naletijo na stabilen otok, na katerega se vežejo. V tem režimu (v primeru 2D nukleacije) za $E_{Nucl}$ velja Enačba 9.2. $E_{Nucl}$ dobimo s prilagajanjem Enačbe 9.1 na eksperimentalne podatke temperaturne odvisnosti gostote otokov pentacena v območju od 10°C do 45°C (nukleacijske energije $E_{Nucl}$ v območju od 10°C do 45°C so podane na Sliki 9.2(b)). Ob predpostavkah, da je $i = 3$ (R. Ruiz in ostali, B. Stadlobler in ostali) in $E_i = 892$ meV (V. Kalihari in ostali), lahko izračunamo aktivacijske energije za difuzijo molekul pentacena na vseh podlogah. Rezultati so podani v Tabeli 9.2.

V režimu popolne kondenzacije (2D nukleacija) je $\delta = i/(i+2)$, kar znaša 0.6 za $i = 3$. Da bi preverili predpostavko $i = 3$, smo eksponent $\delta$ določili eksperimentalno z merjenjem gostote otokov pentacena v odvisnosti od hitrosti naparevanja pri temperaturi podloge 30°C (Slika 9.3). Kritične eksponente za vse podloge smo izračunali s prilagajanjem Enačbe 9.1 na eksperimentalne podatke. Dobili smo vrednosti od 0.67 do 0.80, ki se približno ujemajo s teoretično vrednostjo 0.6 za $i = 3$.

Z višanjem temperature podlog nad $\approx 45$°C se aktivacijske energije spremenijo (Slika 9.2(b)). Sprememba aktivacijskih energij je tudi znak spremembe režima kondenzacije. Iz grafa na Sliki 9.2(a) je razvidno, da se nad $\approx 45$°C zmanjša pokritost površine z otoki pentacena. Iz tega sklepamo, da desorbcija igra pomembno vlogo, kar je značilno za režim začetno nepopolne kondenzacije. Iz grafa na Sliki 9.2(b) dobimo le grobe ocene (na grafu so le tri točke) aktivacijskih energij za nukleacijo $E_{Nucl}$ v območju od 45°C do 60°C (1360 meV za PS, 710 meV za P$\alpha$MS, 1150 meV za PMMA in 1470 meV za $SiO_2$). V režimu začetne nepopolne kondenzacije $E_{Nucl}$ zapišemo z Enačbo 9.3, kjer je $E_A$ aktivacijska energija za desorbcijo. S pomočjo zgornjih podatkov dobimo naslednje grobe ocene $E_A$ za različne podloge: 610 meV za PS, 180 meV za P$\alpha$MS, 470 meV za PMMA in 680 meV za $SiO_2$. Kljub temu, da gre za grobe ocene, se najmanjša $E_A$ za P$\alpha$MS ujema s predpostavko relativno majhne interakcije pentacena s P$\alpha$MS, ki je vzrok za pojav 3D otokov pentacena pri višjih temperaturah. Kontroliranje gostote otokov v debelejših slojih pentacena je pomembno iz tehnološkega vidika, saj lahko meje med kristalnimi zrni vplivajo na transport električnega naboja po tankih organskih plasteh. Videli smo, da lahko gostoto otokov kontroliramo s spreminjanjem temperature podloge in hitrosti naparevanja. Višja gostota otokov na PMMA v primerjavi s PS in P$\alpha$MS je najverjetneje posle-

dica različnih aktivacijskih energij za difuzijo molekul pentacena in različnih kemijskih struktur površin. Po drugi strani je vzrok za najmanjšo gostoto otokov na $SiO_2$ verjetno manjša hrapavost površin v primerjavi s polimernimi podlogami.

Z večanjem debeline naparjenega materiala se 2D otoki pentacena združijo. Sloje pentacena debeline približno ene molekularne plasti na različnih podlogah smo preučili z metodo TSM. Rezultati so prikazani na Sliki 9.4. Medtem, ko nam topografija ne da skoraj nobenih podatkov o prvi plasti pentacena (levi stolpec slik), lahko na TSM slikah (desni stolpec slik) vidimo posamezna kristalna zrna pentacena. Kontrast v TSM slikah nam da informacijo o orientaciji posameznih kristalnih zrn. V primeru pentacena je kristalografska smer [110] ($[1\bar{1}0]$) najsvetlejših (najtemnejših) zrn vzporedna s smerjo premikanja konice med mikroskopiranjem (horizontalna smer). Vmesni kontrasti zrn ustrezajo primerom, ko je vektor premikanja konice poravnan vzdolž ene izmed vmesnih smeri med [110] in $[1\bar{1}0]$ kristalografskima smerema. Na TSM slikah opazimo največja zrna na $SiO_2$, temu pa sledita P$\alpha$MS in PMMA. Rezultati se ujemajo z grafom na Sliki 9.2, kjer smo najmanjšo gostoto otokov opazili na $SiO_2$, največjo pa na PMMA.

Preučili smo tudi vpliv hidrofilnosti površine na rast eno molekularno plast debelih slojev pentacena. Medtem ko pri temperaturi podloge 50°C (pri hitrosti naparevanja 0.4 nm/min) še dobimo gladke nepretrgane sloje pentacena na vseh podlogah, z višanjem temperature na okoli 65°C na hidrofobnih podlogah pride do 3D nukleacije pentacena. Primerjava rasti pentacena na hidrofobnem P$\alpha$MS in hidrofilnem PMMA je podana na Sliki 9.5. V primeru P$\alpha$MS prva plast pentacena ne prekrije celotne površine podloge. Po drugi strani na PMMA tudi pri 65°C dobimo relativno gladek sloj pentacena. Ti rezultati prav tako potrdijo ugotovitev, da je interakcija molekule pentacena s hidrofilnimi površinami večja kot interakcija pentacena s hidrofobnimi površinami.

## Zaključki

V prvem delu raziskav smo se osredotočili na preučevanje vpliva morfologije podlog na rast tankih slojev organskih polprevodnikov. Za podloge smo izbrali stopničaste površine monokristala safirja z orientacijo (0001).

Z namenom, da bi dobili dobro-definirane površine, smo podloge safirja segrevali na visoki temperaturi. Rezultati naših raziskav vpliva visokotemperaturnega segrevanja safirja na njegovo morfologijo so pokazali, da je morfologija močno odvisna od časa in temperature segrevanja. Po enournem segrevanju površine safirja na 1200°C, pride do lokalnega združevanja stopnic in nastanka otokov na terasah. Po daljšem času segrevanja otoki razpadejo,

pri tem pa se njihov material vgradi v terase. Pri segrevanju na 1500°C že po eni uri pride do združevanja stopnic po celotni površini podloge. Tudi pri 1500°C se pojavijo otoki, ki po daljšem času segrevanja razpadejo. Povprečna višina stopnice in širina terase naraščata z naraščajočo temperaturo segrevanja. Podloge, ki smo jih uporabili za preučevanje rasti tankih organskih slojev, smo predhodno segrevali na 1500°C tudi do 120 h, z namenom da bi dobili široke dobro-definirane terase, ki so ločene s stopnicami višine nekaj nanometrov.

Preliminarne raziskave rasti smo opravili na organskem polprevodniku rubrenu. Ugotovili smo, da stopnice na površini safirja služijo kot šablona za rast linearnih struktur oz. žic rubrena s submikronskimi prečnimi dimenzijami. Vzrok za takšno rast smo pripisali tridimenzionalni geometriji molekule rubrena.

Raziskave smo razširili še na pentacen, PTCDA in TPD. Ugotovili smo, da geometrija molekule igra ključno vlogo v začetnih fazah rasti tankih organskih slojev. V primeru pentacena in PTCDA, ki sta planarni molekuli, stopnice predstavljajo preferenčna nukleacijska mesta pri ustreznih pogojih naparevanja. Kljub temu je interakcija molekul pentacena in PTCDA s stopnicami relativno šibka, saj pri večjih debelinah naparjenega materiala na rast močno vplivajo relativno močnejše medmolekulske sile. Po drugi strani stopničaste površine safirja močno vplivajo na morfologijo slojev TPD in rubrena. Molekuli rubrena in TPD sta relativno dobro gibljivi po površini, kar jima omogoča najti energijsko najugodnejša mesta za vezavo. Zaradi njune tridimenzionalne geometrije pride do tvorbe dodatnih vezi med molekulo in stopnicami. Pri manjših količinah naparjenega materiala pride do nukleacije tridimenzionalnih otokov, ki v primeru TPD takoj zavzamejo položaje na stopnicah. Nukleacija otokov rubrena poteka tudi na terasah, vendar ti otoki niso stabilni. S časom razpadejo, njihov material pa se vgradi v otoke na stopnicah. Pri večjih debelinah naparjenega TPD oz. rubrena se otoki združijo v linearne strukture, ki so vzporedne s smerjo stopnic. Te strukture s časom razpadejo v tridimenzionalne otoke s središči na stopnicah. Ugotovili smo, da se morfologija tankih slojev rubrena in TPD spreminja s časom zaradi zorenja. Hitrejše zorenje v primeru TPD smo pripisali večjemu številu rotacijskih prostostnih stopenj molekule v primerjavi z molekulo rubrena.

Podrobno smo raziskali zorenje otokov rubrena na neobdelanih površinah safirja. Ugotovili smo, da gostota otokov s časom pada, medtem ko njihova povprečna velikost raste. Rezultati so pokazali, da lahko pojav pri temperaturi podloge 50°C opišemo s klasičnim Ostwaldovim zorenjem. Pri sobni temperaturi podloge defekti pomembno vplivajo na dinamiko procesa.

Pokazali smo, da je vpliv stopničastih podlog na morfologijo organskih slojev močno odvisen od geometrije organske molekule. Predlagamo, da se

prihodnje raziskave osredotočijo na iskanje ustreznih molekul, ki bi lahko vodile v rast stabilnih vzorcev na površinah. Električne meritve na teh strukturah bi lahko nato opravili s prevodnim načinom AFM. Alternativna metoda, ki postaja vse bolj popularna, je funkcionalizacija molekul. Pritrditev funkcionalnih skupin, npr. na oba konca planarne molekule, bi lahko vodila v rast eno-dimenzionalnih struktur na površini. Slaba stran te metode je možen negativen vpliv funkcionalnih skupin na transport naboja po takšnih strukturah.

V zadnjem delu smo se osredotočili na rast tankih slojev pentacena na polistirenu - PS, poli($\alpha$-metilstirenu) - P$\alpha$MS in poli(metil metakrilatu) - PMMA. Za primerjavo smo preučili tudi rast pentacena na $SiO_2$. Za sloje debeline okoli 0.5 nm je značilna nukleacija dvodimenzionalnih otokov na vseh podlogah. Na hidrofobnih podlogah se pri temperaturah večjih od $\approx$ 30°C pojavi tudi znaten delež tridimenzionalnih otokov pentacena. Iz grafov temperaturne odvisnosti pokritosti in gostote otokov smo ugotovili, da pride do prehoda iz režima popolne kondenzacije v režim začetne nepopolne kondenzacije pri temperaturi nad $\approx$ 45°C. Izračunali smo aktivacijske energije za difuzijo molekul pentacena na vseh tipih površin. S pomočjo transverzalne strižne mikroskopije smo ugotovili, da lahko pri ustreznih pogojih naparevanja dobimo gladke, eno molekularno plast debele, polikristalne sloje pentacena na vseh podlogah. Rezultati so pokazali, da na hidrofobnih površinah pri višjih temperaturah podloge ($\approx$ 65°C) pride do prehoda iz dvodimenzionalne v tridimenzionalno rast. Pri takšni rasti prvi sloj pentacena ne prekrije celotne površine podloge. Po drugi strani lahko na hidrofilnih podlogah pri $\approx$ 65°C še vedno dobimo gladke, eno molekularno plast debele sloje pentacena.


# Ključne besede

organski polprevodniki, tanke plasti, stopničaste površine, naparevanje, epitaksija z molekularnimi curki, mikroskopija na atomsko silo, transverzalna strižna mikroskopija, nukleacija, Ostwaldovo zorenje

# Contents

# 1 Introduction

The increasing trend towards miniaturization of electronic and optoelectronic devices based on thin layers of semiconductors has led to the development of methods that allow precise control of semiconductor thin film deposition throughout the fabrication process. The electronic and optical properties of thin semiconductor films are in general governed by their structure and morphology. In the past decades, several techniques were employed to achieve control over the growth of thin semiconductor films. One of the most promising techniques, invented in the late 1960s by J. R. Arthur and A. Y. Cho of the Bell Labs, is called molecular beam epitaxy (MBE). MBE is a versatile tool for growing thin epitaxial structures made of semiconductors, metals or insulators [1, 2] (and references therein). In MBE, one or several beams of thermal-energy atoms or molecules strike the surface of a substrate, which is maintained at an elevated temperature in an ultrahigh vacuum environment. The atoms or molecules may react with each other and with the substrate surface, forming smooth and ordered films. Relatively slow growth rates ($\sim$1 monolayer/s) allow the growth process to be controlled on an atomic or molecular level. Growth techniques based on particle beams were first used to investigate thin layers of inorganic semiconductors like GaAs. The precision of the growth process allowed fabrication of more complex semiconductor heterostructures which form the basis of almost all modern electronic and optoelectronic devices.

The discovery of organic materials with semiconducting properties opened up a number of promising research opportunities. The primary motivation for investigating the electronic and optical properties of organic materials was that they could offer several advantages over their inorganic counterparts, such as: mechanical flexibility, emission tunable over the visible spectrum, ease of fabrication of organic electronic devices, and low fabrication costs. Tunable emission and high electroluminescence efficiency of organic light emitting diodes (OLEDs) has led to the development of organic light emitting displays, which may, in the near future, replace liquid crystal displays (LCDs). Organic materials with charge carrier mobilities comparable

to that of amorphous silicon are already being used as active layers in organic thin films transistors (OTFTs). In the near future, OLEDs and OTFTs will probably serve as the main building blocks of color flexible displays.

As with inorganic thin films, the electronic and optical properties of organic thin films heavily depend on their structural and morphological properties. Preparation of thin organic films depends on the type of the organic molecule. While thin polymer films are usually prepared from solutions by dip or spin-coating, thin films consisting of low-molecular weight aromatic or heterocyclic molecules are usually grown by a vapor transport method such as organic molecular beam deposition (OMBD). OMBD is an analogous technique to MBE and is used to control the growth process of organic thin films on a molecular level [3].

An important step in production of electronic devices is reproducible fabrication of surface patterns (e.g. contact electrodes, "one" or "zero-dimensional" structures, etc.) on substrates. Surface patterns are traditionally created with "top-down" techniques like lithography or writing. At present, sophisticated methods such as electron-beam writing and x-ray lithography allow fabrication of surface structures with dimension bellow 100 nm [4]. These techniques, however, will eventually reach their fundamental limits. In contrast to "top-down" methods which are based on fabrication of surface patterns, "bottom-up" methods take advantage of spontaneous organization of atoms or molecules into surface structures during deposition of the material. One of the key factors that influences the process of organization of molecules into structures is surface diffusion. The diffusion of molecules on the substrate surface allows them to find minimum surface energy sites which leads to growth of structures that depend on the physical and/or chemical properties of the substrate surface. In the case of "bottom-up" techniques the fundamental size limit of surface structures decreases down to the size of the molecules themselves. A method that is used to grow low-dimensional inorganic structures and is only recently being employed to study the organizational properties of organic molecules is deposition of molecules onto atomically well-defined surfaces [5] (and references therein).

At the core of this work are studies of initial stages of growth of thin organic films on vicinal surfaces of sapphire single crystal. Vicinal sapphire surfaces are regarded as a type of atomically well-defined surfaces that are characterized by atomically flat terraces, which are separated by steps. The main goal of this work was to study the influence of the terrace-and-step morphology of vicinal (0001) sapphire surfaces on the organizational properties of organic molecules.

In order to fully take advantage of the mechanical flexibility of organic materials these have to be deposited on organic substrates. The second part

of the thesis therefore focuses on the growth of thin organic films of pentacene on polymeric substrates. The structure and morphology of the films are discussed as a function of deposition rate and substrate temperature.

After the first chapter the thesis is organized as follows. The second chapter gives an overview of the basic properties of organic compounds that were used in this work. The physical and structural properties of pentacene, 3,4,9,10-perylenetetracarboxylic dianhydride (PTCDA), 5,6,11,12-tetraphenylnaphthacene (rubrene), and $N,N'$-bis(3-methylphenyl)-$N,N'$-diphenylbenzidine (TPD) and their bulk crystal phases are described.

The third chapter outlines the two main experimental methods that were used to prepare and characterize the samples. Thin organic films of pentacene, PTCDA, rubrene, and TPD were grown by OMBD in a custom made vacuum chamber. The main experimental tool that was used to characterize the substrates and the organic films was the atomic force microscope (AFM) which was operated either in contact or intermittent-contact mode. The majority of experiments were performed at the Laboratory for epitaxy and nanostructures, University of Nova Gorica. Part of the experiments involving growth and characterization of pentacene films on polymeric substrates were carried out at the Department of chemical engineering and materials science, University of Minnesota, under the supervision of Prof. C. Daniel Frisbie.

In the fourth chapter a detailed study of the behavior of the (0001) surface of sapphire upon high temperature annealing is presented [6]. The established annealing protocols allow preparation of substrates with well-defined surfaces that are characterized by atomically flat terraces separated by steps. The effect of the annealing temperature and annealing time on the average terrace width and step height is discussed.

The fifth chapter is dedicated to preliminary results obtained on growth of thin rubrene films on vicinal sapphire surfaces [7]. A qualitative mechanism of organization of rubrene molecules at the sapphire steps is proposed.

In the following two chapters the study of initial stages of growth of organic semiconductors on vicinal sapphire surfaces is extended to pentacene, PTCDA, and TPD [8, 9]. The effects of deposition rate, substrate temperature, and the conformation of the organic molecule on the morphology of the films are presented.

Chapter 8 is dedicated to the investigation of post-growth morphological evolution of thin rubrene films on as-received sapphire surfaces [10]. For the first time the ripening process in thin organic films is systematically studied as a function of time and temperature.

Chapter 9 deals with the results of pentacene growth on polymeric substrates. By measuring the monolayer island densities and coverages as a function of substrate temperature the condensation regime is identified and

the activation energies for surface diffusion of pentacene molecules on different types of substrates are calculated. The structure of completely coalesced pentacene islands is investigated by a novel contact AFM technique called transverse shear microscopy (TSM).

In the last chapter the results of the work are summarized. Suggestions for future experiments which would further exploit the possibilities of growing tailor-made organic nanostructures on surfaces are given.

# 2 Materials

This chapter outlines the basic properties of the four organic compounds that were used in our thin film growth studies: PTCDA, pentacene, rubrene, and TPD. It focuses on the structural properties of the molecules and their bulk crystal phases.

## 2.1 PTCDA

3,4,9,10-perylenetetracarboxylic dianhydride (PTCDA) has been used as a model organic compound in studies of epitaxial growth of thin organic films. It forms thin crystalline films on a variety of metal, semiconductor, and insulator surfaces [11–17].

PTCDA is an aromatic molecule that consist of five benzene rings which form a perylene core and one anhydride group at each end of the molecule (Figure 2.1). The chemical formula of PTCDA is $C_{24}H_8O_6$. It is a planar molecule with dimensions of 14.2 Å$\times$ 9.2 Å [17]. Electrons in the molecule occupy molecular orbitals up to the highest occupied molecular orbital (HOMO). The orbitals above HOMO are unoccupied. The lowest unoccupied molecular orbital (LUMO) is 2.48 eV above HOMO [18].

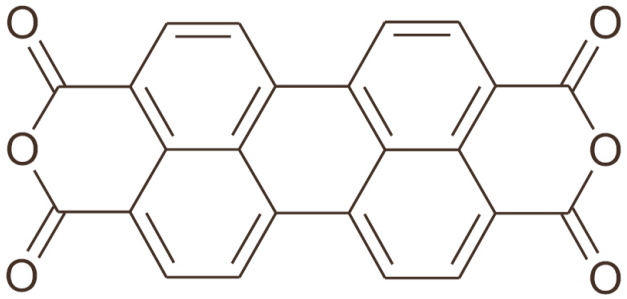


**Figure 2.1:** Structural formula of the PTCDA molecule. The molecule consists of five benzene rings and two anhydride groups at its ends. It is a planar molecule with a relative molecular mass of $M = 392$.

The bulk crystal structure of PTCDA is monoclinic (Figure 2.2). There are two known modifications of the crystal structure, namely the $\alpha$ polymorph and the $\beta$ polymorph. Their unit cell parameters are listed in Table 2.1. The molecules in both polymorphs arrange in the (102) planes in a herringbone pattern and form a layered structure with an interplanar distance $d_{102}$ which is given in Table 2.1.

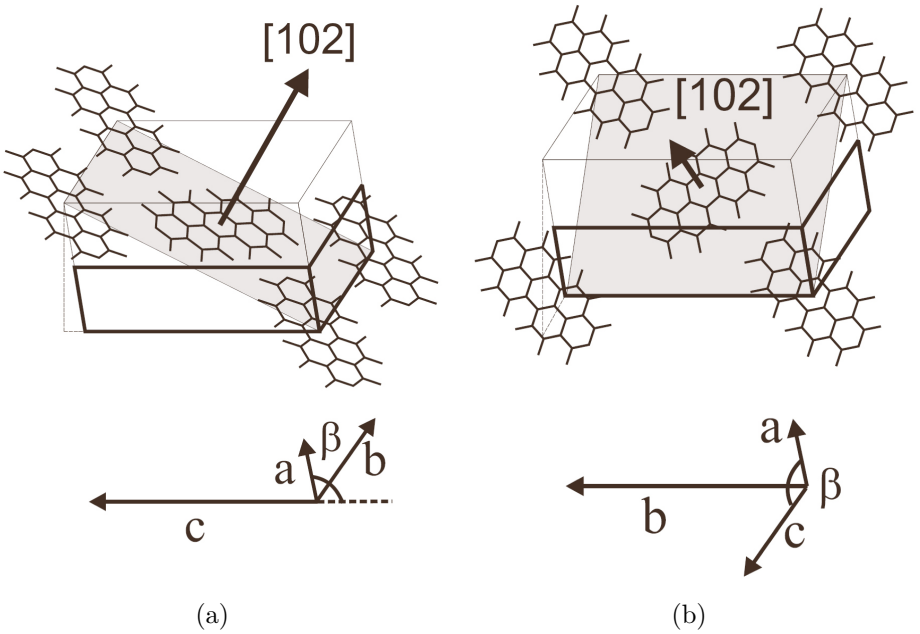


**Figure 2.2:** (a) Unit cell of the $\alpha$ polymorph, and (b) unit cell of the $\beta$ polymorph of bulk PTCDA. The (102) plane indicated in the figure coincides with the molecular plane. The images were taken from Ref.[19].

| polymorph | $a$ [Å] | $b$ [Å] | $c$ [Å] | $\beta$ [°] | $d_{102}$ [Å] |
|---|---|---|---|---|---|
| $\alpha$ [11, 20] | 3.74 | 11.96 | 17.34 | 98.8 | 3.23 |
| $\beta$ [19, 21] | 3.87 | 19.3 | 10.77 | 83.5 | 3.25 |

**Table 2.1:** Unit cell parameters of the $\alpha$ and $\beta$ polymorph of bulk PTCDA.

## 2.2 Pentacene

Pentacene ($C_{22}H_{14}$) stands out as one of the most promising candidates for applications in organic thin film transistors (OTFTs) because of its high charge carrier mobility exceeding 1 $cm^2/Vs$ [22, 23]. The mobility of pentacene is therefore comparable to that of amorphous silicon, which is currently used in low-cost electronic devices.

Pentacene, like PTCDA, is also a planar molecule with dimensions of 14.21 Å × 5.04 Å [24]. The structural formula of pentacene is shown in Figure 2.3. The energy gap between HOMO and LUMO in solid pentacene, based on the photoconductivity data [25], is 2.2 eV.

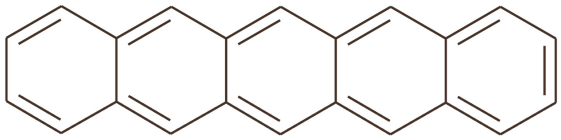

**Figure 2.3:** Structural formula of pentacene. The molecule consists of five benzene rings and has a relative molecular mass of $M = 278$.

Pentacene is known to form ordered crystalline or polycrystalline films on various substrates such as metals [26, 27], semiconductors [28], and insulators [29, 30].

The bulk crystal structure of pentacene is triclinic. There are two known modifications of the crystal structure with the unit cell parameters listed in Table 2.2. In the crystal structure reported by Campbell *et al.* [31], pentacene molecules arrange themselves in a herringbone pattern in the **ab** crystallographic plane and form a layered structure along the **c** crystallographic axis with an interplanar distance $d_{001}$ of 1.45 nm. The structure reported by Mattheus *et al.* [32] has interchanged **a** and **b** axes and an interplanar distance of 1.41 nm. Both crystal structures of pentacene are shown in Figure 2.4.

| reported in | $a$ [Å] | $b$ [Å] | $c$ [Å] | $\alpha$ [°] | $\beta$ [°] | $\gamma$ [°] | $d_{001}$ [nm] |
|---|---|---|---|---|---|---|---|
| [31] | 7.93 | 6.14 | 16.03 | 101.9 | 112.6 | 85.8 | 1.45 |
| [32] | 6.266 | 7.775 | 14.53 | 76.475 | 87.682 | 84.684 | 1.41 |

**Table 2.2:** Unit cell parameters of the two crystal structures of pentacene.

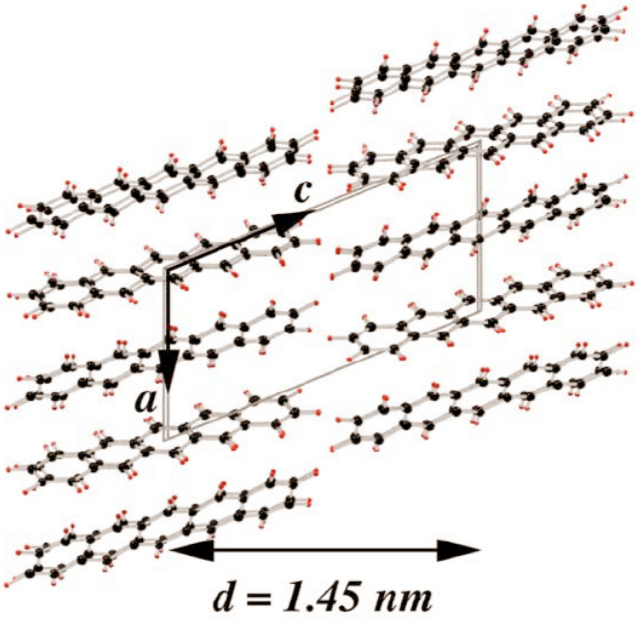


(a)

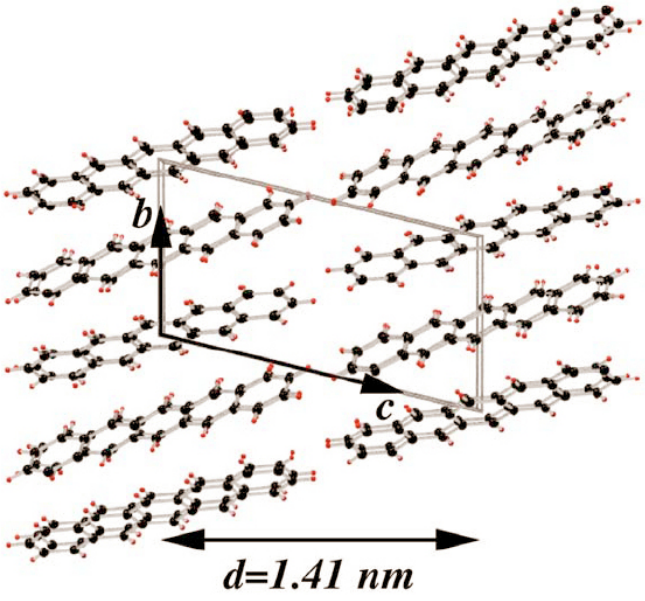


(b)

**Figure 2.4:** The crystal structure of pentacene reported in (a) [31] and (b) in [32]. The images were taken from Ref.[33].

## 2.3 Rubrene

The use of high mobility organic materials in electronic devices is essential if we wish to consider practical applications of these devices. Researchers have recently focused on rubrene, which shows promise for applications in organic electronics. Rubrene single crystal field effect transistors (FETs) were reported to exhibit mobilities on the order of 10 $cm^2/Vs$ [34, 35].

Although growth of crystalline films of rubrene by OMBD may be a difficult task due to the different geometries of the rubrene molecule in the gas and solid phases [36, 37], it has been recently suggested that the use of a pentacene buffer layer and an atomically flat substrate may improve crystal properties of rubrene thin films [38].

In contrast to PTCDA and pentacene, rubrene ($C_{42}H_{28}$) is not a planar molecule. Molecular geometries of rubrene in the gas and solid phases are shown in Figure 2.5. In the gas phase, the tetracene-backbone (four benzene rings) has a twisted geometry, resulting in axial chirality as indicated in Figure 2.5(a). In the solid phase, rubrene molecules lose their chirality [39]. The calculated energy difference between HOMO and LUMO in rubrene is 2.6 eV [40].

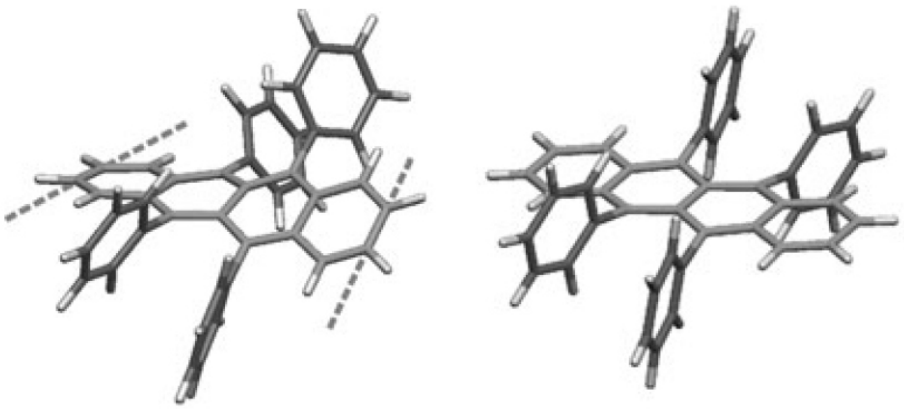

(a) (b)

**Figure 2.5:** Molecular geometries of rubrene in (a) the gas phase and (b) in the solid phase [39]. In the gas phase, the lines defined by the exterior carbon atoms of the outermost aromatic rings form an angle of 42°, resulting in axial chirality of the molecule.

Rubrene crystallizes in an orthorhombic unit cell with a = 14.44 Å, b = 7.18 Å, and c = 26.97 Å [41]. The crystal structure of rubrene is shown in Figure 2.6. Rubrene molecules arrange themselves in a herringbone pattern

in the **ab** crystallographic plane. The interplanar distance $d_{001}$ between consecutive layers of rubrene molecules is 1.34 nm [39].

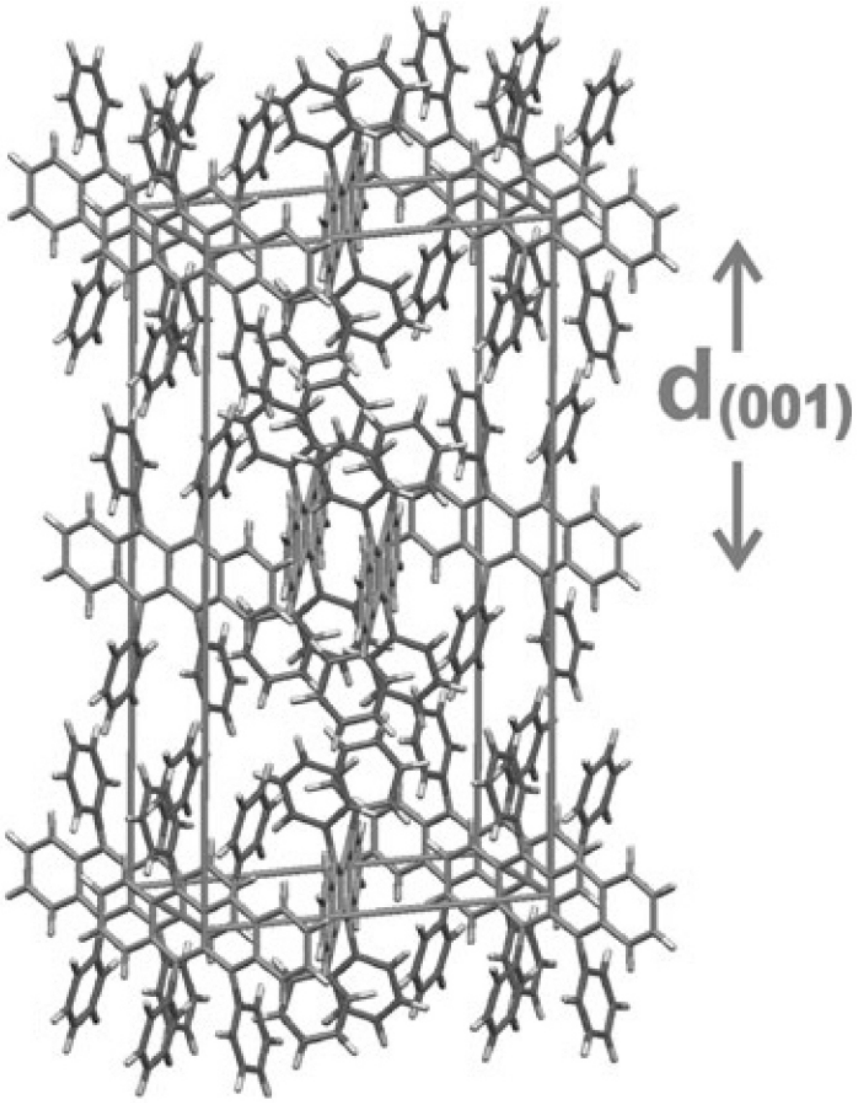


**Figure 2.6:** Orthorhombic crystal structure of rubrene. The molecules arrange themselves in a herringbone pattern in the **ab** crystallographic plane. The distance $d_{001}$ between consecutive planes of rubrene molecules is 1.34 nm. The image was adapted from a figure in Ref. [39].

## 2.4 TPD

$N, N'$-bis(3-methylphenyl)-$N, N'$-diphenylbenzidine (TPD) has been adopted as model system in studies of hole transport in organic materials [42]. It is widely used as an active compound in white light electroluminescent devices [43], voltage-tunable OLEDs [44, 45], and flat panel displays [46].

The chemical formula of TPD is $C_{38}H_{32}N_2$. Based on the optical conductivity measurements the energy gap in TPD is $\approx 3$ eV [47]. The molecular geometry of TPD is three-dimensional. As shown in Figure 2.7, the molecule consists of the central biphenyl moiety and four terminal aryl rings. The biphenyl part of the molecule has a twisted geometry with the torsion angle between the central two aromatic rings of 33.8°. The molecule can also be seen as being composed of two triphenylamine parts. The three phenyl groups assume a propeller-like structure with the torsion angles of 42.0°, 40.6°, and 42.3° with respect to the plane defined by the three N-C bonds.

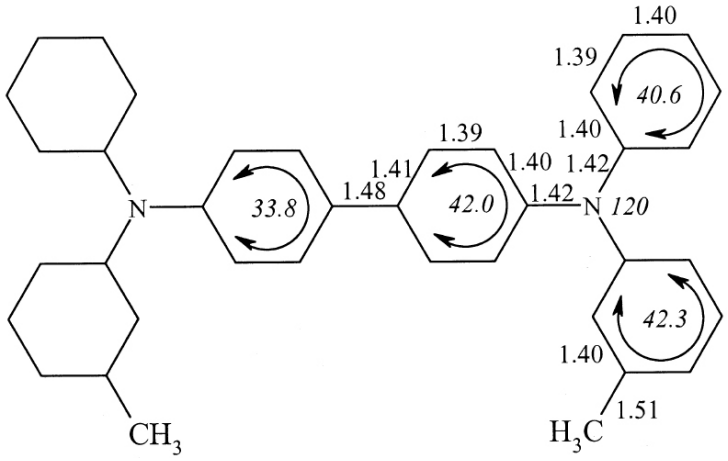


**Figure 2.7:** Structural formula of TPD in the gas phase based on density functional theory calculations [48].

TPD crystallizes in an orthorhombic unit cell with a = 11.07 Å, b = 14.47 Å, and c = 17.82 Å . X-ray diffraction data showed that the torsion angles between the different aromatic rings in the molecule are significantly altered in the solid state [49]. Moreover, two different conformations of the molecule exists in bulk TPD. The second conformation of the molecule is obtained by a formal rotation of the two terminal aryl rings around the C-N bond. The structural complexity of TPD results in favorable conditions for geometry reorganization of the molecule. This fact was confirmed by observation of rotational movement of the four terminal aryl rings of the molecule in the solid state even at temperatures as low as 150 K [49].

# 3 Experimental methods

## 3.1 Organic molecular beam deposition

Organic molecular beam deposition (OMBD) is a common technique used to deposit thin organic films [3]. In OMBD, beams of molecules emerge from temperature-controlled effusion cells and strike the surface of a substrate which can be held at a desired temperature. Slow growth rates ($\sim$1 monolayer/min) allow controlled growth of thin organic films on a molecular level.

OMBD is typically carried out in a vacuum chamber (see Figure 3.1) with a pressure of the residual gas ranging from $10^{-5}$ Pa to $10^{-9}$ Pa. The flux of the molecules that strike the substrate surface is controlled by the temperature of the effusion cell and by a mechanical shutter which can be used to turn the beam "on" or "off". A quartz crystal thickness monitor is used to measure thicknesses of deposited layers.

To preserve the beam nature of the molecular transport, the background pressure in the vacuum chamber must not exceed a certain value. This value can be estimated from the condition that the mean free path $L_b$ of the molecules in the beam, which penetrate the residual gas, has to be larger than the distance from the outlet of the effusion cell to the substrate surface [2]. Using the kinetic theory of an ideal gas, which is applicable at low pressures, the mean free path of the molecules can be expressed as [50–52]

$$L = \frac{1}{\sqrt{2}\pi n d^2}, \tag{3.1}$$

where $n$ and $d$ are the concentration and the diameter of the molecules, respectively. The concentration of the gas molecules is related to pressure $p$ and temperature $T$ via the ideal gas law

$$n = \frac{p}{k_B T}, \tag{3.2}$$

where $k_B$ is the Boltzmann constant ($k_B = 1.38 \times 10^{-23}$ JK$^{-1}$). Assuming that the beam and the residual gas make up a mixture of two gases, the

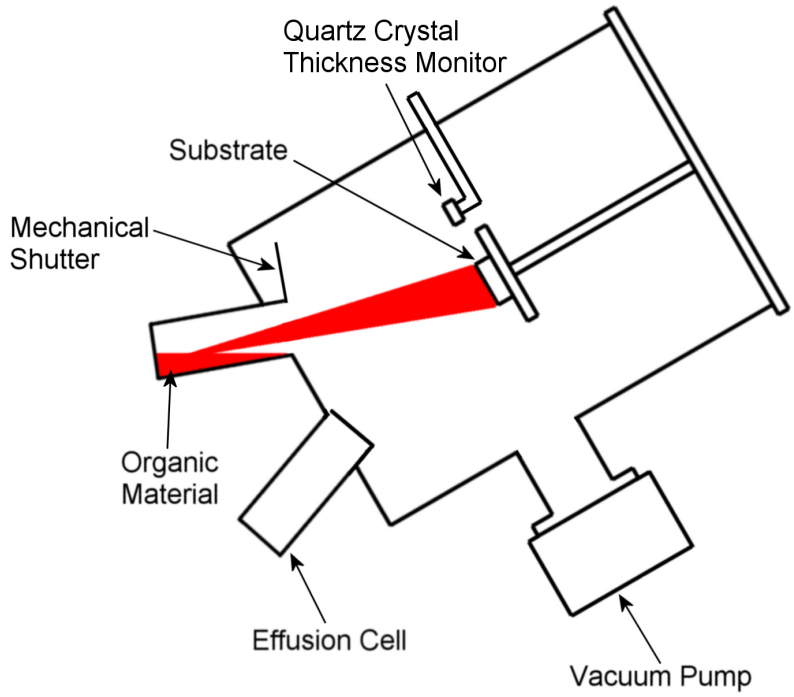


**Figure 3.1:** A schematic cross-section of a vacuum chamber used to deposit thin organic films.

following formula [51] can be used to calculate the admissible concentration of the molecules in the residual gas:

$$L_b^{-1} = \sqrt{2}\pi n_b d_b^2 + \pi n_g d_{bg}^2 \sqrt{1 + v_g^2/v_b^2} \tag{3.3}$$

with

$$d_{bg} = \frac{d_b + d_g}{2},$$

where $n_b$, $d_b$, and $v_b$ are the concentration, diameter, and average velocity of the molecules in the beam, respectively, while $n_g$, $d_g$, and $v_g$ stand for the concentration, diameter, and average velocity of the residual gas molecules in the vacuum chamber. Substituting (3.2) into (3.3) for the concentration of the residual gas molecules and rearranging the obtained expression, the following result for the admissible pressure of the residual gas is obtained:

$$p_g = k_B T \frac{L_b^{-1} - \sqrt{2}\pi n_b d_b^2}{\pi d_{bg}^2 \sqrt{1 + v_g^2/v_b^2}}. \tag{3.4}$$

The average velocities of the molecules can be calculated from the kinetic theory of gases [52]:

$$v = \sqrt{\frac{3k_BT}{m}}, \tag{3.5}$$

with $m$ being the mass of the molecule ($m = Mm_u$, where $M$ is the relative molecular mass and $m_u = 1.66\times10^{-27}$ kg is the atomic mass unit). Assuming the vacuum chamber is filled with air at room temperature, the following values can be used for the residual gas:

$$T = 300 \text{ K},\ d_g = 3.74 \times 10^{-10} \text{ m},\ M_g = 29,$$

where $d_g$ was taken from the viscosity measurements of air at 273 K [50, 51]. These are the typical data for OMDB growth of PTCDA in our studies:

$$\begin{aligned} T_b &= 600 \text{ K},\ d_b \approx 10^{-9} \text{ m},\ M_b = 392, \\ L_b &\approx 0.1 \text{ m},\ n_b \approx 1 \times 10^{14} \text{ m}^{-3}. \end{aligned}$$

The concentration of the molecules in the beam $n_b$ was calculated from the growth rate $R$ using the equation

$$n_b = \frac{R\rho}{M_b m_u v_b}. \tag{3.6}$$

where $\rho$ is the density of PTCDA (1.69 g/cm$^3$ from Ref. [20]). The typical growth rates employed in our experiments (except in studies of dependence of pentacene island density on deposition rate) were $\approx 0.5$ nm/min. Using the above data, the maximum value of the residual gas pressure is $p_g^{max} \approx 1\times10^{-2}$ Pa. This condition is easily fulfilled in most OMBD systems. However, more rigorous conditions must be satisfied if one wishes to assure a low concentration of impurities, which may disrupt the stacking habits of the molecules in the deposited layer.

The condition for growing a sufficiently clean organic layer is satisfied if the impurity incorporation rate is substantially lower than the film growth rate. The time for a monolayer of residual gas molecules of mass m to adsorb onto a substrate surface can be calculated using simple kinetic theory [53]:

$$\tau = \frac{N_S\zeta\sqrt{2\pi m k_B T}}{p}, \tag{3.7}$$

where $N_S$ is the density of surface molecules required to form a complete monolayer, $\zeta$ is the sticking coefficient of the residual gas molecules, and $p$ is the residual gas pressure. Assuming that the residual gas in the vacuum

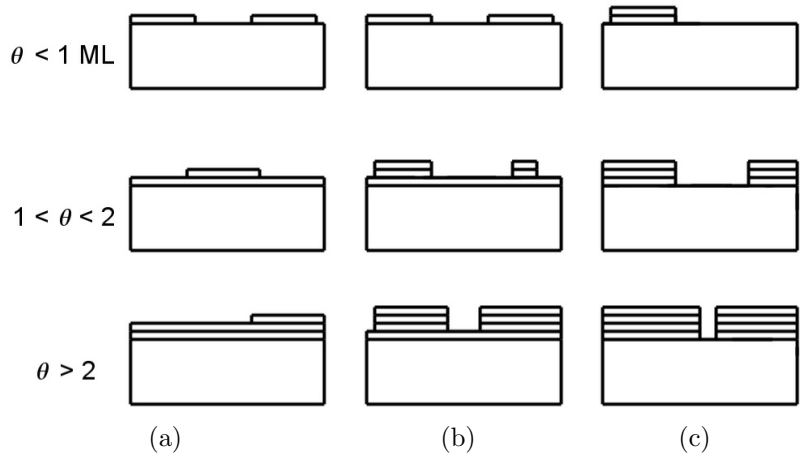


**Figure 3.2:** Schematic representation of three growth scenarios in organic thin film growth: (a) layer-by-layer or Frank-van der Merve mode, (b) layer-plus-island or Stranski-Krastanov mode, and (c) island growth or Volmer-Weber mode. Θ represents the coverage in monolayers.

chamber is nitrogen at room temperature, $\zeta = 1$ and $N_S = 10^{14}$ cm$^{-2}$ [3], the residual gas pressure should be less than $5.8 \times 10^{-7}$ Pa in order to achieve an impurity incorporation rate of less than 1 monolayer/min. This is a more rigorous requirement, however, it should be noted that the sticking coefficient of the residual gas molecules is usually lower than that of the beam molecules [2]. This means that relatively clean organic layers can be grown at rates of $\approx 1$ nm/min ($\approx 1$ monolayer/min) and background pressures of $\approx 10^{-6}$ Pa. Nevertheless, to assure a minimum concentration of impurities, an OMBD system which can achieve the lowest possible background pressure should be used.

The structure of organic thin films grown by OMBD depends on factors such as type of molecule-substrate interaction, growth rate, substrate temperature, density of surface defects, etc. Three growth scenarios are possible, depending on the relative strengths of the molecule-molecule and molecule-substrate interactions [54]. If the molecule-substrate interaction is stronger than the molecule-molecule interaction this results in a layer-by-layer or Frank-van der Merve growth mode. On the other hand, if the molecules are more strongly bound to each other than to the substrate this leads to island or Volmer-Weber growth mode. An intermediate case known as layer-plus-island or Stranski-Krastanov growth mode is also possible. In this case layer growth is energetically unfavorable after the first few monolayers are formed, which results in island growth on top of this intermediate layer. The three different growth modes are illustrated in Figure 3.2.

In all three scenarios the initial stages of growth are characterized by island formation. In the case of layer-by-layer and layer-plus-island growth modes the growth of the first monolayer proceeds via nucleation of two-dimensional (2D) islands. During deposition of the material the islands grow and eventually coalesce to form a complete monolayer. In Volmer-Weber growth mode three-dimensional (3D) islands nucleate from the onset of growth.

The density of islands (whether they are 2D or 3D) depends on the deposition rate and substrate temperature. A model developed primarily for clustering in inorganic systems [54], which is also being adopted for investigation of island nucleation in thin organic films [30, 55], predicts that the density of stable islands $N$ varies as a power law with the deposition rate $R$ and as an activated Arrhenius law with the substrate temperature $T_S$:

$$N \propto R^{\delta} \exp(E_{Nucl}/k_B T_S), \tag{3.8}$$

where $E_{Nucl}$ is the activation energy for homogeneous nucleation and $\delta$ a critical exponent. $E_{Nucl}$ depends on the activation energies of different processes that may occur on the surface, such as surface diffusion ($E_D$), desorption from the substrate surface ($E_A$), and formation of an island of a critical size $i$ with a binding energy $E_i$. $E_i$ is defined as the difference in free energy between $i$ non-interacting molecules adsorbed on a surface and $i$ molecules that form an island. Both $E_{Nucl}$ and the value of the critical exponent $\delta$ depend on the condensation regime [54], critical cluster size and dimensionality of the clusters.

The OMBD system used in our studies consisted of a custom made introduction-chamber and a main chamber equipped with temperature controlled effusion cells and a quartz-crystal thickness monitor. The two chambers were separated by a gate valve and were connected to separate pumping stages that consisted of a rotary vane pump and a turbo-molecular pump. The background pressure in the main chamber during the deposition of the organic material was $\approx 1 \times 10^{-6}$ Pa ($\approx 1 \times 10^{-8}$ mbar). The samples were transfered on a sample holder from the introduction-chamber into the main chamber with a magnetic linear drive. This allowed the main chamber to be constantly under vacuum. The sample holder was attached to a manipulator that allowed movement and rotation of the sample holder around three translational and two rotational axes. This insured precise positioning of the sample in front of the molecular beam. The distance from the sample surface to the outlet of the effusion cell was $\approx 10$ cm. In the case of the polymeric substrates the samples were mounted directly onto the sample holder in the main chamber.

As discussed above the two key factors that influence the structure of organic films grown by OMBD are substrate temperature and deposition rate. In our experiments the substrate temperature was controlled with a sample heating/cooling block that was attached to the sample holder in the main chamber. This enabled precise temperature control ($\pm 0.5^\circ$ C) of the sample surface. The deposition rate was measured with a quartz crystal thickness monitor. The accuracy of the quartz microbalance was $\pm 0.2$ nm, which allowed the deposition rate to be measured with an accuracy better than 10%.

## 3.2 Atomic force microscopy

Atomic force microscopy (AFM) is a technique used for characterization of surfaces on the nanometer scale. The method is based on measurement of forces that act between a sample surface and a sharp tip [56]. The tip is mounted on the end of a cantilever which acts as a force sensor. There are many modes of AFM operation which exploit the static deflection of the cantilever or the change in its dynamic properties due to the tip-sample interaction.

In most AFM instruments the deflection of the cantilever is measured by reflecting a laser beam from the rear side of the cantilever and monitoring the deflection of the beam with a position-sensitive detector. The method is illustrated in Figure 3.3. If the detector is a four-segment photodiode both, the normal bending and the torsion of the cantilever, which is a result of lateral forces that act on a tip, can be measured. Alternative methods of detecting the cantilever deflection include using a cantilever as one mirror in an optical interferometer [57], measuring the change in capacitance between the cantilever and another electrode [58], and using a piezoresistive cantilever [59].

The experimental set-up of the AFM depends on the mode of operation. Typically the sample is mounted onto a piezo scanner (see Figure 3.3) which can translate the sample in the horizontal plane. This allows investigation of different portions of the sample surface.

### 3.2.1 Contact atomic force microscopy

#### Topographic imaging

In contact mode topographic images are recorded by scanning the tip over the sample surface at a constant cantilever deflection. When the tip encounters a surface feature the deflection of the cantilever is used as an input signal

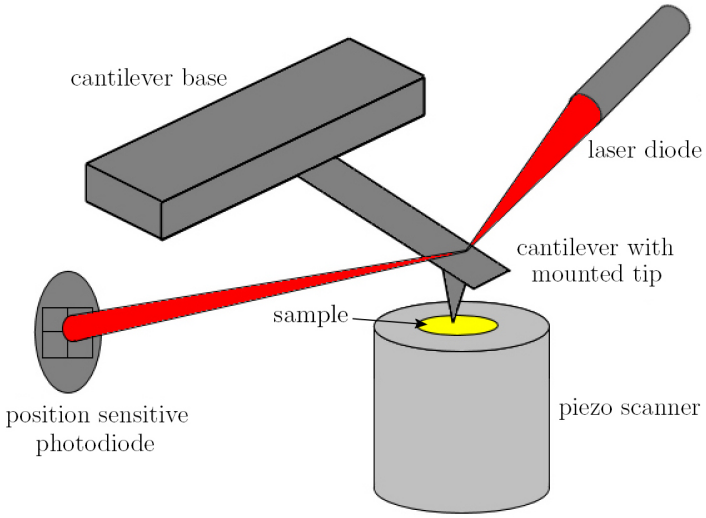


**Figure 3.3:** Schematic diagram of the beam-detection system in AFM. The incident laser beam is reflected from the cantilever onto the position-sensitive photodiode. The four segment photodiode can detect both the normal deflection and the torsion of the cantilever. The sample under investigation is mounted onto a piezo tube. Applying voltage to the piezo tube results in translation of the sample in the horizontal plane which allows different portions of the surface to be examined.

to a feedback loop. The feedback loop is connected to a piezo scanner which translates the sample in the vertical direction until the deflection of the cantilever is brought back to the starting value. The vertical displacement of the sample is used to produce a topographic image.

In contact mode topographic imaging the tip is brought into the repulsive force regime. In this regime the deflection of the tip is determined by an equilibrium of the attractive force between the mesoscopic part of the tip and the sample, the repulsive force between the tip apex and the sample, and the normal force exerted by the cantilever spring (see Figure 3.4).

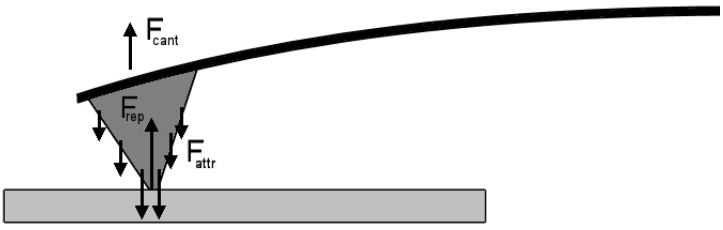


**Figure 3.4:** Forces in contact-AFM. The attractive long-range forces $\mathbf{F}_{attr}$ between the tip and the sample are balanced by the repulsive force $\mathbf{F}_{rep}$ between the tip apex and the sample and the normal force exerted by the cantilever $\mathbf{F}_{cant}$. The bending is chosen to minimize the resulting force.

In contact mode the deflection of the cantilever can be used to measure the net force between the tip and the sample. Since this force is equal to the force exerted by the cantilever it can be calculated by multiplying the cantilever deflection by the cantilever spring constant:

$$F_{cant} = k\Delta z, \tag{3.9}$$

where $k$ and $\Delta z$ are the spring constant and deflection of the cantilever, respectively. Typical cantilever spring constants range from 0.1 N/m to 100 N/m.

Measuring the cantilever deflection versus the vertical displacement of the sample produces a force vs. distance curve that can be used to calibrate the normal cantilever force during topographic imaging. A typical force vs. distance curve for a soft cantilever is shown in Figure 3.5.

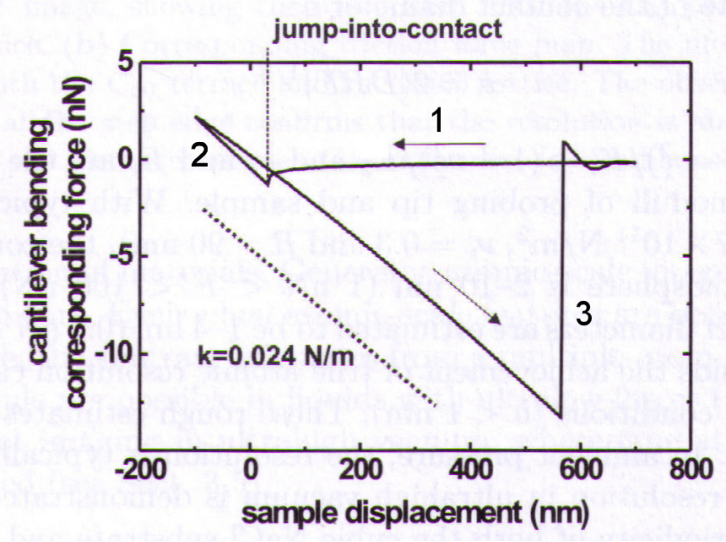


**Figure 3.5:** Cantilever bending vs. vertical sample displacement recorded with a soft cantilever (k=0.024 N/m). The arrows indicate approach and retraction. The image was adapted from Ref. [56].

When the tip is far from the sample the cantilever deflection is constant with respect to the sample displacement (regime 1 in Figure 3.5). When the gradient of the increasing attractive force becomes larger than the spring constant an instability occurs and the tip jumps to contact. After the tip is brought into contact with the sample surface, decreasing the sample displacement results in a linear curve corresponding to Equation 3.9 (regime 2 in Figure 3.5). Adhesion between the tip and the sample surface generates a hysteresis in the force vs. distance curve. A negative normal force exerted

by the cantilever is required to bring the tip out of contact with the sample surface (regime 3 in Figure 3.5). During imaging in ambient conditions the adhesion mainly originates from capillary forces between the tip and a water layer that forms on the sample surface.

During acquisition of images in contact mode the operator will try to minimize the forces on the tip apex by bending the cantilever. This reduces the potential damage to the sample caused by the tip. The method is referred to as applying a negative load.

### Lateral force microscopy

Moving the tip across the sample surface in the direction perpendicular to the long cantilever axis results in a lateral component of the force between the tip apex and the sample. This lateral force causes torsional bending of the cantilever, which can be detected using a four segment photodiode in a beam-deflection-type AFM. The signal produces a frictional map of the sample surface. For a quantitative analysis of the data the torsional bending of the cantilever has to be calibrated [56].

The signals due to the normal and torsional bending of the cantilever may interfere resulting in image artifacts on both topographic and frictional maps. This effect can be accounted for by comparing the forward and reverse topographic scans. If the effect of the torsional bending is negligible the topographic images should be identical for both scan directions, while the lateral force maps are inverted.

### Transverse shear microscopy

Transverse shear microscopy (TSM) is a novel contact AFM technique that was recently utilized to map the grain shape and orientation in polycrystalline organic semiconductor films [60]. As opposed to conventional lateral force microscopy (LFM) where the scanning direction is perpendicular to the long cantilever axis, in TSM, the scan vector and the long cantilever axis are parallel [60–62]. The torsional bending or twisting of the cantilever in TSM is a result of the net shear forces that act between the tip apex and the sample surface. With TSM it is possible to observe the grain shape and orientation in oligoacene polycrystalline thin films. The method relies on the in-plane anisotropy of the elastic properties of these materials. The operational principle of TSM is illustrated in Figure 3.6.

For a quantitative analysis of the TSM data, the crystalline structure of the material must be known. Since the crystalline structure of the thin film may differ from the bulk crystal structure, TSM data has to be complemented

by X-ray diffraction measurements on both the single crystal and the thin film.

On pentacene thin films the TSM signal is nearly a factor of 10 smaller than the conventional LFM signal [60]. This means that topographic surface features that result in twisting of the cantilever will likely obscure the contribution to the TSM signal that arises from the elastic anisotropy of the material. Due to this fact only relatively smooth films will produce TSM contrast in practice.

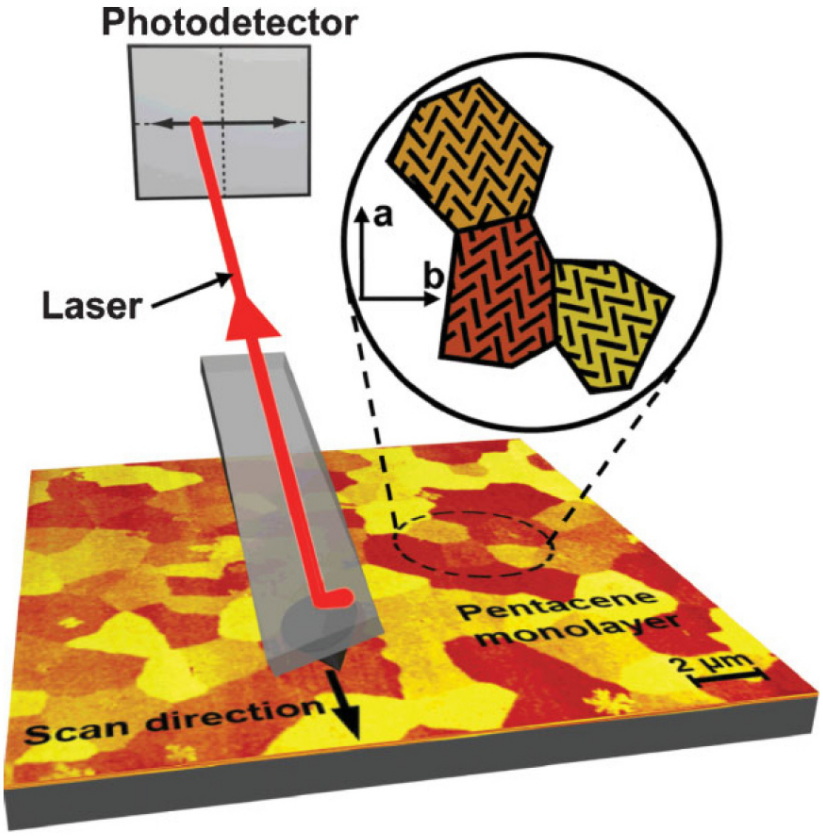


**Figure 3.6:** Scheme illustrating the working principle of TSM. The torsion of the cantilever is detected by reflecting a laser beam from the cantilever onto a position-sensitive detector. In the above image the sample under investigation is a monolayer thick pentacene film. The film consists of coalesced crystalline grains (islands) with different orientations. When the scan vector is parallel to the long cantilever axis, the cantilever twist depends on the crystallographic orientation of the grain under the tip. The magnified view depicts the herringbone packing motif of the pentacene molecules in the **ab** crystallographic plane and the relative grain orientation. The image was adapted from a figure in Ref. [60].

### 3.2.2 Dynamic atomic force microscopy modes

When imaging soft samples such as thin organic layers or biological samples in contact AFM the lateral forces exerted by the tip apex may damage the sample surface. This can be avoided by using dynamic atomic force microscopy which provides means for measuring the surface topography with little or no contact between the tip and the sample surface. In dynamic AFM the cantilever is excited by a piezoelectric actuator to oscillate near its resonant frequency with an amplitude of a few to a few tens of nanometers. The typical eigenfrequencies of the cantilevers used in dynamic AFM imaging range from 100 to 400 kHz. Topographic images are acquired by scanning the tip over the sample surface. When the tip encounters a surface feature the changes in the resonant frequency or the vibrational amplitude are used as an input to a feedback loop which controls the tip-sample distance. As in contact AFM the translation of the sample in the vertical direction is used to produce a topography map of the sample surface.

The two main dynamic AFM modes are non-contact AFM (NC-AFM) and intermittent-contact AFM (IC-AFM) also referred to as tapping mode. In non-contact mode the tip-sample distance is on the order of a few to a few tens of nanometers. In ambient conditions the water layer that forms on top of the sample surface may prevent accurate measurements of the topography in non-contact mode. Operating the AFM in a high vacuum overcomes this problem. Furthermore, in a vacuum environment high quality factors of cantilevers also allow precise determination of the shifts in the oscillating frequency. At present non-contact AFM is the only operation mode capable of producing true atomic resolution images with quality comparable to that of scanning tunneling microscopy (STM) [56, 63].

IC-AFM is similar to NC-AFM, except that the oscillating cantilever is brought into intermittent contact during each cycle (the tip "taps" the sample surface). The amplitude of oscillation reduces with the tip-sample spacing. The changes in the amplitude of oscillation are used to record the surface topography of the sample. Since the tip penetrates the water layer on the sample surface IC-AFM can be used in ambient conditions. Large oscillation amplitudes and stiff cantilevers are necessary in order to overcome the adhesion resulting from capillary forces between the tip and the sample surface.

# 4 Behavior of the (0001) surface of sapphire upon high-temperature annealing

Evolution of the (0001) $\alpha$-$Al_2O_3$ surface morphology upon annealing was studied using atomic force microscopy. The annealing protocol included temperatures of 1200 and 1500°C and different time. Vicinal $Al_2O_3$ (0001) surfaces annealed at 1200°C exhibit initial localized step coalescence that evolves into terrace-and-step with island morphology that persists for several hours. Annealing at 1500°C results in initial step coalescence on a global scale, and yields a terrace-and-step morphology with an indication of step bunching after longer annealing times.

## 4.1 Introduction

An increased interest in atomically smooth surfaces of $\alpha$-$Al_2O_3$ single crystals was observed a decade ago, when such a surface was considered as a viable substrate for GaN growth [64]. Today, renewed interest in $\alpha$-$Al_2O_3$ single crystals stems from the ability to obtain nanoscale structures on vicinal surfaces that may serve as templates for organic semiconductor thin film growth [65, 66]. The unit cell of sapphire, $\alpha$-$Al_2O_3$, is hexagonal with a = 4.76 Å, and c = 13.00 Å [67]. The crystal structure along the (0001) direction can be viewed as an alternative stacking of one oxygen plane, and two aluminum planes. The unit cell comprises six such oxygen planes sandwiched between planes of aluminum atoms. In this view, the separation of two neighboring planes of oxygen atoms equals c/6 which amounts to 0.21 nm. From this and several previous studies we can see that this distance represents a unit measure that determines morphological changes of (0001) and $(10\bar{1}0)$ surfaces and their vicinal variants.

Sapphire surface morphology is known to be strongly dependent on the

annealing protocol and on the surface orientation [68, 69]. Annealing of the $(10\bar{1}0)$ surface results in a hill-and-valley structure [68], while annealing of the (0001) surface results in a terrace-and-step structure [70]. Yoshimoto *et al.* [64] investigated the morphology of the sapphire (0001) surface after annealing at 1000 and 1400°C for 1 h. They report on an atomically flat surface characterized by uniform steps of 0.2 nm heights, if the sample was annealed at 1000°C for 1 h. Annealing at 1400°C instead, produced a morphology characterized by steps with heights that were integer multiples of 0.2 nm. Terrace-and-step morphology is attained via faceting, and initial stages of this process are reported in Ref. [70]. AFM investigation of the sapphire (0001) surface after annealing for 10 min at 1400°C revealed that faceting begins with the formation of domains of steps that are a multiple of c/6 in height, separated by terrace-and-step surfaces with c/6-high steps. Steps were observed to bunch in pairs. Step pairing and differences in surface areas of terraces separated by steps that are a multiple of c/6 high were presented as evidence for different surface terminations on adjacent terraces. Temperature dependence of morphology of vicinal (0001) sapphire surfaces was explored by Pham Van *et al.* [71]. They observed an evolution of the surface morphology from a surface characterized by c/6-high steps at 1000°C annealing temperature to a surface characterized by steps that are a multiple of c/6 in height. In addition to the zipper-like mechanism of step coalescence, they proposed a mechanism of parting one multiple step into a monostep and another multiple step; a phenomenon that was observed after annealing at higher temperatures. Increasingly high annealing temperature therefore drives the vicinal (0001) surface from a terrace-and-step morphology with c/6-high steps to a coarse morphology arrived at through step coalescence.

In this study we will show that the surface may undergo a variety of transformations that are temperature and time dependent prior to arriving at an equilibrium morphology that is characteristic for a given annealing temperature.

## 4.2 Experimental

$Al_2O_3$ samples used in this study were obtained from polished nominally flat wafers (Cradley Crystals Corp.) and from polished wafers with a nominal miscut of 0.2° towards $[11\bar{2}0]$. Annealing of the wafers was performed in air at temperatures of 1200 and 1500°C. The temperature of the furnace was controlled with an accuracy of ±1°C. In order to minimize contamination of the surface of the samples, recrystallized alumina furnace tube and crucible were used. Each sample was annealed at a given temperature in three stages.

After each stage the sample temperature was allowed to drop rapidly (> 50°C/min), and the sample was transferred to an atomic force microscope (AFM) for surface morphology examination. Upon completion of the AFM analysis, the sample was subjected to the next stage of the annealing protocol. The duration of the annealing stages was 1, 3, and 12 h at one temperature, resulting in a total annealing time of 16 h.

## 4.3 Results

Surface morphology of an as-received, nominally flat sapphire sample is shown in Figure 4.1, where we show a $3 \times 3$ $\mu$m$^2$ AFM scan of the sample surface. The surface exhibits a terrace-and-step morphology with a step height of $(0.21 \pm 0.02)$ nm and a step width of $(133 \pm 19)$ nm. The direction of the steps is constant over the surface of the sample, however terrace edges are poorly defined. In addition, 1 nm-high spikes are also present on the surface, and may be a consequence of wafer polishing. As-received samples, with a nominal miscut of 0.2°, exhibit similar surface morphology, but with narrower terraces. In this case, the terrace width was $(57 \pm 6)$ nm, resulting in a miscut angle of $0.21° \pm 0.04°$.

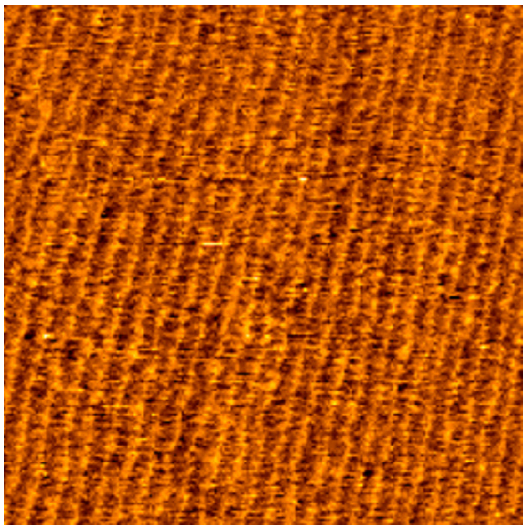

**Figure 4.1:** A $3 \times 3$ $\mu$m$^2$ AFM image of an as-received, nominally flat sapphire sample.

After annealing the samples at 1200°C for 1 h the surface morphology changed substantially. This is exemplified in Figure 4.2, where we show a representative $3 \times 3$ $\mu$m$^2$ AFM height scan of a nominally flat sample annealed at 1200°C for 1 h. The surface is predominately covered with

terraces, separated by c/6-high steps. Terrace edges are now better defined as compared to terrace edges on the as-received sample (Figure 4.1). C/6-high islands cover a small fraction of the surface. An example of such island is enclosed in a circle in Figure 4.2. The terrace, on which the island is located, is wider relative to terraces, which are not covered with islands. On the other hand, the two terraces adjacent to the terrace containing the island are narrowed near the island. Typical for the surfaces of the samples annealed at 1200°C for 1 h are also features of the type, indicated by two arrows in Figure 4.2. Arrow 1 indicates coalescence of four c/6-high steps into a single step of approximately 0.8 nm in height. Arrow 2 indicates a c/6-high island left from the coalescence process. On a nominally flat sample annealed at 1200°C for 1 h, coalescence typically involves two to four c/6-high steps. The majority of the resulting steps are triple steps.

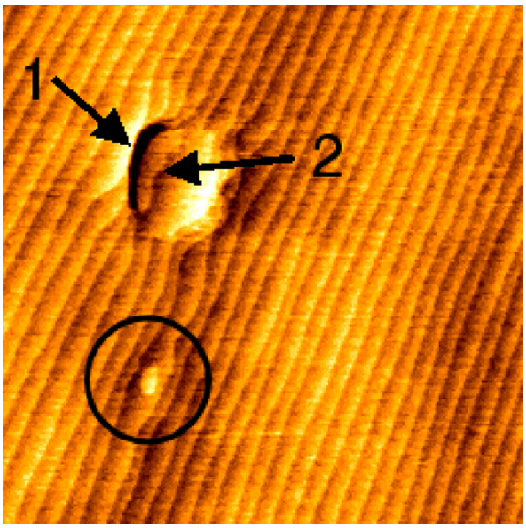


**Figure 4.2:** A $3 \times 3$ $\mu$m$^2$ AFM image of a nominally flat sample annealed at 1200°C for 1 h.

Coalescence of steps is more pronounced on a miscut sample annealed under the same conditions. This is exemplified in Figure 4.3. In Figure 4.3(a) we see that coalescence of steps occurs on a larger portion of the surface as compared to coalescence on a nominally flat sample. Up to seven c/6-high steps may coalesce to form a step with a height that is a multiple of c/6. Some of the islands left from coalescence measure c/6 in height, while others measure 0.4 nm in height. The majority of multiple steps are triple steps. Arrows in Figure 4.3(b) indicate coalescence of three c/6-high steps, and a c/6-high island left from the coalescence process.

Annealing the samples for additional 3 h at 1200°C yields further modification of the surface morphology. A $3 \times 3$ $\mu$m$^2$ AFM image and a $1 \times 1$ $\mu$m$^2$

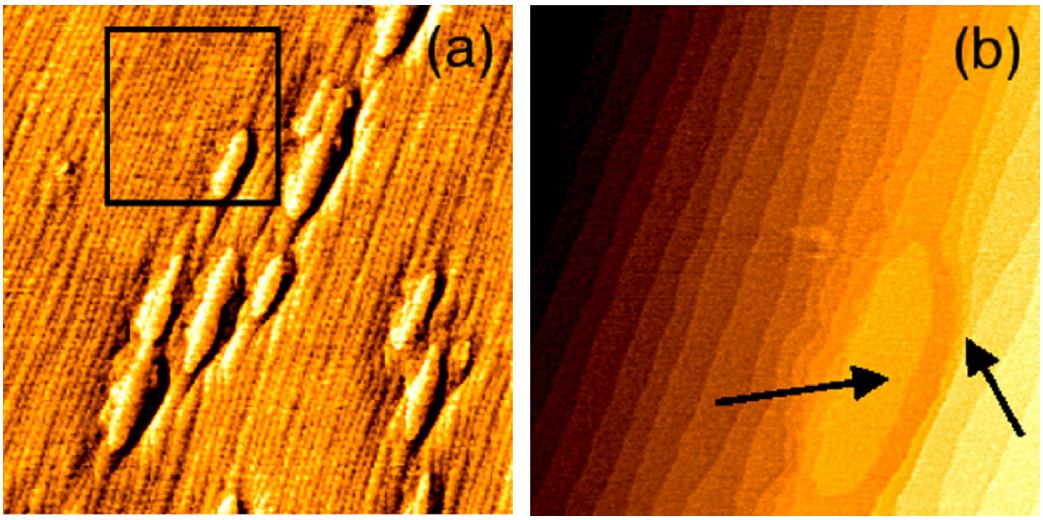


**Figure 4.3:** (a) A $3 \times 3$ $\mu$m$^2$ AFM image of a sample with a nominal miscut of 0.2° annealed at 1200°C for 1 h. (b) A $1 \times 1$ $\mu$m$^2$ magnification of the surface enclosed in the rectangle in (a).

close-up of the same image of a nominally flat sample annealed at 1200°C for 4 h are shown in Figure 4.4(a) and (b), respectively. Figure 4.4(c) shows a height profile obtained along the line indicated in Figure 4.4(b). The surface is characterized by terraces, which are separated by c/6-high and 2×c/6-high steps. Terraces are decorated with c/6-high islands. The majority of these islands spread over a terrace edge onto a neighboring terrace. By using pixel counting, we estimated that the island coverage of the surface shown in Figure 4.4(a) is approximately 65%. The surface densities of c/6-high and 2×c/6-high steps are approximately the same. The step height on the surface is $(0.33 \pm 0.12)$ nm.

Miscut samples exhibit similar morphology, when annealed for additional 3 h at 1200°C (Figure 4.5(a)), however, in this case the fraction of c/6-high steps is negligible compared to the fraction of 2×c/6-high steps. There is also a small fraction of 3×c/6-high steps on the surface. The average step height on the sample in Figure 4.5(a) is $(0.45 \pm 0.06)$ nm. Terraces are decorated with 2×c/6-high islands. The island coverage of the surface in Figure 4.5(a) is approximately 35%. Further annealing, a total of 16 h, of the miscut sample, results only in a slight modification of the surface (Figure 4.5(b)). The fraction of c/6-high steps increases, and a majority of the steps are 2×c/6-high steps. The average step height decreases to $(0.35 \pm 0.07)$ nm on the account of c/6-high steps. Islands, which decorate the terraces, are elongated. The island coverage of the surface in Figure 4.5(b) reduces to 16%.

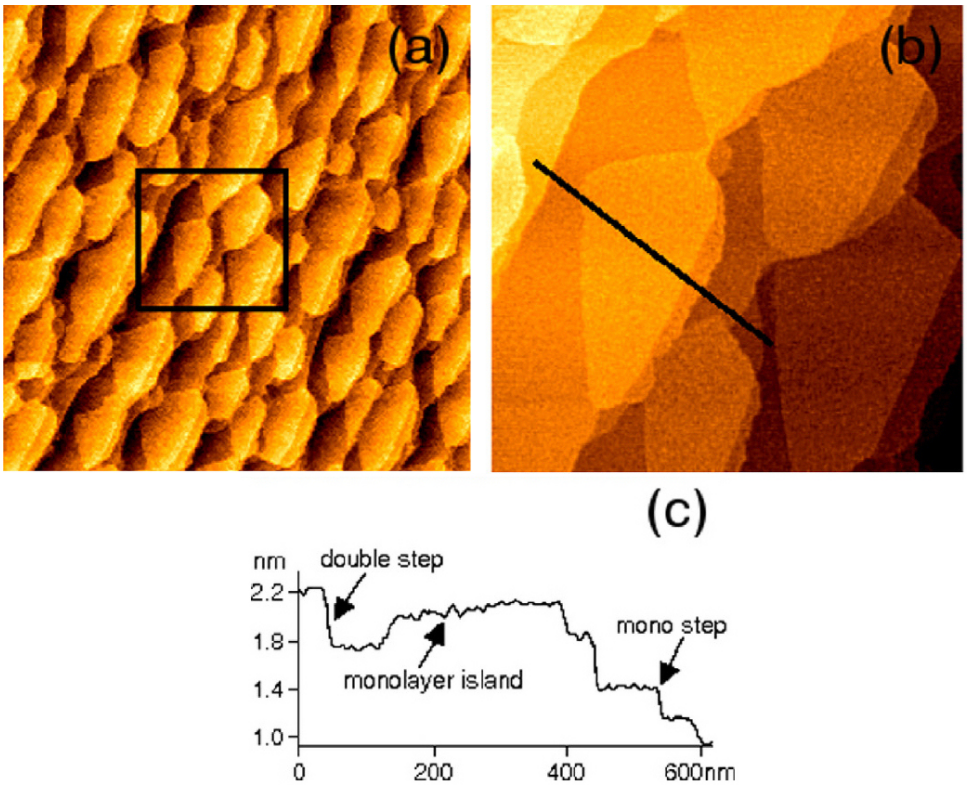


**Figure 4.4:** (a) A $3 \times 3$ $\mu$m$^2$ AFM image of a nominally flat sample annealed at 1200°C for 4 h. (b) A $1 \times 1$ $\mu$m$^2$ magnification of the surface enclosed in the rectangle in (a). (c) Height profile taken along the line indicated in (b).

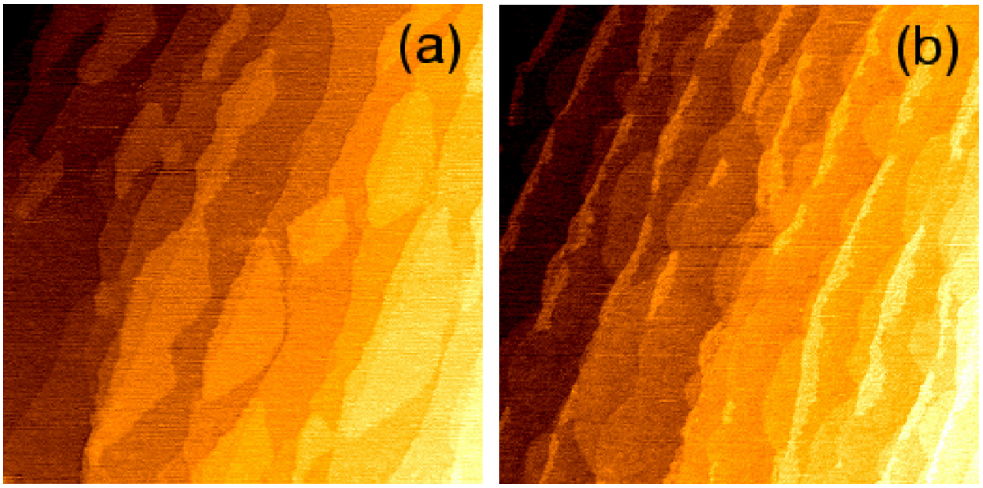


**Figure 4.5:** $1 \times 1$ $\mu$m$^2$ AFM images of a sample with a nominal miscut of 0.2° annealed at 1200°C for (a) 4 h and (b) 16 h.

Further surface evolution is observed upon annealing at 1500°C. Figures 4.6(a)-(c) show the surface morphology of a sample with a nominal miscut of 0.2° annealed at 1500°C for 1, 4, and 16 h, respectively. In contrast to annealing a sample at 1200°C for 1 h where step coalescence occurs only locally, annealing the sample at 1500°C for 1 h results in coalescence of steps on a global scale (Figure 4.6(a)). The average step height on the surface is $(0.85 \pm 0.33)$ nm. As with the samples annealed at 1200°C, coalescence of steps results in faceting. The circle in Figure 4.6(a), where the steps change direction to a low-index crystallographic direction indicates this. Annealing of the sample for additional 3 h increases the step height to $(1.25 \pm 0.40)$ nm (Figure 4.6(b)). Terraces are nearly parallel, and are decorated with 2×c/6-high, elongated islands. In Figure 4.6(b) we also observe bright spots. These are islands of few nm in height and few tens of nm in diameter, and are sometimes observed on alumina surface after annealing. Their origin is unknown, however they do not interfere with the morphological evolution of the (0001) surface during annealing, since we have observed similar features on morphologically substantially different surfaces. In Figure 4.6(b) approximately 42% of the surface is covered with islands. Further annealing of the miscut sample reduces the step height to $(0.58 \pm 0.28)$ nm (Figure 4.6(c)). Coalescence of steps is present on a relatively small portion of the surface. The circle in Figure 4.6(c) indicates coalescence of a 2×c/6-high and a c/6-high step into a 3×c/6-high step.

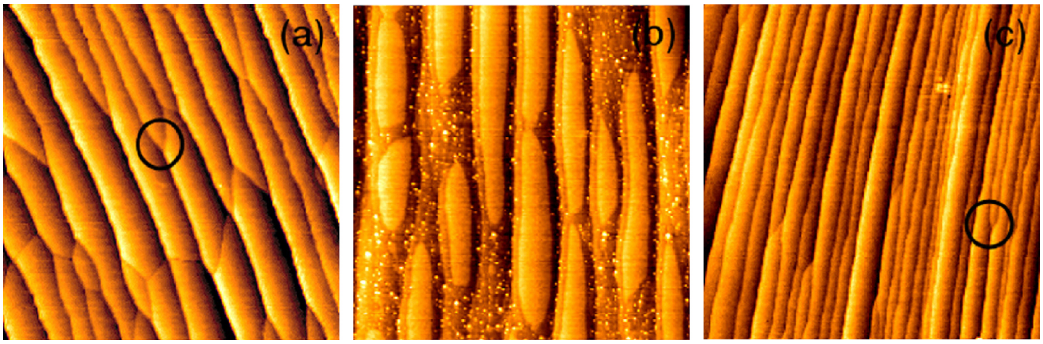


**Figure 4.6:** $3 \times 3$ $\mu$m$^2$ AFM images of a sample with a nominal miscut of 0.2° annealed at 1500°C for (a) 1 h, (b) 4 h, and (c) 16 h.

## 4.4 Discussion

Our studies represent an investigation of the morphological changes of the (0001) alumina surface in a stage that might represent a different route in

the morphology evolution investigated in Refs. [68] and [70], and is likely to be prior to the stage investigated in Ref. [71]. As we see from Figures 4.2 and 4.3, annealing nominally flat, as wells as miscut surfaces at 1200°C for 1 h has already produced a typical terrace-and-step structure with c/6-high steps. However, clearly defined areas where individual steps started to coalesce can be observed. The circle in Figure 4.2 encloses an island of 0.21 nm in height on a terrace. A concave shape of the edge of the terrace to the left of the island suggests that the island has nucleated by mass transport in the direction perpendicular to the terrace edge. We have observed several instances of coalescence of two steps that resulted in a double step, a wider terrace and a c/6-high island on it (not shown). This process can involve several steps as indicated by Arrow 1. The resulting step height after coalescence is $i \times c/6$, where $i$ is the number of steps involved in coalescence. The process of step coalescence under the same annealing conditions is faster on a miscut sample, where we see a larger portion of the surface morphologically changed as a consequence of step coalescence (Figure 4.3). Consequently, larger atomically flat areas are present on the surface. Characteristic for this stage is, therefore coalescence of c/6-high steps into steps that are a multiple of c/6 in height, and growth of flat c/6-high islands on top of the growing terraces. Note that this is a stage that was not observed after annealing at higher temperatures. The onset of such localized morphological changes implies that the atoms part from their positions at the steps and form islands on the terrace. The diffusion on the terrace is therefore a preferred matter transport mechanism in this temperature range. Coupled to this process is a coalescence of c/6-high steps that was already reported by Pham Van *et al.* [71], although we observe localized coalescence of more than two steps.

Further annealing of the samples at 1200°C results in surfaces characterized by steps that measure c/6 and 2×c/6 in height, which agrees with the report in Ref. [71]. However, as we see in Figures 4.4 and 4.5 the terraces are decorated with islands that were not observed before. The transformation of the surface after 4 h of annealing is therefore from localized step coalescence and island formation, to a step-and-terrace with islands. In order to arrive to this morphology the higher steps observed after 1 h of annealing must have decomposed into c/6-high steps. Such decomposition, albeit into monosteps and multiple steps was indeed observed in Ref. [71], however at higher annealing temperatures but shorter annealing times (1 h). This indicates that an equilibrium surface morphology is attained only after several hours. Indeed, in Figure 4.5(b) we see that traces of islands on terraces of a miscut sample are still present after 16 h of annealing. Most of the islands in Figure 4.5(a) spread over terrace edges onto neighboring terraces. The islands that remained after annealing for 16 h, are mostly localized to the

terrace edges. In addition, we observe a decrease in the average step height by 0.1 nm resulting in an increased fraction of c/6-high steps. This may be a consequence of incorporation of atoms, from the islands into terraces, lowering thereby the step height.

Annealing the samples at a higher temperature promotes the diffusion of surface atoms. While the samples annealed at 1200°C for 1 h exhibit only local coalescence of steps, annealing the samples at 1500°C for 1 h results in coalescence of steps on a global scale (Figure 4.6(a)). The process is similar as reported in Ref. [71] for annealing at 1200°C. Two lower steps coalesce by a "zipper-like" scheme to form one higher step. As was the case with lower annealing temperature we have experienced additional morphological evolution at 1500°C, not reported before, and qualitatively similar to the evolution observed on flat and miscut samples at 1200°C. In Figure 4.6(b) we observe 2×c/6 islands that decorate terraces. Observing Figure 4.6(c) might provide us with a possible mechanism that leads to the morphology obtained after 16 h annealing at 1500°C. We see that the average step height is reduced to half of that observed in Figure 4.6(b) and that the islands are absent. In addition, the average terrace width is smaller. Such morphology might arise as a consequence of mass transport from the islands to the adjacent terraces, reducing thereby the step height and the terrace width.

## 4.5 Conclusions

Evolution of the (0001) sapphire surface annealed in air at 1200 and 1500°C was studied by AFM in non-contact mode. It was observed that annealing the surface initially covered with 0.21 nm high steps at 1200°C for 1 h results in local coalescence of the steps. Before the coalescence modifies the surface on a global scale we observe a stage where 0.21 nm high islands reside on terraces adjacent to the coalesced steps. This stage is a dynamic one. The step coalescence and island decomposition is continued at the same temperature for several hours, prior to arriving to the surface characterized by a majority of double steps. On a surface annealed at 1500°C for 1 h coalescence of steps occurs on a global scale. Surfaces annealed at 1500°C for 4 h exhibit higher steps as compared to surfaces annealed at 1200°C for 4 h. This is probably a result of the fact that higher temperatures enhance surface diffusion. Further annealing at 1500°C results in transformation of multiple steps, and thus decreases the average step height.

## 4.6 Acknowledgments

This work was financed in part by the Ministry of higher education, science and technology under the research program P1-0040, and by the Center of excellence "Nanosciences and Nanotechnology". Helpful discussions with F. Schreiber, and D. Mihailović are acknowledged.

# 5 Fabrication of rubrene nanowires on vicinal (0001) sapphire surfaces

Morphology of high-vacuum deposited rubrene thin films on annealed (0001) vicinal sapphire surfaces was studied by atomic force microscopy in non-contact mode. Atomic force microscopy images of rubrene thin films indicate that a regular array of steps on the sapphire surface acts as a template for the growth of arrays of rubrene nanosize wires. To further demonstrate that morphological features of a substrate are crucial in determining the morphology of rubrene layers we have grown rubrene on sapphire surfaces that were characterized by a terrace-and-step morphology with islands. We have found preferential nucleation of rubrene molecules at the intersection between a terrace and a step, as well as around the islands located on terraces.

---

Reproducible fabrication of nanoscale organic structures is of crucial importance for successful operation of advanced electronic and optoelectronic devices. Typical approach to fabricate such devices includes deposition of active material onto a suitable substrate. The deposited layer is subsequently modified using lithographic methods. An alternative route may include deposition of an active layer onto a modified-patterned substrate. Patterning may be achieved through the use of a self-assembled layer [72] or by preparation of substrates with atomically well-defined surfaces [5]. As opposed to topdown techniques, which make use of expensive, high precision tools such as electron-beam writing, and advanced lithographic techniques, the latter approach combines cost-effectiveness with the ease of fabrication.

Vicinal crystal planes represent viable candidates for fabrication of nanostructures. The ability of these surfaces to act as templates for the growth of

low-dimensional structures in metallic systems has been thoroughly studied by Kuhnke and Kern [73]. Vicinal semiconductor surfaces have also been used as templates for the growth of 1D structures. Stacked GaAs quantum wires were grown on vicinal GaAs surfaces with giant steps, which were deliberately introduced by step bunching [74]. In organic/inorganic systems, vicinal sapphire surfaces have been successfully used to grow carbon nanotubes along step edges [75]. Controlled growth of organic semiconductors is less explored than controlled growth of their inorganic counterparts. The basic building blocks of organic semiconductors molecules, interact with a substrate mostly via relatively weak dispersion forces. Consequently, controlling the morphology of an organic layer using a pristine atomically clean substrate surface is not an easy task. The morphology of the organic layer is likely to depend on chemical and geometrical properties of the selected molecules.

We focused on the growth of rubrene (5,6,11,12-tetraphenylnaphthacene) thin films on vicinal sapphire surfaces, since both materials exhibit exceptional physical properties and, as we show in this letter, couple favorably in the formation of ordered nanoscale arrays of organic semiconductor wires. The use of rubrene was motivated due to the demonstrated high hole-mobility in single-crystal field-effect transistors [34, 35]. On the other hand, sapphire is a material, which is widely used in different applications: as a substrate for thin film growth [30, 38, 76], as a gate insulator in organic field effect transistors (FETs) [77] and in laser optics [78, 79].

The most suitable sapphire single crystal surface to be used in the patterned film growth is the vicinal (0001) surface. Preparation of a substrate surface prior to the organic semiconductor growth includes high-temperature annealing in order to improve the crystal structure of the surface, and remove the structural defects that were introduced during crystal cutting and polishing. Transformation of the (0001) sapphire surface upon high-temperature annealing is well documented [6, 64, 70, 71]. Typically the starting surface is already characterized by a step-and-terrace morphology. The step height is an increasing function of annealing temperature and time [6, 71], and is observed in multiples of c/6, where c is the size of the sapphire unit cell along the [0001] direction (1.3 nm). Upon high-temperature annealing for an extended period of time, step coalescence yields steps that measure up to 2 nm in height [71]. On the other hand, if the initial surface is rough, annealing leads to formation of 0.21 nm high steps, which then coalesce into multiple steps [70]. We have used sapphire (0001) substrates (Roditi) with a nominal miscut of 0.55° towards $[11\bar{2}0]$. The wafers were prepared by annealing in air at 1500°C for 120 h. After annealing, we have examined the samples using an atomic force microscope (AFM). A $4 \times 4$ $\mu$m$^2$ area of the

surface of a sapphire substrate after annealing is shown in Figure 5.1. We see that the surface is characterized by terraces and steps, as expected for vicinal (0001) surfaces [70, 71]. The resulting step height was $(2.8 \pm 0.5)$ nm, and the average terrace width was $(350 \pm 40)$ nm. The calculated miscut angle from these values was $(0.46 \pm 0.13)^\circ$ towards the $[11\bar{2}0]$ direction.

**Figure 5.1:** A $4 \times 4$ $\mu$m$^2$ AFM image of a sapphire substrate annealed at 1500°C for 120 h. The surface is characterized by terraces separated by steps which on average measure 2.8 nm in height.

As we show below, by exploiting the evolution of the sapphire surface, we can produce suitable substrate morphology that affects the morphology of the overgrown organic layer. Growth of organic layers was performed in a high vacuum chamber with a base pressure of $5 \times 10^{-9}$ Torr. To desorb water from the surface, the substrates were heated for 4 h at 200° C. Prior to thin film deposition, the substrates were cooled down to room temperature. Rubrene (Aldrich) layers of nominal thicknesses of 10 nm were thermally evaporated onto the substrates at a rate of 1 nm/min. The thickness of the layers was determined in situ by a quartz microbalance. Upon completion of growth, the morphology of the overgrown layers was examined ex situ by AFM. In order to reduce potential film damage due to the interaction of the microscope tip and the rubrene molecules, we have operated the AFM in non-contact mode.

A typical AFM image of a rubrene-covered sapphire surface is shown in Figure 5.2. Figure 5.2(a) represents the scanned area of $4 \times 4$ $\mu$m$^2$, where we see that the surface is characterized by a regular array of rubrene wires and a few isolated rubrene islands. The wires follow the direction of steps,

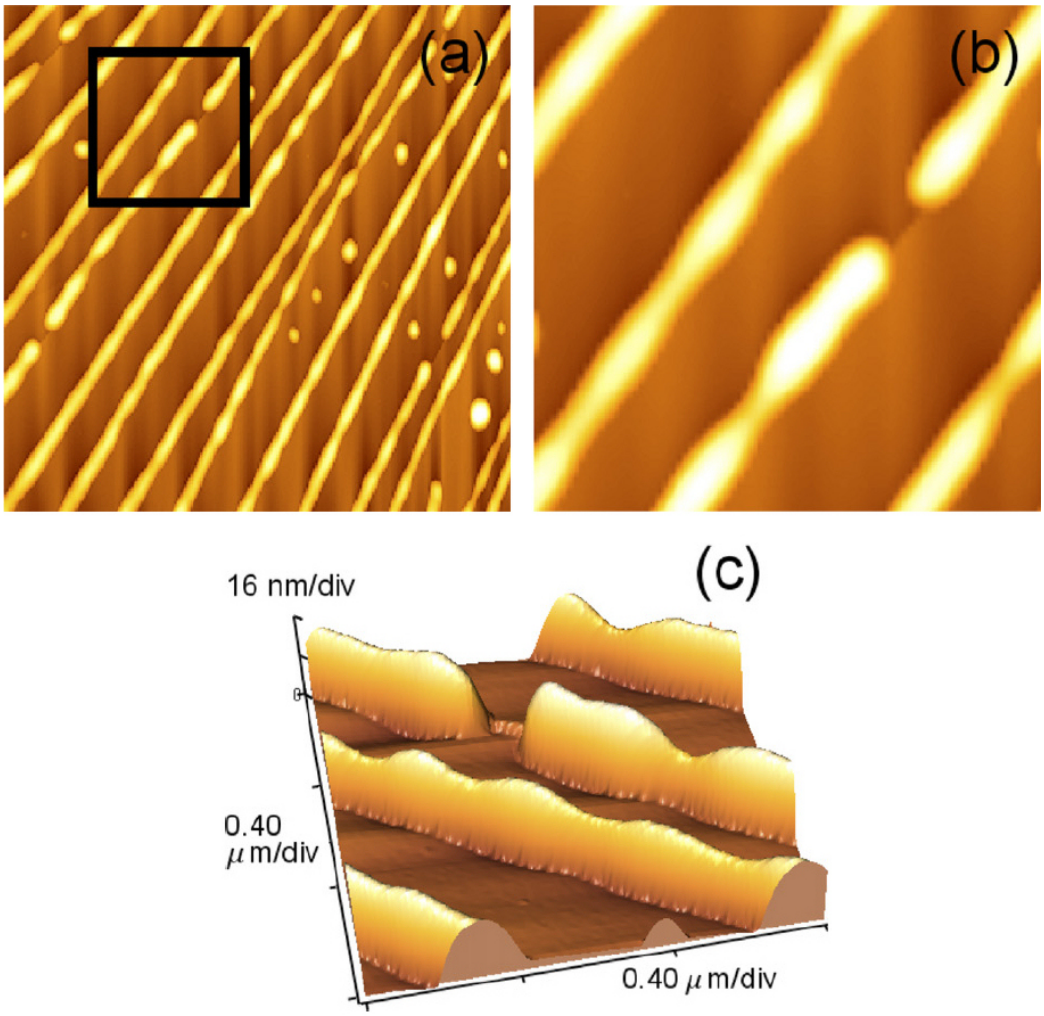


**Figure 5.2:** (a) A $4 \times 4$ $\mu$m$^2$ AFM image of a rubrene film evaporated onto an annealed vicinal (0001) sapphire surface. Rubrene was thermally evaporated onto the substrate at room temperature. The nominal thickness of rubrene as determined by in situ quartz microbalance is 10 nm. Rubrene is observed as wires of lighter tones located at the sapphire steps. (b) A $1.2 \times 1.2$ $\mu$m$^2$ magnification of the boxed area indicated in (a). One of the wires is disconnected, and the sapphire step can be observed. (c) A three dimensional rendition of the image from (b). The size of the wires can be estimated from the vertical and lateral scales.

and are all located at the edges of the terraces. The additional contrast in the form of darker vertical tones is a result of a nonlinear response of the AFM. Figure 5.2(b) is a magnification of the boxed region in Figure 5.2(a) ($1.2 \times 1.2$ $\mu$m$^2$). We can clearly observe the location of the wires in more detail. One of the wires is disconnected, and we can see that the location of the wire is at the intersection between a step and a terrace. A greater volume

of the wire is located on the lower terrace, while a smaller volume of the wire is located on the higher terrace. The lateral dimensions of the wires can be obtained from Figure 5.2(c) that is a three dimensional rendition of Figure 5.2(b). The typical width of the wires is 150 nm and the average height of the wires is 20 nm; their separation is determined by the width of the terrace $(350 \pm 40)$ nm.

From Figure 5.2 we can conclude, that the terrace-and-step morphology provided by the vicinal sapphire surface is instrumental for the directional growth of rubrene, since only a minor fraction of rubrene can be observed on terraces. Previous studies of rubrene thin film growth [38, 76] indeed suggest that changes in the substrate morphology might be responsible for the observed changes in the thin film growth mode. The rubrene thin film morphology changed from amorphous to polycrystalline, when the sapphire substrate was covered with 1 monolayer of pentacene, and rubrene molecules were found to aggregate along the circumference of the pentacene layer [38]. Also, the geometry of rubrene molecules might play an important role in determining nucleation on sapphire steps. The role of molecular conformation in rubrene thin film growth was studied by Käfer *et al.* [36, 39]. Their X-ray absorption fine structure results obtained on the rubrene films grown on $SiO_2$ and Au(111) substrates show that rubrene molecules retain their gas-phase geometry in the first few molecular layers. The molecules in the subsequent layers were found to assume their bulk geometry. In addition, from the analysis of the dichroism, the authors concluded that rubrene molecules bond onto the substrate forming an angle of 38° between the naphthacene backbone and the Au(111) substrate. No alignment of the molecules was detected in the case of an $SiO_2$ substrate.

Returning to the morphology of the substrate, we recognize that sufficiently long annealing of the vicinal (0001) sapphire surface yields atomically smooth crystalline surfaces and exposes two crystal faces, (0001) and $(11\bar{2}0)$. The latter crystal face exposes the planes comprising oxygen atoms separated by a pair of planes comprising aluminum atoms. The former crystal face is aluminum or oxygen terminated [70]. The step-and-terrace morphology of a vicinal (0001) sapphire surface represents a favorable environment for formation of bonds between phenyl side groups of the rubrene molecule and the oxygen atoms that are exposed in step planes. Therefore we may expect that due to sufficiently high surface mobility the molecules migrate to the location where simultaneous bonding with the naphthacene core and the phenyl groups is possible − the intersection of the two perpendicular planes of a terrace and a step. This is further confirmed by the volume distribution of a wire between the two adjacent terraces. From the fact that a greater volume of the wire is located on a lower terrace we conclude that

the nucleation initiates at the intersection between the lower terrace and the adjacent step. As the growth progresses the intermolecular dispersion forces are sufficiently high to favor further nucleation of the impinging molecules, increasing thereby the overall dimensions of the wires.

The hypothesis of increased sticking coefficient at the terrace/step intersection is further confirmed after inspection of Figures 5.3 and 5.4. Figure 5.3 is a $3 \times 3$ $\mu$m$^2$ AFM image of a vicinal (0001) sapphire surface that we obtained after annealing at 1500°C for 100 h. In addition to terraces and steps, we can observe islands that are $1 - 1.5$ nm high and a few tens of nanometers in diameter. Such morphology of sapphire surface has been observed before, and represents one of the intermediate stages in surface energy relaxation during annealing [6]. To us it is important, since it provides an additional evidence for the nucleation of rubrene.

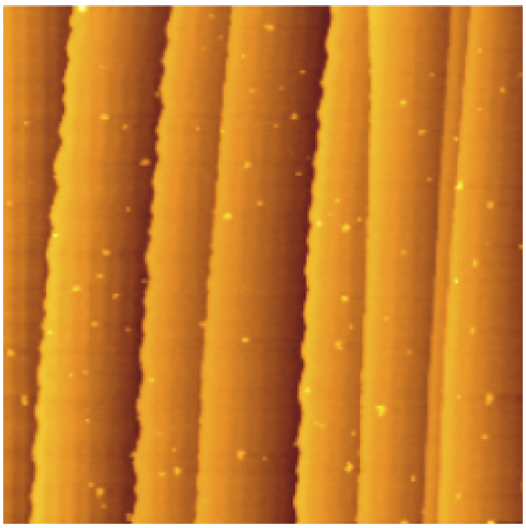

**Figure 5.3:** A $3 \times 3$ $\mu$m$^2$ AFM image of a sapphire substrate annealed at 1500°C for 100 h. Terraces separated by steps can be observed on the surface. In addition, islands measuring $1 - 1.5$ nm in height and a few tens of nanometers in diameter are observed as lighter spots located on the terraces. The islands represent one of the stages in sapphire surface relaxation during annealing.

After the evaporation of rubrene onto such surface we have obtained a morphology that is exemplified in Figure 5.4. In addition to the familiar rubrene wires that are located at the terrace-step intersections, we can observe islands of the same thickness as wires and of a diameter of approximately 200 nm. The location of these islands on the terraces, and their surface density corresponds favorably to the location and surface density of the sapphire islands shown in Figure 5.3.

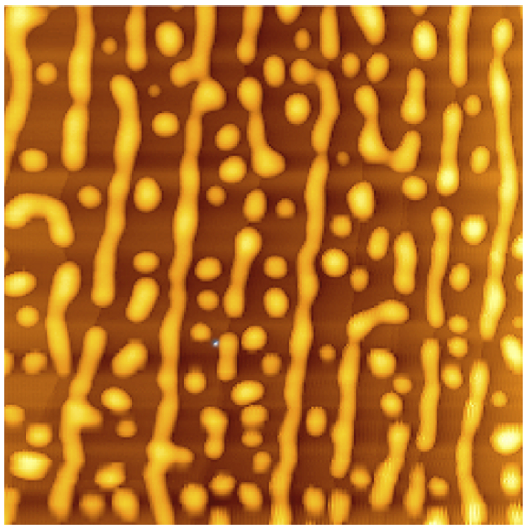

**Figure 5.4:** A $4 \times 4$ $\mu$m$^2$ AFM image of rubrene evaporated onto the annealed vicinal (0001) sapphire surface represented in Figure 5.3. Rubrene was thermally evaporated onto the substrate at room temperature. The nominal thickness of rubrene as determined by in situ quartz microbalance is 10 nm. Rubrene is observed as wires of lighter tones located at the sapphire steps. In addition rubrene islands can be observed on terraces as a consequence of the nucleation of rubrene molecules around the sapphire islands.

To summarize, we have demonstrated that vicinal sapphire surfaces represent a viable option to fabricate arrays of organic semiconductor wires. By controlling the annealing process, we can achieve a well-defined terrace-and-step morphology of the substrate. Such a surface acts as a template for directional rubrene growth. The crucial factor in confinement of rubrene in the area of the intersection between the terrace and the step is the geometry of the molecules. The extreme hydrogen atoms of the naphthacene backbone provide means for attaching the molecules onto the terrace, and the phenyl side groups attach to the step.

## Acknowledgments

We thank Polonca Trebše for helpful discussions. The work was supported in part by the Center of Excellence: Nanoscience and Nanotechnology of the European Regional Development Fund.

# 6 Influence of substrate morphology on growth mode of thin organic films: An atomic force microscopy study

Morphology of high-vacuum deposited thin films of pentacene and rubrene on annealed vicinal (0001) sapphire surfaces was studied by atomic force microscopy in non-contact mode. Pentacene molecules in the first monolayer form two-dimensional islands with an average height of 1.5 nm. The majority of islands nucleate at the steps on the sapphire surface. Surface steps also act as nucleation sites for subsequent monolayers of pentacene. The terrace-and-step morphology of the substrate surface has a larger impact in the case of rubrene thin film growth. Rubrene grows in wire-like structures that follow the direction of the steps. In the case of rubrene films with a nominal thickness of 10 nm, the typical widths and heights of the wires are 150 and 25 nm, respectively. The separation between the wires is determined by the terrace width on the substrate surface. The difference in the morphology of pentacene and rubrene films may be explained by taking into account different geometries of the two molecules.

## 6.1 Introduction

The electronic and optical properties of organic semiconductor (OS) thin films strongly depend on their structure and morphology. Consequently, tailoring these properties requires the ability to control the growth modes of organic materials. Control over the growth of thin films can be achieved by depositing the organic layer on a patterned substrate. Patterned sub-

strates may be obtained through the use of a self-assembled layer [72] or by preparation of substrates with atomically well-defined surfaces [5].

Over the past years, vicinal crystal surfaces have been successfully used to achieve controlled growth on a nanometer scale. In metallic systems, one-dimensional structures were grown on vicinal surfaces by selective decoration of surface steps [73]. Vicinal semiconductor surfaces have also been used as templates for growth of low-dimensional structures. Spatially ordered growth of InAs quantum dots was demonstrated via metalorganic vapor phase epitaxy on step-bunched vicinal GaAs substrates [80]. In organic/inorganic systems, steps on vicinal sapphire surfaces were used to align carbon nanotubes along the step direction [75].

In contrast to inorganic systems, where the physical mechanisms of growth have been successfully exploited to achieve desired control over growth, controlled growth of organic semiconductors is less explored. Controlling the morphology of the organic layer is a difficult task, due to the relatively weak nature of interaction forces between the organic molecule and the substrate. The structure and morphology of the organic layer may strongly depend on the chemical and geometrical properties of the organic molecule.

The present study is an investigation of the influence of the terrace-and-step morphology of the sapphire surface on the growth of high-vacuum deposited thin films of pentacene and rubrene. The use of these two organic semiconductors was motivated by the fact that they show high potential for applications in organic electronic devices [22, 23, 34, 35]. We chose sapphire as the substrate material because of its exceptional physical properties, which have led to its wide use in different applications: as a substrate for thin film growth [30, 38], as a gate insulator in organic field-effect transistors [77], and in laser optics [78].

The following study will show that steps on the sapphire surface influence the morphology of the overgrown organic layer. Our results suggest that the initial stages of growth on stepped sapphire depend on the conformation of the organic molecules forming the overgrown layer.

## 6.2 Experiment

Sapphire surfaces (Cradley Crystal Corp., Roditi Int. Corp. Ltd.), with orientation (0001) and nominal miscuts of 0.2° and 0.55° towards $[11\bar{2}0]$, were prepared by annealing in air at 1500°C for a period between 72 and 120 h. Annealing resulted in a terrace-and-step morphology of the surfaces with average step heights of several nanometers and average terrace widths of several hundreds of nanometers. Annealed substrates were loaded into a

vacuum chamber with a base pressure of $< 10^{-8}$ Torr. To desorb water from the surface, the substrates were heated for 4 h at 200°C. Prior to thin film deposition, the substrates were cooled down to room temperature. Thin films of pentacene (Fluka) and rubrene (Aldrich), with nominal thicknesses from 0.5 to 10 nm, were deposited onto the substrates by evaporation at a nominal rate ranging from 0.5 to 1 nm/min. Thicknesses of layers were determined in situ by a quartz microbalance. Morphology of the films was studied ex situ by an atomic force microscope AFM. The AFM was operated in non-contact mode in order to reduce potential film damage due to the interaction of the microscope tip and the organic film.

## 6.3 Results and discussion

A typical AFM image of the surface of a sapphire substrate after heat treatment is shown in Figure 6.1. Annealing resulted in transformation of the surface morphology from an initial surface, characterized by terraces with typical widths of 100 nm separated by 0.2 nm high steps, to a terrace-and-step morphology with an average terrace width of several hundreds of nanometers and an average step height of several nanometers.

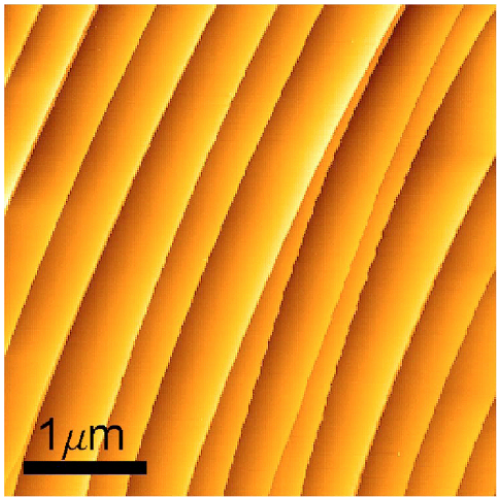


**Figure 6.1:** AFM image of the surface of a sapphire substrate with orientation (0001)+0.55° towards [11$\bar{2}$0] after heat treatment. The substrate was annealed at 1500°C for 120 h. The surface is characterized by a terrace-and-step morphology with an average step height of 2.8 nm and an average terrace width of 350 nm.

Transformation of the (0001) sapphire surface upon high temperature annealing, which results in morphology that is similar to the morphology in Figure 6.1, is well documented [6, 64, 70, 71]. The surface morphology of the

as-received substrates may already be characterized by terraces, separated by 0.2 nm high steps. This height corresponds to one-sixth of the sapphire unit cell size along the (0001) direction [67]. After prolonged annealing, steps coalesce, resulting in an increase of the average step height on the surface [6]. These multiple steps may measure up to 2 nm in height [71]. On the other hand, if the initial surface is rough, annealing leads to formation of 0.2 nm high steps, which then coalesce into multiple steps [64, 70].

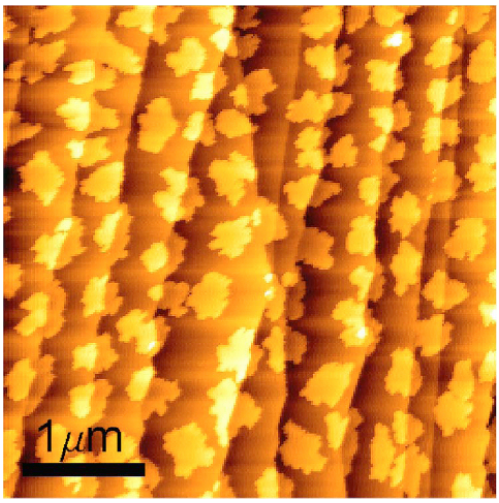


**Figure 6.2:** AFM image of a pentacene film with a nominal thickness of 0.5 nm deposited onto a sapphire substrate by vacuum evaporation. The substrate was annealed at 1500°C for 72 h. The evaporation rate was 0.5 nm/min. Pentacene molecules form two-dimensional islands with an average height of 1.5 nm. The majority of islands nucleate at the steps on the sapphire surface.

Such surfaces were used as substrates for OS thin film deposition. Figure 6.2 shows a sub-monolayer thick film of pentacene, evaporated onto a sapphire substrate at a rate of 0.5 nm/min. Image profiles (not shown here) indicate that pentacene molecules form two-dimensional islands with an average height of 1.5 nm, which corresponds to the long molecular axis being almost perpendicular to the substrate surface [81]. We also note that the majority of pentacene islands nucleate at the steps on the substrate surface. The islands are not connected. The film morphology is consistent with previous observations of growth of pentacene on sapphire [30] and on $SiO_2$ [30, 82]. However, the observed preferential nucleation of islands at the steps has not been reported in Ref. [30]. The difference in the observations may be explained by the different surface morphologies of the substrates used in both studies. The substrates used in this study are characterized by a terrace-and-step morphology with atomically flat terraces of several hundreds of nanometers in width and a step height on the order of several nanometers. On the other

hand, sapphire substrates used in Ref. [30] were polished substrates with no preferential orientation, cleaned with the method described in Ref. [83]. The authors do not report on the average step height on the surface; however, we may assume that the majority of steps on the substrates used in Ref. [30] were 0.2 nm high single steps.

Influence of substrate morphology on growth mode of pentacene can be further explored by taking into account Figure 6.3, which shows a pentacene film with a nominal thickness of 1.7 nm, evaporated onto a sapphire substrate at a rate of 0.5 nm/min. The islands which nucleated during the formation of the first monolayer have already coalesced. The boundary between two islands is indicated by arrow 1 Figure 6.3. The second monolayer of pentacene is characterized by islands with a substantially larger area than the islands of the first monolayer. The third and fourth monolayers of pentacene start to nucleate before the second monolayer is complete, as indicated by arrows 2 and 3, respectively. Note that nucleation of the third and fourth monolayers is initiated at the location of the steps on the sapphire surface (bright areas).

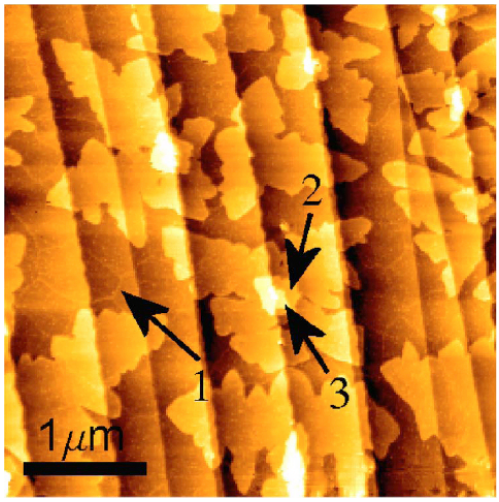


**Figure 6.3:** AFM image of a pentacene film with a nominal thickness of 1.7 nm deposited onto a sapphire substrate by vacuum evaporation. The substrate was annealed at 1500°C for 72 h. Arrow 1 indicates a boundary between two islands of the first pentacene monolayer that have coalesced. Nucleation of pentacene from the third monolayer onward starts at the location of sapphire steps (brighter tones).

From the above observations we can conclude that steps on the sapphire surface influence the positions of pentacene islands of the first monolayer and act as nucleation sites for the third and fourth monolayers of pentacene.

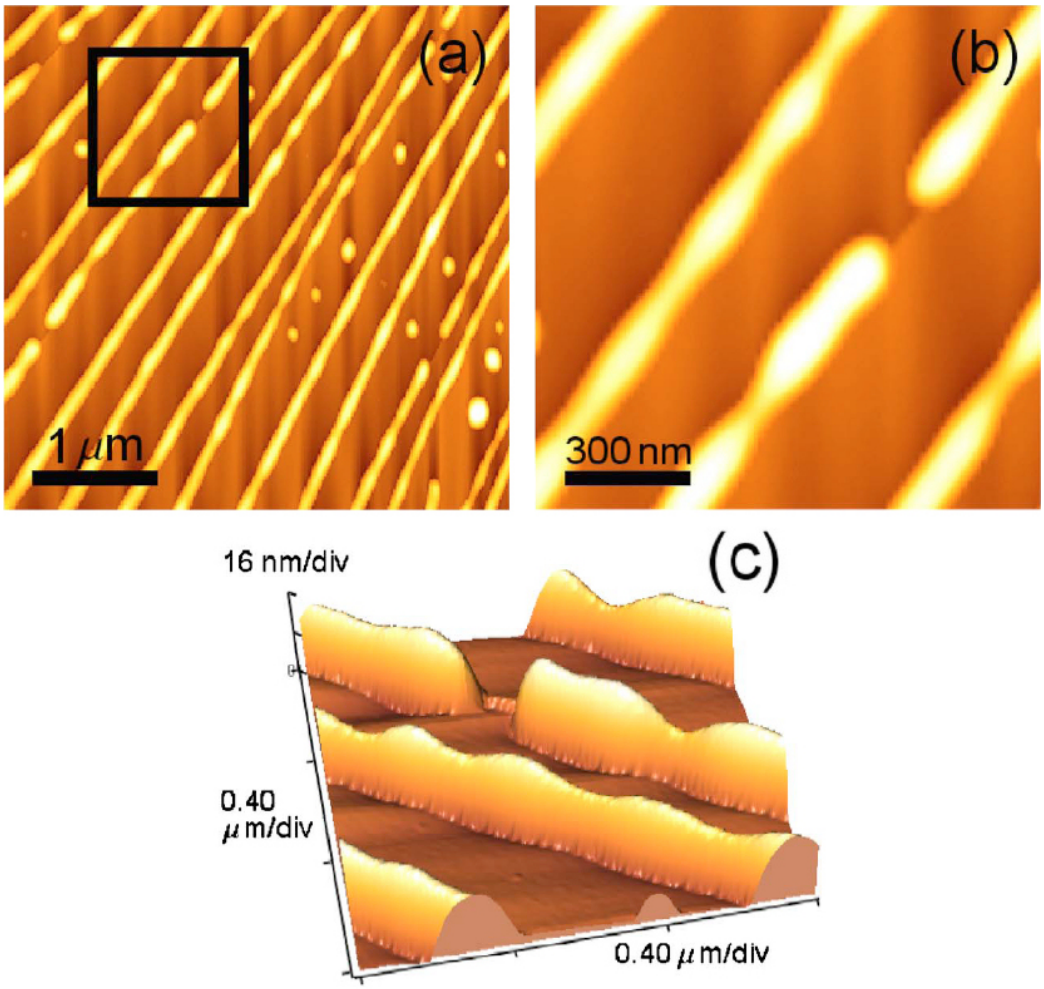


**Figure 6.4:** (a) AFM image of a rubrene film with a nominal thickness of 10 nm deposited onto a sapphire substrate by vacuum evaporation. The substrate was annealed at 1500°C for 120 h. Rubrene grows in wire-like structures along the sapphire steps (brighter tones). (b) Magnification of the boxed area in (a). At the location where one of the wires is disconnected, one can see that the majority of the material resides on the lower terrace, while the other part of the wire is located on the higher terrace. (c) A three-dimensional rendition of (b).

The terrace-and-step morphology of the sapphire surface has a more dramatic effect on the growth of rubrene thin films. Figure 6.4(a) shows a typical AFM image of a rubrene film with a nominal thickness of 10 nm, deposited onto a sapphire substrate at a rate of 1 nm/min. The surface in Figure 6.4(a) is characterized by a regular array of wire-like structures, which follow the direction of steps. All of the wires are located at the surface steps. Only a few isolated rubrene islands can be observed on terraces. Figure 6.4(b) is a magnification of the boxed region in 6.4(a). At the location, where one

of the wires is disconnected, one can see that the majority of the material resides on the lower terrace, while the other part of the wire is located on the higher terrace. From Figure 6.4(c), which is a three-dimensional rendition of Figure 6.4(b), the lateral dimensions of the wires can be obtained. Typical widths and heights of the wires are 150 and 25 nm, respectively. The terrace width on the sapphire surface determines the separation between the wires. In Figure 6.4(a), the average separation between the wires is 350 nm. From Figure 6.4 we can conclude that the terrace-and-step morphology, provided by the vicinal sapphire surface, is instrumental for the directional growth of rubrene, since only a minor fraction of rubrene can be observed on terraces.

The profound difference in the morphology of pentacene and rubrene films on sapphire substrates with a terrace-and-step morphology may be explained by taking into account different geometries of the two molecules. While pentacene is a planar molecule (Figure 6.5(a)), the molecular geometry of rubrene is three dimensional (Figure 6.5(b)) [84]. When pentacene is deposited onto sapphire, the molecules assume a slightly inclined, upright orientation. In the initial stages of growth, pentacene molecules diffuse on the surface of the substrate, until they encounter a site with a minimum surface energy that acts as a nucleation site. Surface steps on sapphire may represent such nucleation sites. Pentacene islands that have already nucleated at the steps act as nucleation sites for other molecules. A diffusing molecule immediately attaches to an island, when it encounters one. This assumption is consistent with the observation of highly ramified pentacene islands on sapphire in Ref. [30]. Further deposition of pentacene therefore results in an increase of the island size, leading to eventual coalescence of the islands. Nucleation of subsequent monolayers of pentacene proceeds in a similar way. The observation that pentacene molecules in the first monolayer form islands and do not grow in elongated structures along the sapphire steps is an indication that the interaction between sapphire steps and pentacene molecules is relatively weak.

While the terrace-and-step morphology of sapphire influences the positions of pentacene islands, it has a larger impact on the growth mode of rubrene. A previous growth study of thin rubrene films suggests that substrate morphology plays an important role during thin film growth [38]. The structure of thin rubrene films changed from amorphous to polycrystalline when sapphire substrates were covered with 1 monolayer of pentacene. Furthermore, rubrene molecules were found to aggregate along the circumference of the pentacene layer. The geometry of rubrene molecules might also affect the nucleation of rubrene at the steps. The role of molecular conformation in rubrene thin film growth was studied by Käfer *et al.* [36]. They observed that the geometry of molecules influences the growth of rubrene on $SiO_2$ and

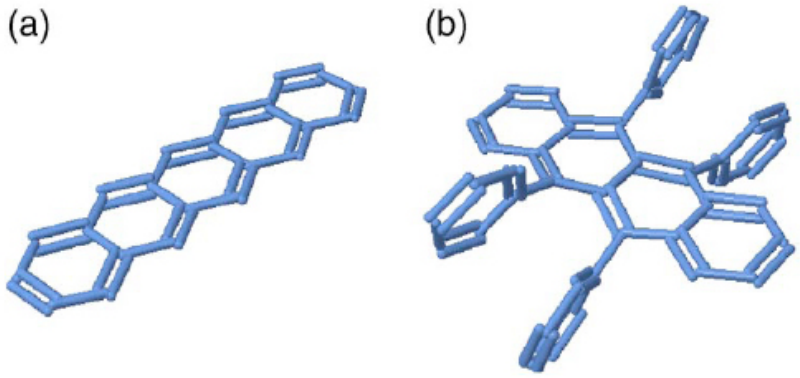


**Figure 6.5:** Molecular geometries of (a) pentacene and (b) rubrene. While pentacene is a planar molecule, the molecular geometry of rubrene is three dimensional. The molecule is composed of a tetracene backbone (four benzene rings) and four phenyl side groups, which may provide additional bonds to the sapphire surface at the steps.

Au(111). Figure 6.4(b) suggests that nucleation of rubrene starts at the sapphire step on the lower terrace. Relatively large steps on the sapphire surface expose several planes of oxygen atoms of the sapphire single crystal. Steps on the sapphire surface may therefore represent a favorable environment for formation of bonds between phenyl side groups of the rubrene molecule and oxygen atoms exposed at the steps. As the growth progresses, the intermolecular forces are sufficiently high to favor further nucleation of the impinging molecules, increasing thereby the overall dimensions of the rubrene wires.

## 6.4 Conclusion

We have investigated the influence of the terrace-and-step morphology of annealed (0001) sapphire substrates on the growth mode of thin films of pentacene and rubrene. In the case of pentacene, steps on the sapphire surface affect the position of pentacene islands of the first and subsequent monolayers. Nucleation of the majority of islands of the first monolayer starts at the location of the surface steps on the sapphire substrate. Steps also act as nucleation sites for the third and fourth monolayers of pentacene. The effect of the terrace-and-step morphology of the (0001) sapphire surface is more profound in the case of rubrene, which grows in wire-like structures along the steps. In the case of rubrene films with a nominal thickness of 10 nm, the typical widths and heights of the wires are 150 and 25 nm, respectively. The separation between the wires is determined by the terrace width on the substrate surface.

# 7 Initial stages of growth of organic semiconductors on vicinal (0001) sapphire surfaces

Initial stages of growth of pentacene, 3,4,9,10-perylenetetracarboxylic dianhydride (PTCDA), rubrene, and $N, N'$-bis(3-methylphenyl)-$N, N'$-diphenylbenzidine (TPD) on vicinal (0001) sapphire surfaces were examined by non-contact atomic force microscopy. Pentacene nucleates at the nm-size steps, however island growth proceeds on the terraces in a layer-plus-island growth mode. PTCDA nucleates randomly at room temperature, while at 135°C and low coverage the molecules aggregate at the steps. At increased coverage the island growth proceeds in the directions determined by the intermolecular interactions and not along the steps. Rubrene and TPD nucleate in 3D islands that evolve over time by ripening. TPD nucleates at the steps and also ripening proceeds along the steps. The ripening rate of rubrene islands is one order of magnitude slower than the ripening rate of TPD islands. We associate this difference to the wealth of rotational degrees of freedom in TPD molecules as opposed to only a twisting degree of the tetracene backbone in rubrene.

## 7.1 Introduction

Most of the new organic optoelectronic devices are based on thin layers of organic semiconductors (OSs). Especially organic thin film transistors often rely on OS layers that are as thin as few molecular layers. Molecular arrangement on the substrate surface is therefore of considerable importance, since any disorder that occurs during initial stages of OS layer deposition may propagate throughout the subsequent layers, and have a detrimental effect

on transport of charge carriers. Growth of OS layers was found to encompass all three major groups of growth modes, layer-by-layer, layer-plus-island and island growth mode depending on the growth conditions and chemical nature of the OS molecules that form the overlayer. The morphology of an overlayer is also, to a great extent, determined by the ratio of interlayer interaction energy and the energy of the interaction between the overlayer and the substrate [85]. When the substrate-overlayer interaction energy exceeds the intralayer interaction energy, the layer-substrate system lowers its total energy by forming a continuous first molecular layer on the substrate. What happens next depends on the amount of strain within the layer. If it is low enough the overlayer continues to grow in a layer-by-layer fashion. For moderate amounts of strain a wetting transition occurs, and three-dimensional (3D) islands form on top of the initial layer. If the interlayer interaction exceeds the overlayer-substrate interaction this results in 3D island formation from the onset of growth.

In addition, surface diffusion of the molecules and their incorporation into existing clusters must be considered when describing the growth phenomena. The mobility of incoming molecules on the surface is governed by the substrate-molecule and the molecule-molecule interactions. The latter plays an important role during deposition of the molecules. In the case of a high flux of incoming molecules the motion of the molecules on the surface is impeded by the intermolecular interactions that result in formation of clusters. The higher the flux of incoming molecules, the higher is the probability of a molecule diffusing on the substrate surface to encounter a new molecule, which effectively reduces the surface mobility of the molecules. Therefore, during initial stages of growth higher molecular fluxes result in morphologies that are characterized by smaller grain sizes. Substrate temperature has similar effect on surface morphology through affecting the surface energy that is available to the diffusing molecules. At increased substrate temperatures islands of larger perimeters are expected since higher surface mobility of the molecules allows them to find optimum positions near the islands [86].

During initial stages of growth the layers may undergo different stages of evolution. After the initial nucleation phase the molecular clusters attract molecules, which move on the surface. After the equilibrium between the number of available sites in the clusters and the number of wandering molecules is reached, the islands may grow only through island-island interaction through a process known as Ostwald ripening [87, 88] that is generally perceived as a last stage in clustering on surfaces. During the ripening phase the islands exceeding a critical size continue to grow, and islands smaller than the critical size decompose and their molecules become consumed by larger islands. Ostwald ripening has been observed on surfaces of inorganic semi-

conductors [89–92], and has been exploited in formation of quantum dots. In organic semiconductors this phenomenon has not yet been observed with the exception of rubrene islands on sapphire [10].

In this paper we present a systematic study of behavior of different organic semiconductors on vicinal (0001) sapphire surface during initial stages of growth. We were interested in the possibility of fabricating ordered structures, and using substrate features as growth templates. During this study we have varied the flux of incoming molecules and substrate temperature to influence the surface mobility of the molecules and the size of crystalline grains. In our study we have explored initial stages of growth of pentacene, 3,4,9,10-perylenetetracarboxylic dianhydride (PTCDA), rubrene, and $N, N'$-bis(3-methylphenyl)-$N, N'$-diphenylbenzidine (TPD). All four semiconductors bear significant technological relevance. For example: pentacene is a prime material for fabrication of organic thin film transistors [22, 93, 94], PTCDA is one of the most investigated OSs, and forms relatively ordered layers on a variety of substrates [3], TPD is a model hole transport material [95], and is widely used in organic light emitting diodes [45], rubrene is becoming increasingly investigated as a high-electron mobility material [96].

For our purposes these materials are interesting also from the point of view of their spatial configuration. Pentacene and PTCDA are planar molecules, while TPD and rubrene molecules have a three-dimensional configuration. In our previous study [8] we have compared the growth mode of pentacene and rubrene on vicinal (0001) surface of $Al_2O_3$. We have found that nanometer-size steps on the surface have little effect on growth of pentacene. These steps, on the other hand, dramatically affect the growth of rubrene which grows predominantly along the steps forming linear structures. There we have suggested that the 3D configuration of rubrene molecules might promote bonding along the steps. In the present paper we have extended the study and added one planar molecule (PTCDA) and one 3D molecule (TPD). We observed striking similarity in behavior during initial stages of growth on stepped sapphire surface among the materials of the same molecular configuration. The molecules that exhibit a planar configuration form randomly distributed islands on the surface, albeit the two materials exhibit different growth modes. Pentacene grows in a layer-plus-island growth mode, while PTCDA forms islands. The molecules that exhibit a three-dimensional configuration grow almost exclusively along the steps forming elongated structures.

## 7.2 Experimental section

Ultra-thin organic films of pentacene (Fluka), PTCDA (Fluka), rubrene (Aldrich), and TPD (Sigma-Aldrich) were deposited onto sapphire surfaces (Cradley Crystal Corp., Roditi Int. Corp. Ltd.) with orientation (0001) and nominal miscuts ranging from 0.2° to 0.55° towards $[11\bar{2}0]$. Prior to thin film deposition the substrates were annealed in air at 1500°C for a period between 72 h and 150 h. This resulted in a terrace-and-step morphology of the surfaces with average step heights of several nm and average terrace widths of several hundred nm. The substrates were transferred to a high vacuum chamber where they were heated for a minimum period of 30 min at temperatures above 200°C in order to desorb water from the surface. Afterwards the substrates were cooled down to room temperature (RT). During deposition of organic materials the temperature of the substrates was controlled with a heater and a thermocouple that was attached to the substrate. Organic material was evaporated from a crucible at a background pressure of $< 10^{-8}$ Torr. The nominal growth rates ranged from 0.3 nm/min to 0.8 nm/min. The growth rates of PTCDA, rubrene, and TPD were determined a posteriori by atomic force microscopy (AFM). Since these organic films do not grow in a layer-by-layer mode, a threshold algorithm was used to estimate the volume of the deposited material per unit area. This value was used as a measure for the thickness of the organic film. It represents the thickness of a hypothetical uniform layer of the organic material. The nominal growth rate is then obtained by dividing the thickness by the evaporation time. In the case of pentacene, the quartz microbalance was calibrated by measuring the pentacene island heights and the area coverage (in percent) of the submonolayer thick pentacene films. The nominal thickness of the submonolayer pentacene film is obtained by multiplying the average island height by the area coverage. Morphology of the films was studied by AFM at ambient conditions. Due to the relatively weak nature of intermolecular forces in the investigated materials the AFM was operated in non-contact mode. During the morphology investigation of TPD and rubrene the AFM tip was translated out of the scanned region after each measurement in order to minimize interference with the growth phenomena that occurred after deposition of the material.

## 7.3 Results

Initial stages of growth of OS investigated in this study are grouped according to the configuration of their molecules. We present the results of

planar molecules (pentacene and PTCDA) first and 3D molecules (rubrene and TPD) second.

### 7.3.1 Pentacene

In Figure 7.1 we show a sequence of surface topographies of 0.5 nm thick pentacene films evaporated onto (0001) vicinal surfaces of sapphire at substrate temperatures (left to right) 28°C, 42°C, and 60°C. The growth rate employed was 0.31 nm/min. The scan size is $4 \times 4$ $\mu$m$^2$. Pentacene molecules form irregularly shaped islands that measure $(1.7 \pm 0.3)$ nm in height, which corresponds favorably to one molecular layer of the thin film phase of pentacene [81]. We have used a threshold algorithm after the morphological features of the substrate were removed from the AFM images to extract the shape of the islands. The areal density of the islands is $(3.6 \pm 0.5)$ $\mu$m$^{-2}$, $(1.3 \pm 0.3)$ $\mu$m$^{-2}$, and $(0.21 \pm 0.06)$ $\mu$m$^{-2}$, which corresponds to island sizes of $(0.078 \pm 0.010)$ $\mu$m$^2$, $(0.20 \pm 0.04)$ $\mu$m$^2$, and $(1.00 \pm 0.35)$ $\mu$m$^2$ for the substrate temperatures of 28°C, 42°C, and 60°C, respectively.

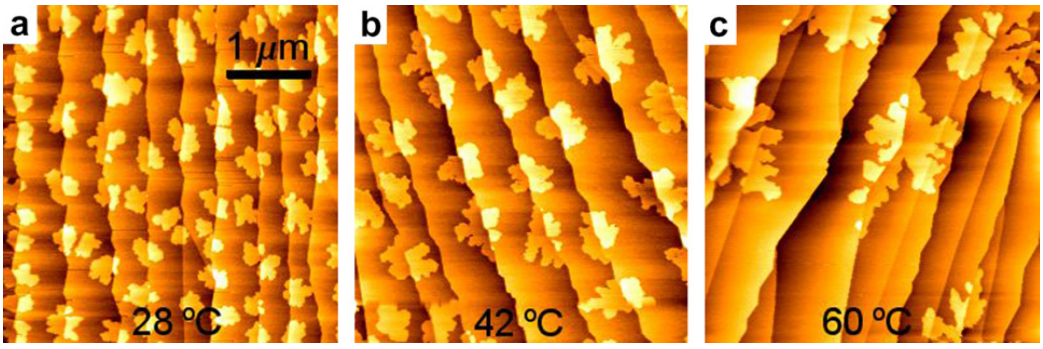


**Figure 7.1:** Sequence of surface topographies of 0.5 nm thick pentacene films evaporated onto (0001) vicinal sapphire surfaces obtained by annealing at 1500°C. Different images correspond to different substrate temperatures: (a) 28°C, (b) 42°C, and (c) 60°C. Pentacene was evaporated at a rate of 0.31 nm/min. The scan size is $4 \times 4$ $\mu$m$^2$ in all figures. Pentacene can be seen in the form of irregularly shaped islands with an average height of 1.7 nm. A substantial fraction of islands with their centers at the sapphire steps is observed at all temperatures. As the temperature increases the island density decreases and the average island size increases. At 60°C some of the islands are elongated along the step direction.

From Figure 7.1 it is evident that the spatial distribution of the islands is different from purely random. In addition to a decrease of the island density (and corresponding increase of the average island area) with temperature, we note an increase in fractal morphology of the island with increasing substrate temperature. The islands nucleate and grow almost regardless of the

substrate surface morphology, although the majority of the islands nucleate at the steps and spread on both terraces defining the step. By increasing the substrate temperature we obtain larger islands (Figure 7.1(b) and (c)), while their areal density decreases. At 60°C some of the islands, while maintaining the monolayer thicknesses, encompass several terraces. Similar behavior of the island size was observed when we varied the flux of incoming molecules. We have explored the morphology of the pentacene islands at nominal growth rates of 0.04 nm/min, 0.47 nm/min, and 4.9 nm/min at RT. The average island size, was found to be $(0.56 \pm 0.20)$ $\mu$m$^2$, $(0.073 \pm 0.010)$ $\mu$m$^2$, and $(0.02 \pm 0.002)$ $\mu$m$^2$ for the growth rates of 0.04 nm/min, 0.47 nm/min, and 4.9 nm/min.

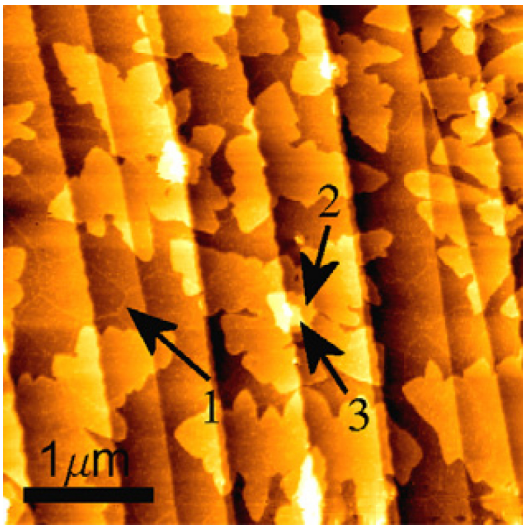


**Figure 7.2:** Topography of a pentacene film with a nominal thickness of 1.7 nm deposited onto a (0001) vicinal sapphire surface obtained by annealing at 1500°C. The growth rate was 0.5 nm/min, and the substrate was at RT. The scan size is $4 \times 4$ $\mu$m$^2$. Pentacene islands in the first monolayer coalesce and form a complete monolayer. Arrow 1 indicates a boundary between two such islands. Islands with a substantially larger area characterize the second monolayer. Nucleation of pentacene in the third and fourth monolayer initiates at the location of sapphire steps (Arrows 2 and 3).

Further evidence of the role of steps as nucleation centers for pentacene may be obtained from Figure 7.2, where we show a $4 \times 4$ $\mu$m$^2$ scan of a nominally 1.7 nm thick pentacene layer grown at 0.5 nm/min. We see that increasing the amount of evaporated material causes coalescence of islands and formation of a continuous pentacene layer, of which we can observe only grain boundaries (indicated by Arrow 1 in Figure 7.2). The islands in the second monolayer already passed the nucleation stage and continue to grow, the islands in the third and the fourth layer are in their nucleation stage

(Arrows 2 and 3 in Figure 7.2). Here we emphasize that the nucleation of the third and fourth monolayers initiates exclusively at the location of the steps.

### 7.3.2 PTCDA

Initial stages of growth of PTCDA on sapphire are less spatially correlated than in the case of pentacene. This is evident from Figure 7.3, where we show a nominally 0.3 nm thick PTCDA film evaporated onto a sapphire surface at RT, using a growth rate of 0.7 nm/min. The scan size is $1 \times 1$ $\mu$m$^2$. We see that PTCDA molecules aggregate to form smooth islands with an average projected area of 220 nm$^2$ and an average height of 2.0 nm. Nucleation initiates with the same probability on terraces, as well as at the steps.

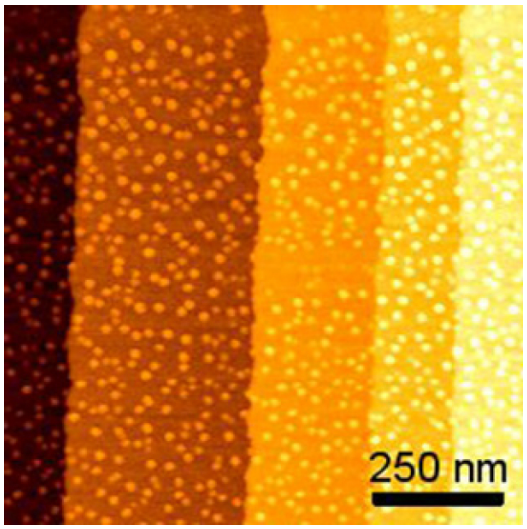


**Figure 7.3:** A $1 \times 1$ $\mu$m$^2$ AFM image of the morphology of a 0.3 nm thick PTCDA film deposited onto a (0001) vicinal sapphire surface obtained by annealing at 1500°C. The growth rate was 0.7 nm/min, and the substrate was at RT. PTCDA can be seen in the form of 3D islands with an average projected area of 220 nm$^2$, average density of 940 $\mu$m$^{-2}$, and an average height of 2.0 nm. The islands are randomly distributed over the substrate surface.

In order to investigate the possibility to induce templated growth of PTCDA at sapphire steps we have increased the substrate temperature and varied the PTCDA coverage. Typical results are shown in Figure 7.4. Here we show the morphology of PTCDA evaporated at 135°C at coverages of 0.3 nm, 1.6 nm, and 3.3 nm, using a growth rate of 0.7 nm/min. At the lowest coverage (Figure 7.4(a)) we note that the majority of islands start to nucleate at the steps. As the coverage increases the steps remain preferred

nucleation sites, however some of the islands grow in size due to capture of additional material and/or elongate in the directions that are oblique or perpendicular to the step lines. Increasing further the coverage (Figure 7.4(c)) we obtained further enlargement of the islands and no significant increase in the correlation of the island positions with the steps.

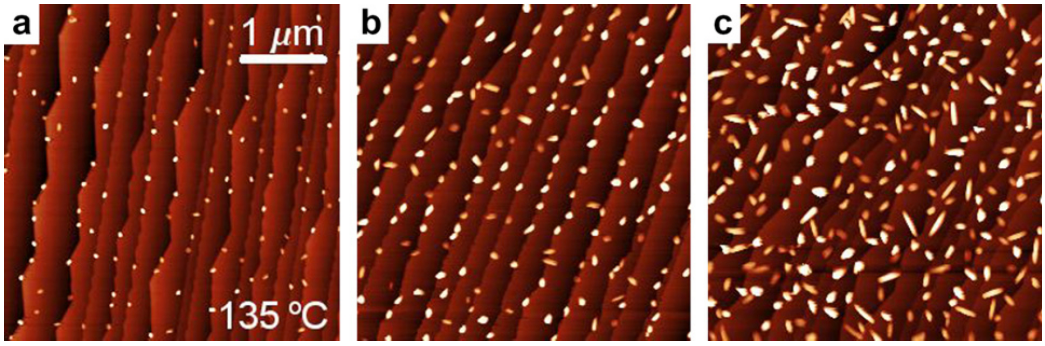


**Figure 7.4:** Sequence of surface topographies of PTCDA films evaporated onto (0001) vicinal sapphire surfaces obtained by annealing at 1500°C. The scan sizes are $4 \times 4$ $\mu$m$^2$. Different images correspond to different PTCDA film thicknesses: (a) 0.3 nm, (b) 1.6 nm, and (c) 3.3 nm. The growth rate employed was 0.7 nm/min and the substrate temperature was 135°C. (a) PTCDA molecules aggregate in 3D islands with an average island size of 2500 nm$^2$ and an average island density of 8 $\mu$m$^{-2}$. A vast majority of islands nucleate at the steps. (b) At increased coverage preferred nucleation is still observed at the steps; however, some of the islands elongate in the directions that are oblique to the steps. (c) In thicker films the island size increases. There is no significant increase in the correlation between the island positions and orientations and the step direction.

### 7.3.3 Rubrene

Substantially different morphology was obtained by evaporation of rubrene and TPD onto vicinal (0001) sapphire surfaces. A typical AFM image of a 2.3 nm thick rubrene film deposited at RT at a rate of 0.3 nm/min is shown in Figure 7.5(a). The image was obtained 30 min after completion of evaporation. At this coverage rubrene molecules aggregate in 3D islands with an average projected area of 5000 nm$^2$, average density of 27 $\mu$m$^{-2}$, and an average height of 12 nm. Although the majority of islands nucleate on terraces there is some indication of preferred nucleation at the steps. By monitoring the morphology of rubrene on sapphire over time we have found that the density and size of the islands change (Figure 7.5(b) and (c)). After 48 h (Figure 7.5(c)) the island density decreases by more than an order of magnitude to an average value of 0.75 $\mu$m$^{-2}$. This results in an increase of the average island size and height to 63000 nm$^2$ and 50 nm, respectively. We

note that the volume of deposited material is conserved over time. After 48 h the morphology of rubrene islands stabilizes. As the morphology of rubrene islands evolves we see that an increasingly larger fraction of islands is observed at the sapphire steps and after 48 h all islands are observed at the steps on the surface. Ripening of rubrene islands was studied in detail in Ref. [10] where it was observed that the density of rubrene islands on as-received substrates decreases with time. The decrease is stabilized after a period of approximately 30 h. The observations of morphological changes of rubrene islands are therefore qualitatively similar in the case of annealed and as-received sapphire substrates.

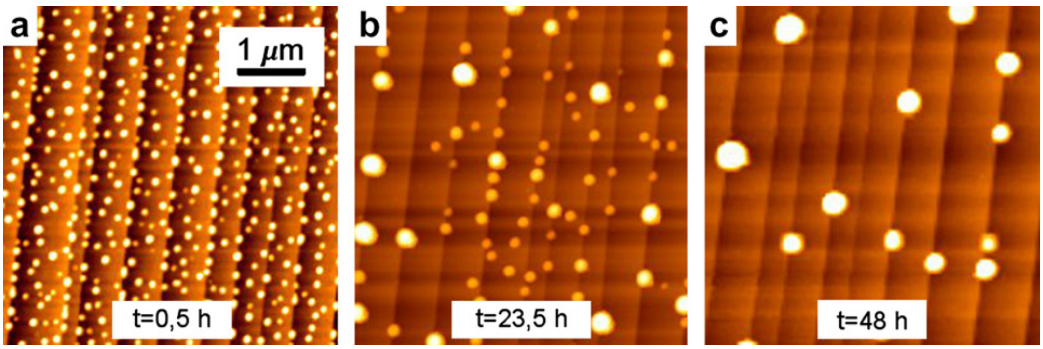


**Figure 7.5:** Sequence of surface topographies of a 2.3 nm thick rubrene film evaporated onto a (0001) vicinal sapphire surface obtained by annealing at 1500°C. $4 \times 4$ $\mu$m$^2$ AFM images represent the time evolution of the morphology of a rubrene film deposited at a rate of 0.3 nm/min. The substrate was held at RT. (a) Immediately after deposition rubrene can be seen in the form of 3D islands with an average area of 5000 nm$^2$, average density of 27 $\mu$m$^{-2}$, and an average height of 12 nm. (b) After 23.5 h the island density exhibits a substantial decrease. The fraction of islands at the surface steps increases. (c) After 48 h the island density decreases by more than an order of magnitude to an average value of 0.75 $\mu$m$^{-2}$. The islands size and height increase to 63000 nm$^2$ and 50 nm, respectively. After 48 h the morphology of the rubrene film stabilizes. All of the rubrene islands are located at the surface steps.

At increased coverage rubrene islands coalesce and eventually form elongated structures which follow the direction of the sapphire steps. Immediately after deposition of the material stops there is also a substantial quantity of material on terraces (not shown). After several hours the molecules arrange almost exclusively at the location of the steps. This is exemplified in Figure 7.6 where we show a 7 nm thick rubrene film deposited onto a sapphire substrate held at RT at a rate of 0.3 nm/min. The image was obtained 15 h after evaporation. After 48 h these linear structures decay into 3D islands due to ripening (not shown). Our previous data [7] show that the resulting structures are located at the steps with the majority of the material on the lower terrace and the minority of the material on the

higher terrace. Typically the structures measure from 150 nm to 200 nm in width and approximately 25 nm in height. Their separation is determined by the width of the terraces on the sapphire surface. We have also found [7] that rubrene molecules tend to aggregate and form islands at the location of surface defects whose height is on the order of 1 nm. These defects are sometimes observed on the surface of sapphire after annealing.

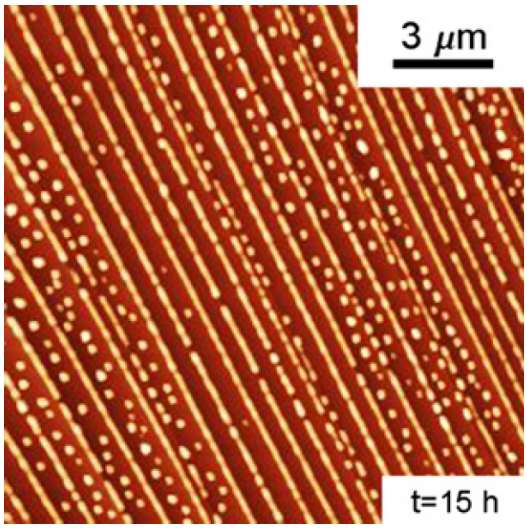


**Figure 7.6:** $10 \times 10$ $\mu$m$^2$ AFM image of a 7 nm thick rubrene film evaporated onto a (0001) vicinal sapphire surface, obtained by annealing at 1500°C, at a rate of 0.3 nm/min. The substrate was held at RT. The image was obtained 15 h after deposition. Rubrene can be seen in the form of elongated structures which follow the direction of the sapphire steps. Typical widths and heights of the structures are from 150 nm to 200 nm and 25 nm, respectively. A minor fraction of rubrene in the form of 3D islands can also be seen on terraces.

### 7.3.4 TPD

Similar growth behavior as in thin rubrene films was observed in thin films of TPD. TPD also exhibits island ripening after deposition of the organic material has stopped. This is exemplified in Figure 7.7, where we show the morphology evolution of a 0.3 nm thick TPD film grown on a vicinal sapphire surface at RT and a rate of 0.6 nm/min. However, in the case of TPD we see that spherical islands nucleate exclusively at the steps. Island ripening is observed even after 1 hour upon completion of growth (Figure 7.7(b)). After 5.5 h (Figure 7.7(c)) the morphological features of the film are substantially different as compared to the morphology of the film after 0.33 h; however, we observe that the positions of TPD islands are confined to the sapphire

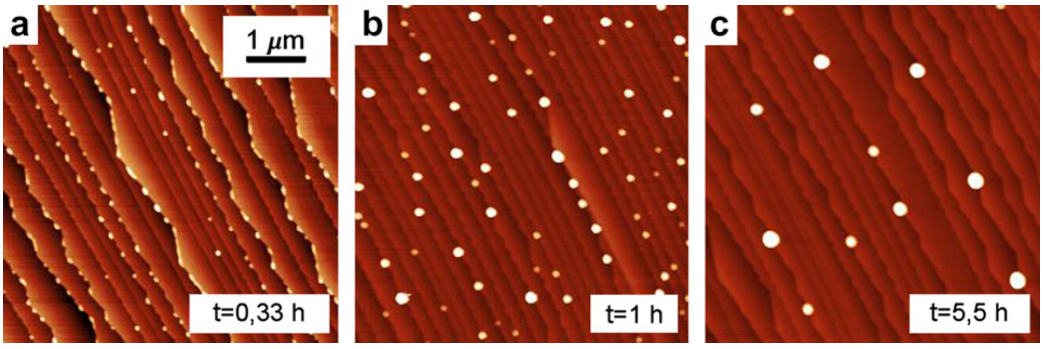


**Figure 7.7:** Sequence of surface topographies of a 0.3 nm thick TPD film evaporated onto a (0001) vicinal sapphire surface obtained by annealing at 1500°C. $4 \times 4$ $\mu$m$^2$ AFM scans represent the time evolution of the morphology of a TPD film. The material was deposited at a rate of 0.6 nm/min. The substrate was held at RT. (a) Immediately after deposition TPD can be seen in the form of 3D islands that are confined to the steps on the sapphire surface. (b) and (c) As time progresses ripening of TPD islands is observed. Throughout the ripening process the positions of TPD islands are confined to the location of steps on the substrate surface.

steps. By comparing Figures 7.7 and 7.5 we see that ripening of TPD islands is an order of magnitude faster than rubrene island ripening. If we increase the thickness of TPD to 2.8 nm, and allow the film to relax for 0.5 h we can achieve a morphology that is characterized by linear structures with typical widths of 100 nm and heights of approximately 6 nm. These structures decorate the steps on the sapphire substrate as exemplified in Figure 7.8 which shows an AFM image of a 2.8 nm thick TPD film deposited at a rate of 0.8 nm/min onto a sapphire substrate held at RT. After several hours the structures decay into 3D islands due to ripening as in the case of rubrene (not shown).

## 7.4 Discussion

By comparing the behavior of all four materials in the initial stages of growth we may conclude that the ability of the substrate features to control the nucleation of the incoming molecules is characteristic to molecules that exhibit substantial surface mobility and even post-growth ripening. Growth of pentacene in its initial stages on insulating substrates such as $SiO_2$ is well documented [55, 82, 97–99], and our results on vicinal surfaces of sapphire agree well with these findings. We observe islands of dendritic shape with size and spatial density that vary with substrate temperature and flux of incoming molecules. Similar behavior is reported by Pratontep *et al.* for the dependence on the growth rate and for the dependence on the substrate tem-

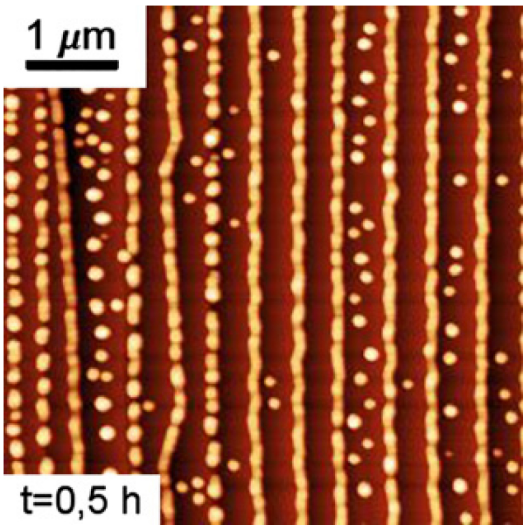


**Figure 7.8:** $4 \times 4$ $\mu$m$^2$ AFM image of the morphology of a 2.8 nm thick TPD film deposited onto a vicinal sapphire substrate at a rate of 0.8 nm/min. The substrate was held at RT. The image was obtained 30 min after evaporation. TPD can be seen in the form of linear structures with typical widths of 100 nm and typical heights of 6 nm. The structures follow the direction of the steps on the substrate surface.

perature [55, 98]. The shape and density of the islands observed in Figure 7.1 are a result of interplay between surface diffusion, nucleation, re-evaporation and incorporation of the molecules into existing islands. Dendritic shape of the islands is a signature of diffusion-limited aggregation [99, 100]. We see that by increasing the substrate temperature the degree of branching is increased (cf. Figure 7.1(a-c)). As pointed out in Ref. [99], dendritic shapes of the islands are a signature of the molecular hopping time on the substrate surface being much smaller than the hopping time at an island edge. This means that when a diffusing molecule attaches to an island its mobility is strongly reduced as compared to the mobility on the sapphire substrate. From the deviation of the spatial distribution of the islands from pure randomness (Figure 7.1) we conclude that steps indeed act as preferred nucleation sites. It is interesting however, that the island that nucleates at the lower terrace always has its neighboring island on the upper terrace, and we never observe dendrites near the step edge. In the absence of detailed data on the early stages of nucleation we can only speculate that the mobility of pentacene molecules near the vertical face of the step or at the step edge is affected by the local energy minimum to such degree as to favor bonding near an island already present. The preference of nucleation of pentacene islands at the steps is further confirmed by inspecting Figure 7.2 where we observe the onset of nucleation of a third and fourth layer (Arrows 2 and 3,

respectively) at the step edge. We note that despite the fact that pentacene islands nucleate at the step edges the growth continues radially away from the nucleation site and not along the step. Clearly molecular mobility near the islands is strongly reduced, and the molecules become attracted to the islands. This is in agreement with the capture zone concept [55], in which a mean distance in which the molecule is attracted to an existing island exists. If we assume that the nucleation site is at the step, and that the diffusion (Ehrlich-Schwoebel) barrier at the step edge precludes the motion of the molecules on a lower terrace, and that the probability for molecules to hop to an upper terrace is low, the perimeter of the capture zone can extend only away from the step on the same terrace.

In contrast to pentacene that nucleates at the steps from the initial stages of growth at RT, and experiences island growth on terraces, PTCDA forms randomly distributed islands, regardless of the surface corrugation (Figure 7.3). Note that we observe ordering of PTCDA molecules along the steps only upon heating the substrate to 135°C. We have observed similarly that at low coverages (Figure 7.4(a)) PTCDA molecules prefer sites at the steps, which may be explained by relatively weak interaction with the substrate and consequently high surface mobility. However, as the coverage increases (Figure 7.4(b)) intermolecular bonding overcomes the molecular interaction with the substrate steps, and we start to observe elongated structures oblique to the step lines. These structures dominate as the coverage increases (Figure 7.4(c)). It is apparent that PTCDA molecules interact with the substrate at RT strongly enough to suppress surface mobility and result in randomly distributed islands (Figure 7.3). This is somewhat at variance with the results by Nony *et al.* [101], who studied PTCDA growth on KBr(001) substrates that were electron irradiated. The resulting surface comprised nanometer-size rectangular pits of one atomic layer in depth. The authors found that PTCDA molecules aggregated in these pits or decorated the borders of the larger pits. The strength of molecule-substrate interaction that affects molecular surface mobility is therefore different for the two insulators (KBr(001) and $Al_2O_3$). Comparing with pentacene we see similar behavior in the sense that island nucleation initiates at the steps, while island growth continues from the nucleation sites in directions that are not related to the directions of the steps. Growth of OSs with an aromatic molecular core on insulating substrates is therefore difficult to reconcile with the activity of the molecular reaction center around which a molecule could rotate to accommodate for an optimum position relative to the substrate lattice, and which was accounted for quasi-epitaxial growth of PTCDA on metallic substrates [102]. The localized molecular reaction center could however provide means for molecular rotation and adjustment of interaction to existing islands.

Both pentacene and PTCDA comprise 2D molecules that exhibit island growth that is determined mostly by the ability of molecules to sense a specific site at the existing island. Such precise accommodation might also be the reason for stability of both pentacene and PTCDA layers on a variety of substrates. As we see from Figures 7.5-7.8, rubrene and TPD behave similarly to each other, and differently than pentacene and PTCDA in terms of initial stages of growth. Both OSs comprising 3D molecules exhibit substantial surface mobility, moreover they both experience Ostwald ripening, as seen from Figures 7.5 and 7.7. Here we note that the rate of ripening in TPD exceeds the rate of ripening of rubrene islands by almost an order of magnitude. In addition we observe almost immediate decoration of steps by TPD islands (Figure 7.7(a)), while in the case of rubrene the process of readjustment of islands along the steps may take as long as 48 h (Figure 7.5). Such superior surface mobility of TPD relative to rubrene and of course relative to the 2D molecules investigated in this work may have a reason in the coordination of the molecule. Synchrotron X-ray diffraction studies of TPD in the solid-state show that the molecular structure exhibits substantial rotation in the four terminal aryl rings [49]. Upon arriving onto the surface TPD molecules may therefore relatively easily accommodate for different atomic environment and adjust their geometry until they arrive at the site with two perpendicular surfaces, where they become confined and allow to move only along the steps. This results in coarsening of the islands (Figure 7.7), and eventually leads to a formation of wires if there is enough material present (Figure 7.8). Rubrene molecule also exhibits conformational changes upon arriving from the gas phase onto the substrate surface. The 42° twist of the tetracene backbone that is present while the molecule is in the gas phase vanishes in the solid-state [36]. Changes from a twisted to a flat backbone might help accommodate the molecular orientation on the surface until the molecule reaches a surface step that confines the molecular movement in one dimension and allows island coarsening and formation of elongated structures. While the TPD molecule exhibits several rotational degrees of freedom (individual aryl rings as well as individual phenyl rings), the rubrene molecule exhibits only a twist of the tetracene backbone. We suggest that such important difference in molecular configuration may be responsible for substantially faster island coarsening of TPD relative to rubrene. In addition, both TPD and rubrene molecules have side rings that may provide additional bonding to the surface at the steps, which would explain preferential nucleation at these sites. On the other hand both 2D molecules show no changes in coordination upon arrival onto the surface, and exhibit substantially lower surface mobility than the 3D molecules.

## 7.5 Conclusions

We performed AFM studies of initial stages of growth of OSs by grouping the molecules according to their coordination. We have found that OSs with 2D molecules such as pentacene and PTCDA exhibit lower degree of surface mobility on vicinal surface of sapphire. While pentacene nucleates at the nm-size steps its island growth proceeds in a dendritic fashion on the terraces, eventually covering the whole substrate with a single molecular layer. PTCDA molecules instead anchor themselves randomly on the substrate at RT. At 135°C the surface mobility is increased so that the molecules tend to aggregate at the steps. At increased coverage the intermolecular interactions prevail and the islands grow in the directions determined by these interactions rather than exclusively along the steps. 3D molecules (rubrene and TPD) diffuse on the sapphire surface much more freely than 2D molecules. We have found that the interactions with the substrate are so weak that island ripening is the primary mechanism that follows nucleation. Moreover, especially TPD molecules immediately sense the positions at the steps and ripening proceeds exclusively along the steps. We observe an order of magnitude faster rate of ripening for TPD relative to rubrene. We associate this difference with several rotational degrees of freedom that are present in TPD molecules, while rubrene molecules exhibit only twisting of the tetracene backbone.

## 7.6 Acknowledgments

We acknowledge helpful discussions with A. Petrović and P. Škraba. This work has been financed in part by ERDF, Center of Excellence Nanoscience and Nanotechnology.

# 8 Ripening of rubrene islands

We investigate the time evolution of morphology of thin rubrene films on sapphire surfaces using atomic force microscopy. The results show that after deposition of rubrene has stopped the density of rubrene islands decreases with time while the average island size increases. In addition, the process of island ripening is strongly temperature dependent. At 50°C, we observe a time dependence of the island density that is consistent with the existence of a kinetic surface barrier for the molecules to detach from the islands. The experimental data indicate that, at room temperature, defects on the sapphire surface play a dominant role in the process of rubrene island ripening.

## 8.1 Introduction

Initial stages of growth of organic semiconductor (OS) films have profound effects on the morphology of subsequent layers. Morphology, in turn, strongly affects the electronic properties of OS layers; it is therefore essential to understand the mechanisms that govern the arrangement of molecules in early stages of nucleation. Growth of OS layers during vacuum evaporation is characterized by a complex interplay between adsorption of molecules onto a substrate, their diffusion on the substrate surface, and their aggregation into clusters that act as nucleation sites for larger islands. When OSs are deposited onto inert substrates, organic molecules exhibit relatively weak interactions with the underlying surface. The arrangement of molecules on the surface is therefore determined by comparatively stronger intermolecular interactions. This may lead to a relatively ordered growth regardless of a considerable lattice mismatch between the two materials [103, 104], a process known as quasi-epitaxy [105, 106]. Three distinctive growth modes, layer-by-layer (Frank-van der Merve), layer-plus-island (Stranski-Krastanov), and island (Volmer-Weber) growth mode, first established in growth of inorganic semiconductors, have also been confirmed in OS thin film growth. Ultrathin films of PTCDA, which is one of the most thoroughly studied organic com-

pounds [3], exhibit a layer-by-layer growth mode [16, 107], whereas molecules in thicker films assemble in three-dimensional (3D) islands, which results in a Stranski-Krastanov (SK) [16] or a Volmer-Weber growth mode [108, 109].

The resulting morphologies obtained in growth studies of thin OS layers appear to be stable with time after the deposition of the organic material has stopped. Pentacene, for example, is known to exhibit diffusion mediated growth on oxidized silicon surfaces, which involves four qualitatively different steps [97]. When the molecules encounter the surface of the substrate, they diffuse until a critical number of them meets and a stable cluster is formed. Subsequently, the molecules continue to nucleate new islands but also aggregate into existing ones. The next step is the aggregation regime where the incoming molecules attach only to already existing islands. In the last stage, the monolayer islands coalesce. Similar mechanisms are present during deposition of subsequent layers, only this time, the molecules diffusing on the $n$th layer can either nucleate and contribute to the growth of the $(n+1)$th layer or transfer downward and contribute to the growth of the $n$th layer [110]. After deposition of the material has stopped, the pentacene film exhibits a stable layered structure.

Following a more general scenario of clustering on surfaces, the islands that have nucleated in the initial stages of growth may evolve with time after deposition of the material has stopped. The last stage may involve coalescence of clusters or transformation of clusters by a mechanism known as Ostwald ripening (OR) [85, 87, 88, 111]. During this process, islands exceeding a critical size grow, while islands smaller than the critical size decompose and are eventually incorporated into larger islands. This last stage of clustering has been confirmed and systematically investigated in inorganic systems comprising quantum dots [89–92]. Since molecules are extended objects - which introduces additional degrees of freedom - and since the interactions between organic molecules are different than the atom-atom interactions in inorganic semiconductors, it is of fundamental importance to investigate whether the last stage of clustering can also occur in systems comprising OS thin films.

In this study, we investigate thin films of the organic semiconductor rubrene deposited onto (0001) sapphire surfaces. We observe that the resulting morphology of the films is unstable and evolves with time after deposition of the organic material has stopped. Since the electronic and optical properties of OS films depend on the morphology of the organic layer, the observed ripening of rubrene films may have significant practical implications.

## 8.2 Experimental section

Rubrene (Aldrich) was evaporated onto as-received (0001) sapphire surfaces (Roditi Int. Corp. Ltd.) in a vacuum chamber with a base pressure of $5 \times 10^{-9}$ Torr. Prior to deposition of rubrene, the substrates were heated at temperatures above 200°C to desorb water from the surface. During deposition of rubrene, the substrates were held at room temperature. Upon completion of evaporation, the samples were immediately examined with an atomic force microscope (AFM) which was operated in air. In order to reduce the interaction of the microscope tip with the organic film, all AFM measurements were performed in tapping mode.

Since thin rubrene films exhibit a morphology characterized by 3D islands which leave a portion of the substrate uncovered, a threshold algorithm was used to measure the volume of the deposited material per unit area. This was used as a measure for the thickness of rubrene films. It represents the thickness of a hypothetical uniform layer of rubrene. The growth rate and thickness of rubrene films calculated with this method were 0.28 nm/min and 1.6 nm, respectively. Alternatively, we could use the fraction of the area covered by rubrene islands as a measure of the deposited material; however, coverage defined in this way changes with time after deposition of rubrene has stopped as a result of island ripening. Nevertheless, the fraction of the area covered by rubrene islands 30 min after evaporation was 0.2 in all cases.

The surface of the samples was repeatedly scanned in intervals ranging from 30 min to several hours. During each measurement, the scan size was adjusted so that a sufficient number of islands was observed in the scanned area. Each time a threshold algorithm was used to confirm that the total volume of the deposited material is conserved over time (i.e., there is no desorption of rubrene molecules from the sapphire surface). To further minimize the influence of the experimental procedure on the dynamics of the processes occurring on the surface, the AFM tip was translated out of the scanned region after each measurement. As for the scan rate: to ensure minimum interference with the ongoing surface processes, care was taken to examine the surface as quickly as possible, so that the imaging time was short in comparison to the interval between measurements.

Two types of measurements were performed, each at a different temperature. In the first set of measurements, the temperature of the samples was controlled with a PID temperature controller and a heater that was attached to the AFM scanner. During the measurement, the temperature of the samples was maintained at 50°C. The other set of samples was investigated at room temperature.

## 8.3 Results and discussion

Figure 8.1 illustrates how the morphology of a thin rubrene film develops with time after deposition of the organic material has stopped. The images correspond (left to right) to initial, middle, and final phases of the ripening process of a sample maintained at 50°C. Initially (Figure 8.1(a)), we observe a number of spherical islands, indicating that the dominant growth mode of rubrene on sapphire under selected conditions is of a Volmer-Weber type that is typical for systems where the interaction between the molecules exceeds the substrate-molecule interaction [54]. We see that the size distribution of the islands spans a substantial range in the figure. As time progresses we observe increasingly higher ratio of larger islands (Figure 8.1(b), (c)) and a decrease in the island density. The shape of the islands remains self-similar throughout the period of examination.

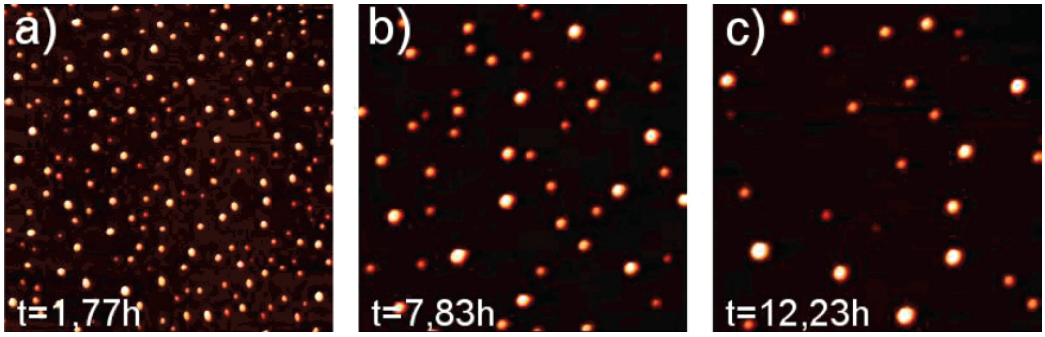


**Figure 8.1:** Consecutive AFM images of a thin rubrene film showing the process of island ripening. The temperature of the sample was maintained at 50°C. The image size is $5 \times 5$ $\mu$m$^2$ in all cases.

The island density was determined from a series of images with a threshold algorithm. Figure 8.2 shows the island density (in $\mu$m$^{-2}$) as a function of time for samples maintained at 50°C (filled circles) and 28°C (filled triangles) on a double-logarithmic scale. The initial island density is similar at both temperatures; however, subsequent evolution of the surface morphology is compellingly different. Focusing on the high-temperature data first, we see that the island density monotonically decreases for a period of approximately 13 h, and after that the decrease is stabilized. The solid line represents a least-square fit of the island density $\rho(t) \propto t^{-a}$ with $a = 1.05 \pm 0.02$. Such behavior was observed, e.g., during ripening of CdSe quantum dots on ZnSe substrates [112]. At the core of the behavior predicted by the model is the mean field theory of OR [85, 88, 111].

The hydrodynamic approximation of OR was introduced by Lifshitz and Slyozov [111] using an approach in which spherical grains in a supersaturated

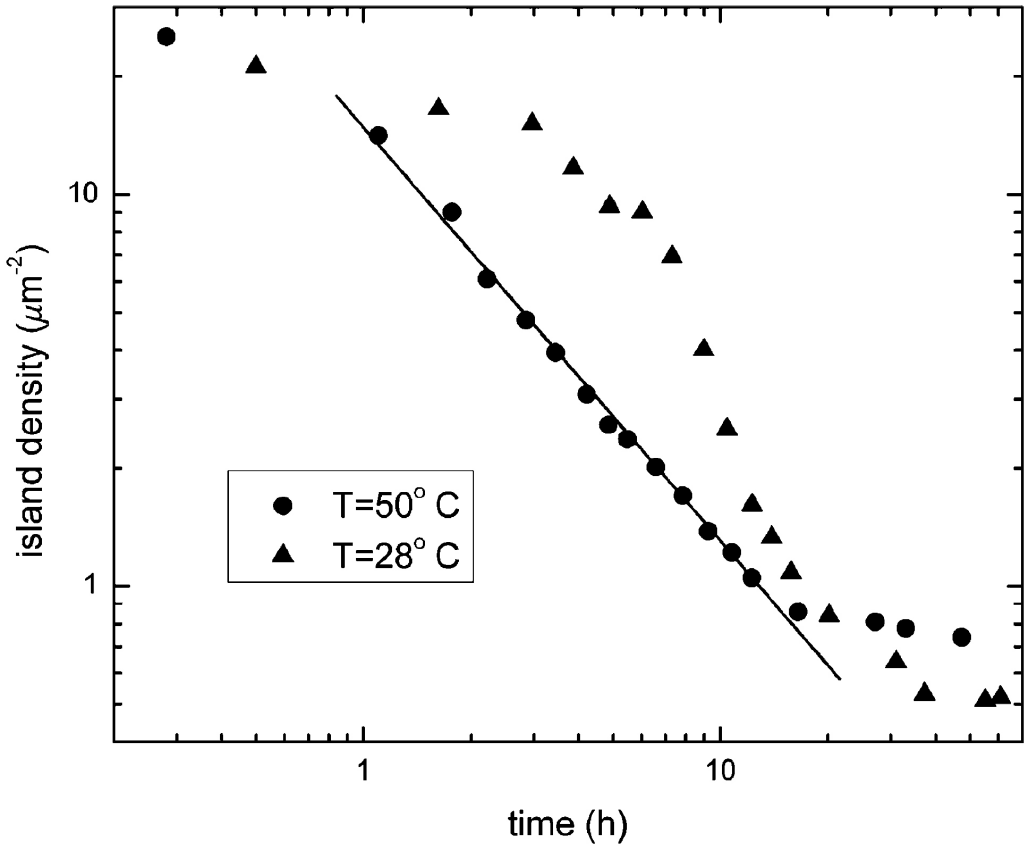


**Figure 8.2:** Island density as a function of time for samples maintained at 50°C (filled circles) and 28°C (filled triangles) shown on a log-log scale. The solid line is a least-square fit of the equation $\rho(t) \propto t^{-a}$ to the 50°C data, with $a = 1.05 \pm 0.02$.

solid solution grow if their radius exceeds a critical value that is determined by the average concentration of the solution and the concentration of the solution at the boundary of a grain. If the radius of the grain is below the critical value, the grain dissolves. Chakraverty applied this theory to clusters on surfaces [85, 88]. In the theory of island ripening, two regimes are discriminated, based on the mechanism that governs the exchange of molecules between the growing clusters and the supersaturated environment. If surface diffusion is a limiting process, then the theory predicts that the average island radius $\bar{R}$ increases with time as $\bar{R}(t) \propto t^{1/4}$. If the limiting process involves an energy barrier for detachment of molecules from the islands (interface transfer limited process), then the theory predicts $\bar{R}(t) \propto t^{1/3}$. This in turn yields a dependence of the island density of $\rho(t) \propto t^{-1}$, assuming a self-similarity of the islands and neglecting desorption from the surface. Our high-temperature data therefore support the hypothesis that the mass trans-

port is limited by the interface transfer mechanism before the island density eventually stabilizes.

Less clear is the case of the room-temperature data (filled triangles, Figure 8.2). We see that, initially, the island density remains relatively stable for a few hours after completion of evaporation. During this period, the high-temperature data already starts to exhibit a decrease in island density. Approximately 5 h after evaporation a rapid decrease in island density takes place, the steepest descent observed with $a = 2.87$. The decrease in island density is stabilized at approximately the same time as in the case of the high-temperature data. Such behavior is difficult to reconcile with any of the processes that are called for in the mean-field theory. In the following, we will show that at room temperature island ripening is likely a consequence of a series of processes in which surface defects play a dominant role.

We have already demonstrated [7, 8] that at room temperature steps on vicinal sapphire surfaces act as favorable sites for nucleation of rubrene molecules. In the present system, the substrates employed were as-received, polished sapphire substrates. The average roughness of the substrate surfaces was 0.22 nm with structural defects in the form of long trenches and depressions that can measure up to 1 nm in depth. The influence of these defects on the post-growth evolution of rubrene islands is exemplified in Figure 8.3, where we show a $12 \times 12$ $\mu$m$^2$ AFM scan of a sapphire surface onto which rubrene was evaporated. The image was obtained approximately 30 h after evaporation. Figure 8.3(a) shows the original AFM image of the surface where the island heights (measuring up to $\sim 100$ nm) are mapped into the full color range. Because surface defects are almost 2 orders of magnitude smaller than the maximum island height, they are not visible on the image. Figure 8.3(b) shows the same image obtained with an adaptive mapping algorithm. This algorithm is based on the inverse cumulative height distribution and allows us to image small height variations on relatively flat areas [113]. The mapping exposes defects in the form of straight or slightly curved lines running at various angles across the surface which are clearly seen in Figure 8.3(b). On the other hand, mapping also enhances the visibility of artifacts of the tapping mode imaging, which are seen as dark shadows to the right of many islands. These artifacts should not be confused with defects on the sapphire surface. Following a closer examination of Figure 8.3(b), we conclude that a vast majority of large islands are located at defects on the sapphire surface (e.g., the two most prominent lines which intersect in the lower-left corner of the image are decorated with large islands; also other islands can be found on defects which are seen as faint lines). This observation suggests that surface defects indeed influence the dynamics of the ripening process.

The mechanism responsible for ripening of rubrene islands at room tem-

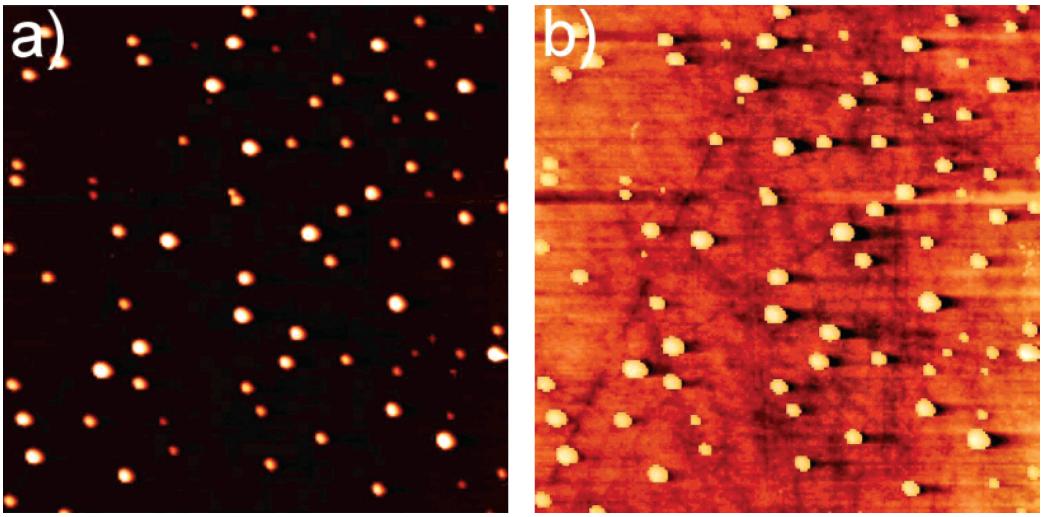


**Figure 8.3:** (a) $12 \times 12$ $\mu$m$^2$ AFM image of a thin rubrene film deposited onto an as-received sapphire substrate. The image was obtained $\sim 30$ h after evaporation. (b) The same image as in panel (a) after an adaptive mapping algorithm was employed. The algorithm, which is based on the inverse cumulative height distribution, exposes defects on the sapphire surface which can be seen as darker lines running at various angles across the surface. Dark "shadows"to the right of many islands are artifacts of the tapping mode AFM.

perature may therefore be as follows. Defects on the as-received substrates expose several planes of oxygen atoms of the sapphire single crystal. Such an environment may favor formation of bonds between the phenyl side groups of rubrene molecules and the oxygen atoms exposed at defects [7, 8]. Diffusing molecules are preferentially attached to these sites and islands that nucleated at defects are relatively stable. At longer observation times the majority of stable (larger) islands are observed at surface defects (Figure 8.3(b)). On the other hand, rubrene islands in defect-free regions are more prone to decomposition as a result of a weaker substrate-molecule interaction. As time progresses the majority of islands located at defects grow in size while a number of islands in defect-free regions undergoes decomposition. As the critical island radius increases with time [85, 88, 111] it eventually becomes larger than the typical radius of islands located in defect-free regions. This results in faster decomposition of these islands and leads to a rapid decrease in the island density observed at $t > 5$ h. The rapid decrease in the island density suggests that a number of islands in defect-free regions reach the critical size at similar times. At 50°C, the additional bonding of rubrene molecules to surface defects seems to be insufficient to alter the dynamics of island ripening. Since the difference between the high and low temperatures is relatively small, this possibly suggests the existence of an energy barrier

for confinement of molecules by surface defects.

The above interpretation would imply that the island size distribution undergoes different time evolution at 50°C and at room temperature. We expect that at room temperature, a rapid decrease in the island density observed at $t > 5$ h would result in a right-skewed distribution (the peak of the distribution shifted toward smaller radii), indicating a substantial fraction of islands that have nucleated at defect-free regions and are prone to decomposition. After the decrease in island density is terminated, the island size distribution should broaden. At elevated temperatures, where surface diffusion is not a limiting factor, the island size distribution is expected to maintain self-similarity in left-hand skewness throughout the observed ripening process [85]. We have analyzed the island size distributions throughout the ripening process and exemplify the histograms at similar time-frames for both substrate temperatures in Figure 8.4. The left column in Figure 8.4 shows histograms pertinent to the room temperature data, whereas the right column shows histograms which correspond to the data obtained at 50°C. By comparing the histograms column-wise, we see that, before and during the rapid decrease of the island density, the room temperature data exhibits a considerably narrower distribution than the 50°C data. In addition, the distribution function at room temperature evolves from a nearly symmetric (slightly left-skewed) to a right-skewed distribution at $t = 7.33$ h, displaying a peak at smaller radii. On the other hand, the distribution function at 50°C maintains its self-similarity throughout the ripening process. The evolution of the distribution function at room temperature therefore implies that at a given point in the ripening process a supply of molecules becomes available and a rapid growth of larger islands becomes possible. Such source of material may be represented by a number of unstable islands whose interaction with the substrate is relatively weak.

If we compare the behavior of rubrene with pentacene, where OR was not observed [97, 110], we can state several important differences. First, the growth mode of rubrene is of a Volmer-Weber type and the growth mode of pentacene is of a Frank-van der Merve type. This indicates that for pentacene the molecule-substrate interaction is stronger than the molecule-molecule interaction, while for rubrene the inverse is true. Surface mobility that is essential for the existence of OR is, therefore, lower for pentacene. Also the shape of the molecules is different: the pentacene molecule is planar and attaches to the surface with its longer axis almost vertical to the substrate. The rubrene molecule, instead is 3D, and is known to exhibit conformational changes upon transition from gas to solid phase. Such changes might improve the ability of the molecule to find energetically favorable sites at an existing island.

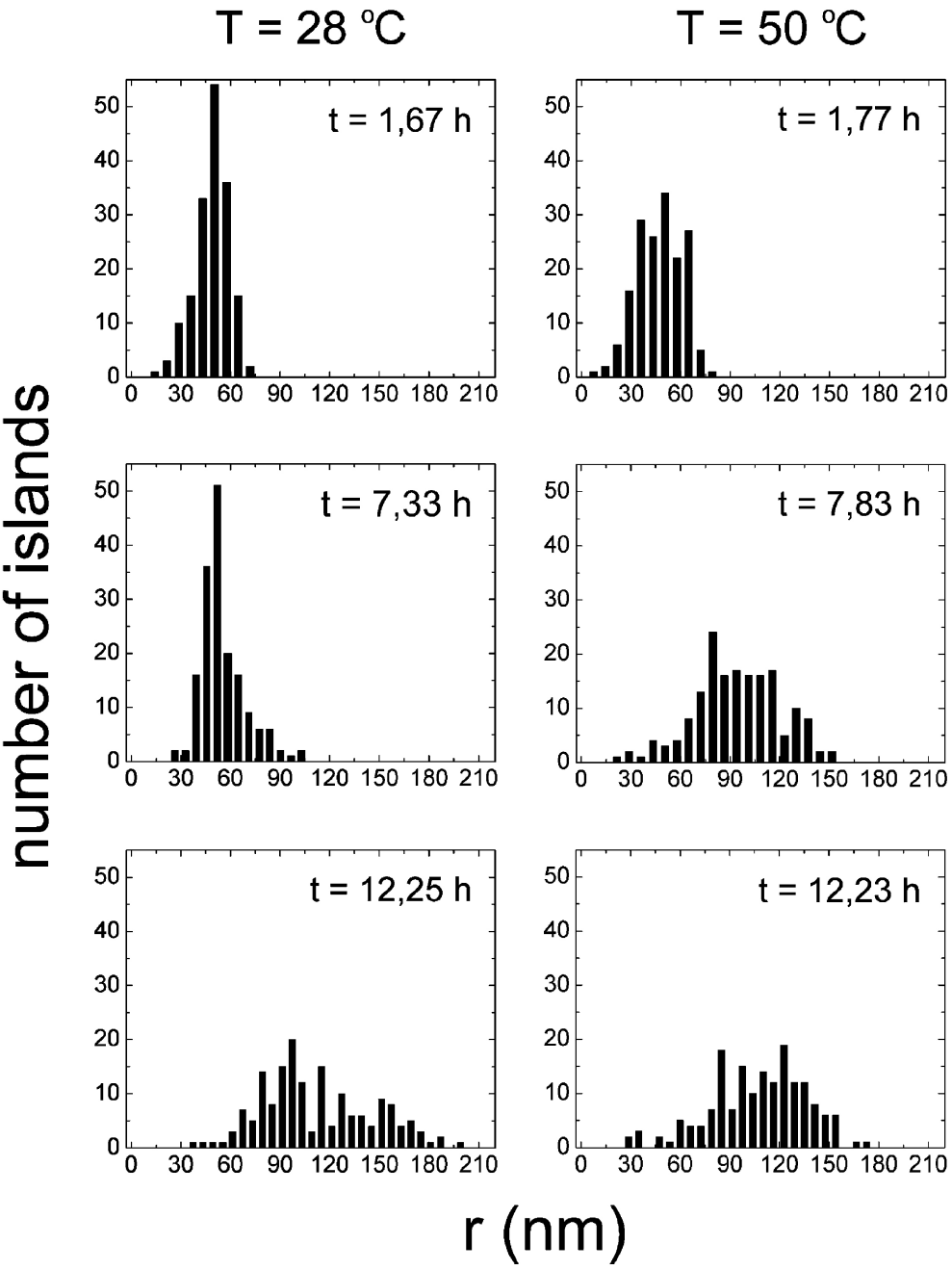


**Figure 8.4:** Histograms of island size distributions at similar time-frames for samples maintained at room temperature (left column) and at 50°C (right column).

## 8.4 Conclusion

In summary we have demonstrated that thin rubrene films grown on sapphire exhibit ripening observed so far in inorganic systems. The process is strongly temperature dependent. At 50°C, the process may be described by classical Ostwald ripening with the interface transfer as the limiting mechanism. At 28°C, ripening shows a behavior that is inconsistent with the predictions of the mean-field theory of Ostwald ripening. Ripening instead depends on the increased interaction of rubrene molecules with the substrate at defects and decomposition of the islands that nucleate at defect-free regions on the substrate surface.

## 8.5 Acknowledgments

We acknowledge helpful discussions with B. Žekš, D. Cvetko, and A. Franciosi.

# 9 Growth of ultrathin pentacene films on polymeric substrates

Growth of sub-monolayer and monolayer thick pentacene films on polystyrene, poly($\alpha$-methylstyrene), and poly(methyl methacrylate) was investigated using tapping-mode atomic force microscopy (AFM) and transverse shear microscopy (TSM). For comparison we also studied pentacene thin film growth on $SiO_2$. In the sub-monolayer regime pentacene nucleates in the form of 2D islands on hydrophilic surfaces, while on hydrophobic surfaces at higher temperatures a noticeable fraction of 3D island nucleation is also observed. By measuring the monolayer island nucleation densities and coverages as a function of substrate temperature we showed that there is a transition from the complete to the initially incomplete condensation regime at a temperature of $\approx 45°C$. We calculated the activation energies for surface diffusion of pentacene molecules on all substrates. TSM was used to map individual grains in smooth monolayer-thick polycrystalline pentacene films. The hydrophilicity of the substrate surface was correlated with the growth mode of pentacene. On hydrophobic surfaces 3D growth resulted in non-continuous pentacene films at temperatures above $\sim 50°C$, while on hydrophilic surfaces smooth pentacene films were obtained even at temperatures of $\approx 65°C$.

## 9.1 Introduction

Mechanical flexibility of organic semiconductor thin films is considered as one of the main practical advantages of using organic semiconductors as active layers in electronic devices such as organic thin film transistors (OTFTs). Pentacene, a member of the oligoacene family, stands out as one of the more attractive candidates for OTFTs applications on the account of its relatively high charge carrier mobility [22, 23] and its ability to form ordered polycrys-

talline films on a variety of substrates [26–30]. In order to fully exploit the mechanical flexibility of organic materials in OTFTs the active layer has to be deposited on a flexible surface such as a polymeric substrate. Despite the fact that the majority of pentacene thin film transistors are fabricated with $SiO_2$ as the gate dielectric, an increasing number of OTFT studies involve deposition of thin pentacene films on polymeric dielectrics [114–118].

Studies of charge carrier transport have shown [119, 120] that conduction in OTFTs involves one or at most two layers of the active organic material. It is therefore reasonable to expect that the performance of pentacene thin film transistors will strongly depend on the morphology of the starting layers. The morphology of ultrathin ($\sim$ 1 nm) polycrystalline pentacene films is characterized by grains with densities that depend on the substrate temperature and deposition rate. In order to gain a better understanding of the mechanism of charge carrier transport in ultrathin pentacene films a thorough investigation of their morphology as a function of deposition parameters is necessary. Up to date only a few (somewhat contradictory) morphological studies of ultrathin pentacene films on polymeric substrates have been reported [30, 121].

In the following work we present a detailed analysis of ultrathin pentacene film nucleation on three different polymeric dielectrics: polystyrene - PS, poly($\alpha$-methylstyrene) - P$\alpha$MS, and poly(methyl methacrylate) - PMMA. These three materials were chosen because it was possible to obtain surfaces with the same root-mean-square (RMS) roughness for all types of dielectrics. This is especially important since the substrate RMS roughness may substantially influence the surface nucleation densities of pentacene grains [121, 122]. Since these polymeric dielectrics are characterized either by a hydrophilic (PMMA) or a hydrophobic (PS, P$\alpha$MS) surface, it was possible to study the nucleation behavior of pentacene as a function of hydrophilicity of the substrate surface. For comparison, the nucleation of pentacene on $SiO_2$ was also investigated. The nucleation regime of pentacene on all types of substrates was unambiguously identified from plots of submonolayer nucleation densities and coverages as a function of deposition parameters. This allowed us to calculate the energy barriers for surface diffusion of pentacene molecules. The use of a relatively new scanning probe microscopy technique, called transverse shear microscopy (TSM), allowed us to image coalesced pentacene grains in $\sim$ 1 monolayer (ML) thick pentacene films. The analysis of TSM images showed that at suitable deposition conditions it is possible to grow smooth ML-thick polycrystalline pentacene films on all types of dielectric surfaces.

## 9.2 Experimental

Polymeric surfaces were prepared by spin coating $SiO_2$ substrates with 1 wt.% toluene solutions at 4000 RPM. The resulting polymer film thicknesses were approximately 40 nm in all cases. The substrates were then left to dry overnight. The RMS surface roughness of the substrates was measured with a Veeco CPII atomic force microscope (AFM) which was operated in tapping mode. The surface energies of the polymers were estimated by a technique proposed by Owens and Wendt. The method is based on contact-angle measurements of different liquids on the substrate and is described in detail in Refs. [123] and [124]. Deionized water, diiodomethane, glycerol, and ethylene glycol were used as characterization liquids.

Submonolayer thick ($\approx$ 0.4 nm) pentacene (Fluka, 99.8%) films were grown by thermal evaporation in a vacuum chamber with a base pressure of $\leq 10^{-7}$ Torr. For the temperature dependence measurements of pentacene island densities a temperature range from 10°C to 60°C was chosen. At temperatures near 70°C high desorption rates resulted in no pentacene molecules being adsorbed onto the polymeric surfaces. The temperature of the substrates was controlled with a heating/cooling block attached to the sample holder. During each deposition all four types (PS, P$\alpha$MS, PMMA, and $SiO_2$) of substrates were placed onto the sample holder simultaneously. Small samples (few $mm^2$) were used in order to avoid the angular dependence of the flux of pentacene molecules that strike the substrate surface. The morphology of submonolayer thick pentacene films was examined with a Veeco CPII AFM in tapping mode.

Monolayer thick pentacene films were grown by thermal evaporation under a base pressure of $\approx 10^{-6}$ Torr. The substrate temperature and deposition rate were fixed at 50°C or 65°C and $\approx$ 0.4 nm/min, respectively. TSM and topography images of pentacene films were acquired with a Veeco Nanoscope IIIA multimode AFM which was operated in an argon atmosphere. All TSM images were recorded with rectangular cantilevers (Mikromasch) with a typical force constant of $\approx 0.95$ N/m at a load of $\sim 10$ nN.

## 9.3 Results and discussion

All of the polymeric dielectrics used in our study exhibit a similar surface morphology with an RMS roughness of $2.8 \pm 0.1$ Å as determined from a series of $4 \times 4$ $\mu m^2$ AFM images. In the case of $SiO_2$ substrates the RMS roughness was $2.1 \pm 0.1$ Å .

Table 9.1 lists the surface energies and water contact angles for all four

types of substrates. The total surface energies of polymeric substrates are similar while there are differences between the dispersive and polar components for different polymers. PMMA has a larger polar component and a smaller dispersive component of the surface energy as compared to PS and P$\alpha$MS. Among all substrates $SiO_2$ has the highest surface energy.

| Substrate | Water contact angle (°) | Dispersive component of surface energy (mJ/m$^2$) | Polar component of surface energy (mJ/m$^2$) | Total surface energy (mJ/m$^2$) |
|---|---|---|---|---|
| PS | $90 \pm 2$ | $38.4 \pm 7.8$ | $0.6 \pm 1.3$ | $39.0 \pm 9.1$ |
| P$\alpha$MS | $91 \pm 2$ | $40.5 \pm 5.7$ | $0.4 \pm 0.6$ | $40.9 \pm 6.3$ |
| PMMA | $71 \pm 2$ | $28.9 \pm 8.5$ | $8.3 \pm 4.7$ | $37.3 \pm 13.2$ |
| $SiO_2$ | $37 \pm 2$ | $26.6 \pm 6.7$ | $30.9 \pm 7.5$ | $57.5 \pm 14.2$ |

**Table 9.1:** Surface properties of substrates. The uncertainties in the surface energies are a result of the fitting procedure (see, e.g. Ref. [124]).

For further discussion it will be useful to group the surfaces according to their water contact angle. We will refer to PS and P$\alpha$MS as hydrophobic surfaces and PMMA and $SiO_2$ as hydrophilic surfaces.

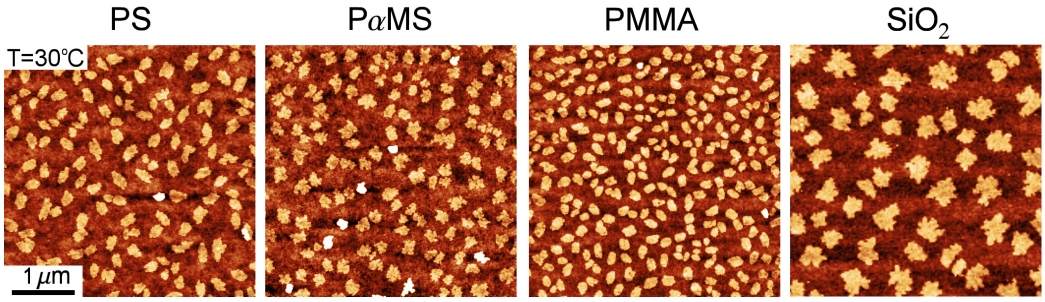


**Figure 9.1:** AFM height images of submonolayer thick ($\approx$ 0.4 nm) pentacene films on PS, P$\alpha$MS, PMMA, and $SiO_2$. The deposition rate was $\approx$ 0.4 nm/min in all cases.

Figure 9.1 shows $4 \times 4$ $\mu$m$^2$ AFM topography images of submonolayer thick pentacene films deposited on all four types of substrates. The deposition rate and substrate temperature were fixed at $\approx$ 0.4 nm/min and 30°C, respectively. In all cases the thin film morphology is characterized by two-dimensional (2D) islands that measure $\approx$ 1.5 nm in height. This is consistent with previous observations of pentacene monolayer island nucleation on inert substrates [8, 9, 30, 55]. The shape of the islands is more compact in the case of PS and PMMA compared to P$\alpha$MS and $SiO_2$. This is an indication that on PS and PMMA the diffusion of pentacene molecules that attach to

the island edges is higher in the case of these two substrates. This enables the molecules to find energetically more favorable sites at the island resulting in a compact island shape. Clearly the nucleation density is lowest in the case of $SiO_2$, followed by PS and P$\alpha$MS, with similar nucleation densities. The highest nucleation density of pentacene islands is observed on PMMA. On all polymeric substrates we note a small fraction of 3D pentacene islands (brighter islands in Figure 9.1). We will show that, on PMMA and $SiO_2$, these are likely a consequence of nucleation on defects, while on PS and P$\alpha$MS, at higher temperatures ($> 30$°C), 3D growth implies a weaker substrate-pentacene interaction on these two surfaces as compared to pentacene on PMMA and $SiO_2$.

We investigated the temperature dependence of the coverage of first and subsequent pentacene layers as well as the temperature dependence of the pentacene island density in the range from 10°C to 60°C at a fixed deposition rate of $\approx 0.4$ nm/min. Coverage of the first pentacene layer represents the pentacene island coverage, while coverage of subsequent layers is a measure of the degree of 3D island nucleation. The results are shown in Figure 9.2.

Concentrating on the temperature dependence of the first pentacene layer coverage (Figure 9.2(a)), we see that it is a slowly varying function of temperature in the range from 10°C to 45°C on all substrates. The coverage exhibits a rapid decrease at temperatures above 45°C. On all polymeric surfaces the coverage of the first pentacene layer decreases to zero at $\approx 70$°C (not shown in Figure 9.2(a)). Another interesting fact is that the coverage of the first pentacene layer is lower for hydrophobic surfaces compared to hydrophilic surfaces. This observation may be explained by noting that different chemical composition of the hydrophilic and hydrophobic surfaces may lead to a different density of available surface sites for adsorption of the incoming pentacene molecules.

If we now turn to the coverage of the second and subsequent pentacene layers we observe that hydrophilicity of the surface plays an important role. For the two hydrophilic (PMMA and $SiO_2$) surfaces the coverage of the second and subsequent pentacene layers is almost constant ($\approx 0$) in the whole temperature range. The coverage only slightly increases at temperatures below $\approx 20$°C. This implies that the small fraction of 3D islands that is present on hydrophilic surfaces is likely a consequence of pentacene nucleation on surface defects. In the case of the hydrophobic PS and P$\alpha$MS surfaces an increase (more pronounced on P$\alpha$MS) in the coverage of the second and subsequent pentacene layers with temperature is observed. This is a clear indication that on hydrophobic surfaces at higher temperatures (above $\approx 30$°C) a noticeable fraction of pentacene nucleates in 3D islands. The increase in the coverage of the second and subsequent pentacene layers also reduces the

coverage of the first pentacene layer.

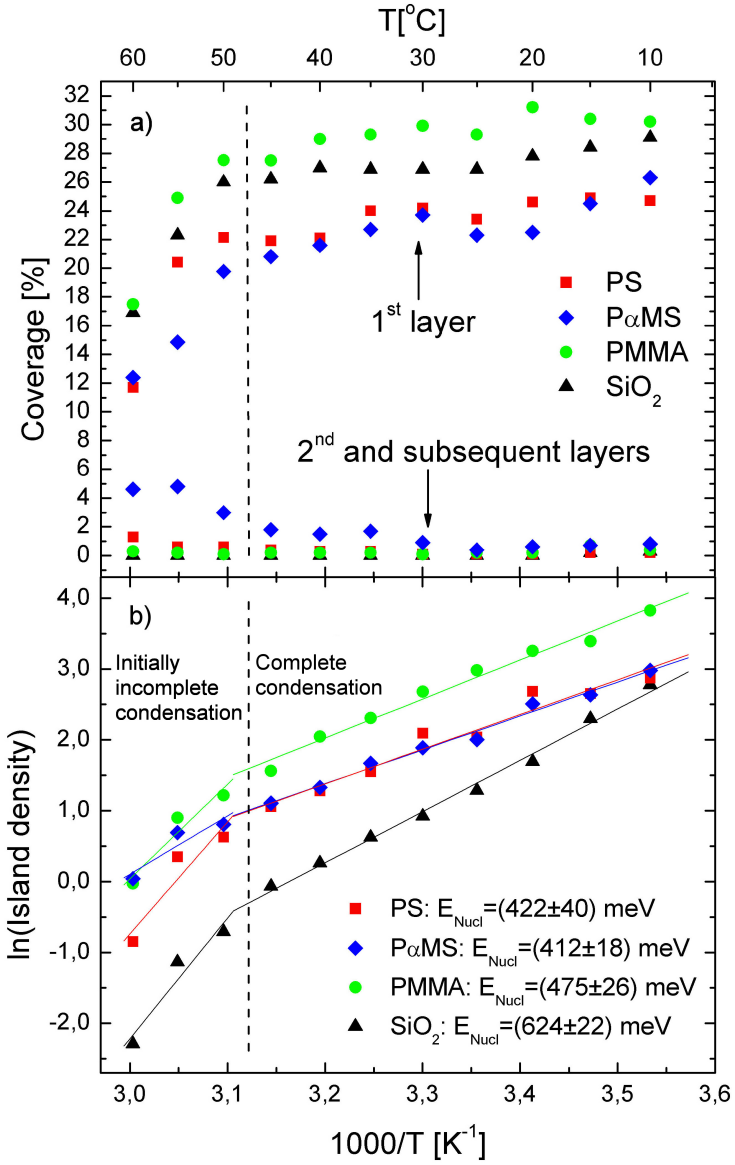


**Figure 9.2:** (a) Coverage of the first and subsequent layers of pentacene as a function of substrate temperature for PS, P$\alpha$MS, PMMA, and $SiO_2$. (b) Temperature dependence of the pentacene island density for all four types of substrates. Solid lines represent a fit of the equation $N \propto \exp(E_{Nucl}/k_B T_s)$ to the experimental data, where $N$ is the island density, $E_{Nucl}$ is the activation energy for nucleation and $T_S$ is the substrate temperature. The activation energies $E_{Nucl}$ in the complete condensation regime are calculated for all four substrates from the numerical fit in the temperature range from 10°C to 45°C. The vertical dashed line in both figures indicates a transition from complete to the initially incomplete condensation regime at a temperature between 45°C and 50°C.

As pointed out by Verlaak *et al.* [125], the growth mode (2D or 3D) of organic semiconductors on inert substrates heavily depends on the deposition parameters (deposition rate and substrate temperature). The thermodynamic driving force of the nucleation process is the (positive) difference $\Delta\mu$ between the chemical potential of the vapor phase $\mu_v$ and the chemical potential of an infinitely large organic crystal $\mu_c$ ($\Delta\mu = \mu_v - \mu_c$). In calculation of the energy released during molecular transfer from the vapor to the solid phase the finite size of the crystallites and the substrate-molecule interaction has to be taken into account. The parameter window for 3D nucleation strongly depends on the substrate-molecule interaction. At supersaturation ($\Delta\mu > 0$) and low substrate-molecule interactions, a transition from purely 2D to a combination of 3D and 2D growth is achieved by increasing the substrate temperature and/or by lowering the deposition rate. Further increase of the substrate temperature results in a purely 3D growth mode. The parameter window for 3D nucleation narrows with increasing substrate-molecule interaction. When the substrate-molecule interaction is larger or equal to the interaction of a single molecule with a neighboring molecular layer, only 2D growth is possible. Taking these considerations into account we conclude that the substrate-pentacene interaction is weaker on hydrophobic surfaces as compared to hydrophilic surfaces, since increasing the substrate temperature results in growth of 3D islands on the surface of PS and P$\alpha$MS. This is somewhat in variance with the surface energy data in Table 9.1. One would expect that the substrate-pentacene interaction would be stronger for P$\alpha$MS than for PMMA; however, it should be noted that the surface energies in Table 9.1 have rather large uncertainties. Another important fact is that the surface energy is obtained by measuring the contact angles of various liquids on the substrate surface. The contact angle of a liquid drop on a surface is a purely macroscopic quantity and does not tell us anything about the microscopic arrangement of molecules on the surface [126]. Thus the substrate-pentacene interaction strength is a more relevant parameter than the surface energy as emphasized by Verlaak *et al.* in Ref. [125]. Nevertheless a high surface energy of the $SiO_2$ substrate agrees with the above conclusions.

If we focus on the temperature dependence of the pentacene island density (Figure 9.2(b)), we see that on all substrates the island density decreases rapidly with increasing substrate temperature. In order to explain this behavior we will turn to the mathematical model of nucleation and growth of thin films, which has been developed by several authors (for a review of the theory see Ref. [54]). The model is based on kinetic rate equations, which take into account different processes that may occur on the substrate surface, such as: surface diffusion, re-evaporation from the substrate surface,

and island nucleation. Each of these processes is associated with an energy barrier (activation energy), e.g., formation of an island of a critical size $i$ (islands with $i+1$ molecules are stable) involves a binding energy $E_i$, which is defined as the difference in free energy between $i$ non-interacting molecules adsorbed on a surface and $i$ molecules that form an island. Based on the relative time scales of various processes occurring on the substrate surface, the rate equation formalism can be used to predict different regimes of condensation. In the so called "complete condensation" regime, re-evaporation from the substrate surface is neglected. After steady state conditions are reached (the density of single molecules on the substrate surface is constant with respect to time), the incoming molecules that strike the substrate surface diffuse on the substrate until they encounter a stable island. In the "initially incomplete" condensation regime, the islands also capture molecules by surface diffusion, although re-evaporation from the substrate surface cannot be neglected. Based on the rate equation formalism, a general equation can be written for the dependence of the saturated island density $N$ on the deposition rate $R$ and substrate temperature $T_S$:

$$N \propto R^{\delta} \exp(E_{Nucl}/k_B T_S), \tag{9.1}$$

In the above equation $k_B$ is the Boltzmann constant, $E_{Nucl}$ is the activation energy for homogeneous nucleation, which includes activation energies for various surface processes, and $\delta$ a critical exponent. The exact expressions for $E_{Nucl}$ and the value of the critical exponent $\delta$ depend on the condensation regime, critical cluster size, and dimensionality of the clusters (2D or 3D), which all need to be determined in order to extract relevant parameters from the experimental data. Based on the observations of pentacene monolayer island nucleation on polymeric and inorganic substrates Pratontep *et al.* concluded that the condensation regime of pentacene on PMMA and $SiO_2$ is initially incomplete [30]. On the other hand Stadlober *et al.* [121] argued that re-evaporation of molecules from the surface is balanced by diffusion of adsorbed molecules, leading them to conclude that on polymeric surfaces and also on $SiO_2$ the condensation regime is complete. Both Pratontep and Stadlober worked under similar deposition conditions.

Unlike previous studies our experimental data suggest that in the temperature range from 10°C to 60°C at a deposition rate of $\approx 0.4$ nm/min there is a transition from complete to the initially incomplete condensation regime. In Figure 9.2(b) we fitted Equation 9.1 to the temperature dependence of the pentacene island density $N$. This allowed us to extract the nucleation energies $E_{Nucl}$ for all four types of substrates. In the range from 10°C to 45°C the activation energies do not change with temperature which is an indication of a single condensation regime in this temperature range. The

activation energies for all substrates in this temperature range are listed in Figure 9.2(b). We can identify the condensation regime by noting that in this temperature range the island coverage (Figure 9.2(a)) does not change significantly with temperature. This is an indication that re-evaporation of pentacene molecules plays a minor role which is characteristic of the complete condensation regime. In this regime the activation energy for nucleation $E_{Nucl}$ has the following parameter dependencies in the case of 2D nucleation [54]:

$$E_{Nucl} = (E_i + iE_D)/(i+2), \tag{9.2}$$

where $E_D$ is the activation energy for diffusion. In order to calculate $E_D$ the critical cluster size $i$ and the binding energy $E_i$ have to be known. Ruiz *et al.* have independently determined that the critical cluster size in the case of pentacene on $SiO_2$ is 3 by a scaling analysis of the island size distributions [97]. A critical cluster size of 3 means that 4 pentacene molecules are necessary to form a stable island. A similar behavior in the case of complete condensation was observed by Stadlober *et al.* for pentacene on $SiO_2$ and polymeric substrates (PMMA, PVP, and PVCi) [121]. They found that the critical cluster size is $3 \leq i \leq 4$. In order to estimate the activation energies for diffusion we will assume, for the moment, that the critical cluster size is 3 for all substrate types. Kalihari *et al.* have shown that for $i = 3$ the cluster binding energy for pentacene is $\approx 892$ meV (see supplementary information in Ref. [60]). Using the above data we calculated the activation energy for diffusion of pentacene molecules on PS, P$\alpha$MS, PMMA, and $SiO_2$. The energies are listed in Table 9.2.

| Substrate | PS | P$\alpha$MS | PMMA | $SiO_2$ |
|---|---|---|---|---|
| $E_D$ [meV] | $406 \pm 67$ | $389 \pm 30$ | $494 \pm 44$ | $743 \pm 36$ |

**Table 9.2:** Activation energies for diffusion of pentacene molecules on PS, P$\alpha$MS, PMMA, and $SiO_2$.

In the complete condensation regime (2D case) the critical exponent $\delta = i/(i+2)$, which equals 0.6 in the case of $i = 3$. We determined the critical exponents for pentacene on PS, P$\alpha$MS, PMMA, and $SiO_2$ experimentally by measuring the deposition rate dependence of pentacene island density at a substrate temperature of 30°C. The results are shown in Figure 9.3. We calculated the critical exponents by fitting Equation 9.1 to the experimental data. The critical exponents are in the range from 0.67 to 0.80 which is in reasonable agreement with the theoretical prediction of 0.6 for $i = 3$.

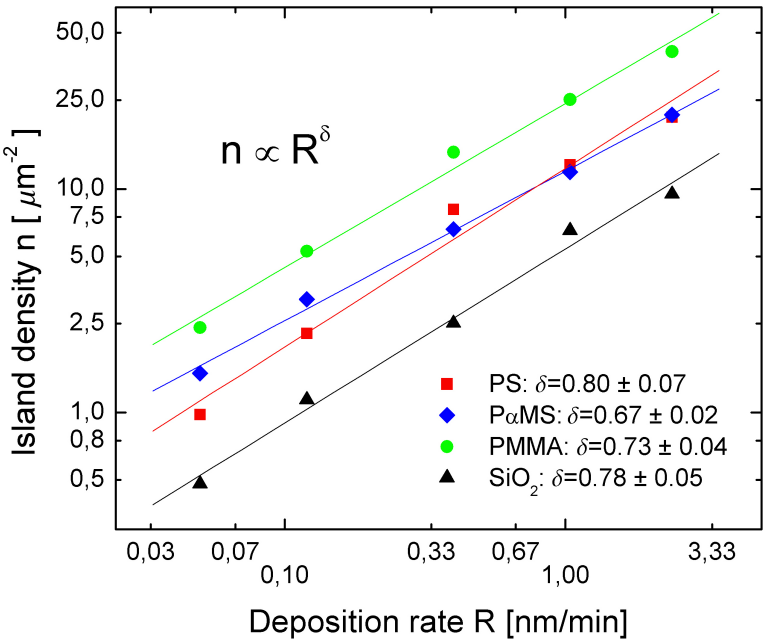


**Figure 9.3:** Pentacene island density as a function of deposition rate for PS, P$\alpha$MS, PMMA, and $SiO_2$. The substrates were held at 30°C.

In Figure 9.2(b) we observe a change in the activation energies $E_{Nucl}$ on all substrates when the temperature is increased above 45°C. This implies also a change in the condensation regime. From Figure 9.2(a) it is evident that the pentacene island coverage rapidly decreases when the temperature is raised above 45°C, which is an indication of pentacene re-evaporation from the substrate surface. This implies that the condensation regime changes from complete condensation at lower temperatures, to the initially incomplete condensation at higher temperatures, where re-evaporation of pentacene plays an important role. From Figure 9.2(b) we can obtain only a crude estimate of the activation energies $E_{Nucl}$ in the range from 45°C to 60°C since the data contains only three points (at temperatures around 70°C the island coverage decreases to $\approx 0$). The activation energies are $\sim$ 1360 meV, $\sim$ 710 meV, $\sim$ 1150 meV, and $\sim$ 1470 meV for PS, P$\alpha$MS, PMMA, and $SiO_2$, respectively. In the initially incomplete condensation regime the activation energy for nucleation $E_{Nucl}$ has the following parameter dependencies in the case of 2D nucleation [54]:

$$E_{Nucl} = (E_i + iE_A)/2, \tag{9.3}$$

where $E_A$ is the activation energy for desorption. The above data can be used to estimate $E_A$ using Equation 9.3 and assuming a critical cluster size of 3. The activation energies for desorption $E_A$ are $\sim$ 610 meV, $\sim$ 180 meV, $\sim$ 470

meV, and $\sim$ 680 meV for PS, P$\alpha$MS, PMMA, and $SiO_2$, respectively. We must keep in mind that these are only rough estimates since a small number of data points was used in the numerical fit. Nevertheless, the smallest $E_A$ for P$\alpha$MS implies a weaker substrate-pentacene interaction as compared to pentacene on other substrates. This is clearly consistent with the observation of a noticeable fraction of 3D pentacene islands that nucleate on P$\alpha$MS at higher temperatures.

Both plots in Figure 9.2 provide some information on the mean diffusion distance $X_S$ of pentacene molecules on the substrate surface before desorption. In the complete condensation regime (below $\approx$ 45°C) re-evaporation from the substrate surface is negligible. This suggests that diffusing pentacene molecules attach to stable islands before being desorbed, which implies that $X_S$ is larger than the typical distance between pentacene islands. As the temperature increases the typical distance between pentacene islands also increases (the pentacene island density decreases). Above $\approx$ 45°C the condensation regime changes to the initially incomplete condensation. In this regime the diffusing molecules my desorb before reaching a stable island. This suggests that with increasing temperature $X_S$ eventually becomes comparable to or smaller than the typical distance between pentacene islands.

Controlling the pentacene island density on the substrate surface is important from the technological point of view since grain boundaries may influence charge carrier transport through organic films [127]. We have seen that the pentacene island density can be controlled by varying the substrate temperature and deposition rate. In the case of polymeric substrates the pentacene island density is higher on hydrophilic PMMA as compared to hydrophobic PS and P$\alpha$MS. This is probably a result of a higher activation energy for diffusion of pentacene molecules on PMMA compared to PS and P$\alpha$MS and a different chemical composition of hydrophilic and hydrophobic surfaces, which may result in a different density of available surface sites for attachment of the incoming pentacene molecules. The substrate surface roughness may also play an important role in determining the nucleation density. The lowest surface roughness of $SiO_2$ substrates may be the reason for the lowest pentacene nucleation density among all types of surfaces.

Increasing the thickness of the deposited material results in coalescence of 2D pentacene islands. We were able to obtain smooth monolayer thick ($\sim$ 1.5 nm) pentacene films on hydrophilic and hydrophobic surfaces at temperatures as high as 50°C at a deposition rate of $\approx$ 0.4 nm/min. The films were examined by a novel contact AFM technique called transverse shear microscopy. TSM is similar to conventional lateral force microscopy which is used to obtain frictional maps of the surface, except that in TSM the torsional bending of the cantilever is recorded while scanning the tip in the

direction parallel to the long cantilever axis [60–62]. TSM is sensitive to grain orientation and can be used to map individual crystalline grains in thin organic semiconductor films.

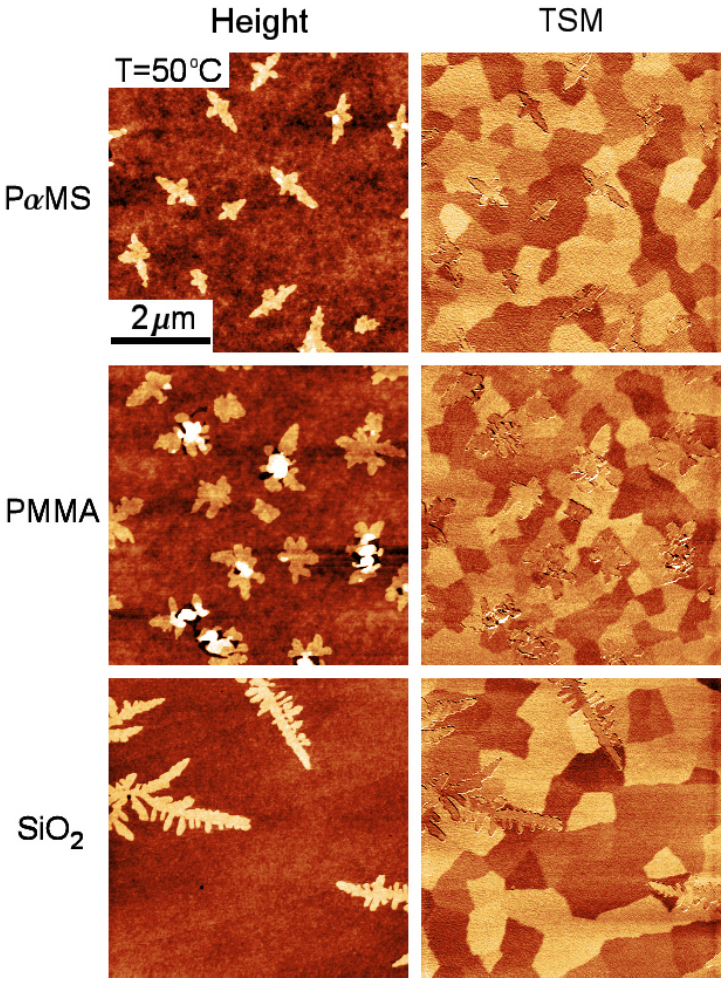


**Figure 9.4:** AFM topography (left column) and TSM (right column) images of pentacene films with a nominal thickness of 2 nm deposited on P$\alpha$MS, PMMA, and $SiO_2$ at a substrate temperature of 50°C and a deposition rate of $\approx 0.4$ nm/min.

Figure 9.4 shows AFM height (left column) and TSM (right column) images of monolayer thick pentacene films deposited on various substrates. The topography images are featureless except for a small number of pentacene islands that have nucleated on top of the first pentacene monolayer. On the other hand TSM images reveal individual faceted grains of the first pentacene monolayer. The images were obtained by subtracting the forward (trace) and reverse (retrace) TSM signals. The contrast in TSM images directly

corresponds to pentacene grain orientation [60, 62]. In the case of pentacene on inert substrates the **ab** crystallographic plane of the grains is parallel to the substrate surface [125]. When the scan direction is aligned along the [110] crystallographic axis the trace TSM signal is maximized while the retrace TSM signal is minimized. If the the scan direction is aligned along the $[1\bar{1}0]$ the trace TSM signal is minimized while the retrace TSM signal is maximized. This means that the [110] ($[1\bar{1}0]$) direction of the brightest (darkest) grains in Figure 9.4 is aligned along the scan (horizontal) direction. Intermediate contrast of grains corresponds to alignment of the scan direction between the [110] and $[1\bar{1}0]$ crystallographic directions.

TSM images show the largest grain sizes on $SiO_2$, followed by P$\alpha$MS, and PMMA. This is in agreement with Figure 9.1, where the lowest nucleation density of monolayer islands was observed on $SiO_2$, followed by P$\alpha$MS, and PMMA.

We also investigated the influence of surface hydrophilicity on the growth mode of ML-thick thick pentacene films on polymeric substrates. Figure 9.5 shows the morphology of nominally 2 nm thick pentacene films deposited on hydrophobic P$\alpha$MS and hydrophilic PMMA at a substrate temperature of 65°C. While at 50°C continuous film growth is still possible even on hydrophobic surfaces, at higher temperatures 3D growth on P$\alpha$MS results in a non-continuous pentacene film. On the other hand relatively smooth films can still be grown on PMMA at 65°C. As discussed above this is a consequence of a weaker substrate-pentacene interaction in the case of P$\alpha$MS as compared to PMMA. In the case of hydrophobic surfaces increasing the substrate temperature reduces the nucleation density and thereby the density of grain boundaries in monolayer thick pentacene films only up to a certain temperature. Above this temperature ($> 50$°C in the case of P$\alpha$MS) a transition from 2D to 3D growth occurs. This results in ill-connected grains and has a detrimental effect on the charge carrier transport.

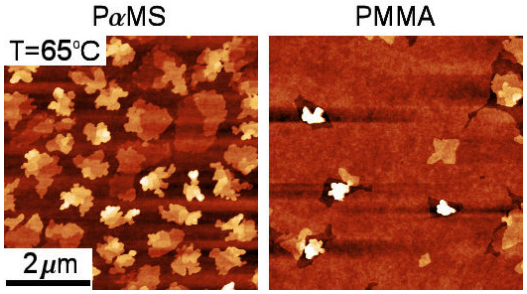


**Figure 9.5:** Contact-mode AFM images of pentacene films with a nominal thickness of 2 nm deposited on P$\alpha$MS (left) and PMMA (right) at a substrate temperature of 65°C and a deposition rate of $\approx 0.4$ nm/min.

## 9.4 Conclusions

We carried out a detailed analysis of ultrathin pentacene film growth on polymeric surfaces. For comparison pentacene thin film nucleation was also studied on $SiO_2$. By measuring the monolayer-island nucleation densities and island coverage as a function of substrate temperature we showed that a transition from the complete to the initially incomplete condensation regime occurs at a temperature of $\approx 45°C$. We were able to extract the activation energies for surface diffusion of pentacene molecules on all substrates. Analysis of the first and subsequent pentacene layer coverage as a function of temperature showed that on hydrophobic surfaces at substrate temperatures above $\approx 30°C$ a noticeable fraction of pentacene nucleates in the form of 3D islands.

At suitable conditions we were able to grow smooth ML-thick pentacene films on all types of dielectric surfaces. TSM was used to image individual crystalline grains in these polycrystalline pentacene films. The growth mode of ML-thick pentacene films was correlated with the hydrophilicity of the substrate surface. In the case of hydrophobic P$\alpha$MS surface a transition from 2D to 3D growth was observed at higher temperatures ($> 50°C$), while on hydrophilic surfaces 2D growth persisted even at temperatures around 65°C. 3D growth of pentacene on hydrophobic P$\alpha$MS was ascribed to a weaker substrate-pentacene interaction as compared to the interaction of pentacene molecules with hydrophilic surfaces. We showed that the growth mode of pentacene is closely related to the substrate surface hydrophilicity i.e. the water contact angle on the surface, which is an easily measurable quantity.

# 10 Conclusions

The first part of the work focused on the influence of substrate surface features on growth of ultrathin organic semiconductor films. We chose sapphire single crystal as the substrate material, since its vicinal (0001) surface, characterized by a terrace-and-step morphology, represents a viable option for templated growth.

In order to obtain a suitable surface for organic thin-film growth the substrates were annealed at high temperatures. Our results on the evolution of the (0001) $\alpha$-$Al_2O_3$ surface upon high-temperature annealing show that the surface morphology strongly depends on the annealing protocol. Annealing the surface initially covered with 0.21 nm high steps at 1200°C results in localized step coalescence that evolves into a terrace-and-step with island morphology. After prolonged annealing the islands become incorporated into the terraces. On the other hand annealing at higher temperatures (1500°C) leads to step coalescence on a global scale, and results in a terrace-and-step morphology with an indication of step bunching after longer annealing times. The step height and terrace width on the sapphire surface increase with increasing annealing temperature. The substrates that were used in our thin-film growth studies were annealed at 1500°C for periods up to 120 h in order to obtain large, well-defined terraces separated by nanometer-size steps, which would potentially act as nucleation sites for organic molecules.

Our preliminary growth studies were performed with the organic semiconductor rubrene. We deposited thin rubrene films on annealed vicinal (0001) sapphire surfaces by thermal evaporation. Atomic force microscopy studies showed that the vicinal surface acts as a template for growth of wire-like rubrene structures with sub-micron lateral dimensions along the sapphire steps. We also demonstrated that substrate features, such as nanometer-size islands induced by the annealing procedure, also act as nucleation sites for rubrene molecules. The increased probability for molecules to attach to surface steps was ascribed to three-dimensional geometry of the rubrene molecule.

Our growth studies were extended to include other organic molecules. We performed investigations of pentacene, PTCDA, and TPD growth on vicinal sapphire surfaces. Our results confirmed that the morphology of ultrathin organic films heavily depends on the conformation of the organic molecule. In the case of planar molecules, which nucleate in the form of two-dimensional (pentacene) or three-dimensional (PTCDA) islands, the surface steps on sapphire influence the positions of these islands. At suitable substrate temperature (room temperature in the case of pentacene and 135°C in the case of PTCDA) the majority of islands nucleates at the nm-size steps. If the nominal thickness of the organic material is increased the average island size also increases. In the case of pentacene the two-dimensional islands eventually coalesce and form a complete monolayer. Steps on the sapphire surface have a more profound effect on the morphology of the organic film in the case of non-planar molecules. Rubrene and TPD both nucleate in the form of three-dimensional islands. While TPD islands immediately assume positions at the sapphire steps, rubrene islands also nucleate on terraces. However; these islands are unstable and eventually decay while their material is incorporated into islands located at the steps. This process may take several hours after the deposition of the material has stopped. Increasing the amount of deposited TPD or rubrene results in growth of linear-structures that follow the step direction. These linear structures are unstable and eventually decay into three-dimensional islands with their centers at the sapphire steps. We found that ripening is responsible for the morphological time evolution of TPD and rubrene thin films. The faster ripening rate of TPD was associated to the wealth of rotational degrees of freedom in TPD molecules as opposed to only a twisting degree of the tetracene backbone in rubrene.

Further investigations were carried out to identify the mechanism behind the morphological time evolution of thin rubrene films. In order to reduce the influence of nm-size steps on the nucleation of rubrene as-received polished sapphire surfaces were used. We studied the morphological evolution of rubrene islands after deposition of the organic material has stopped. Our results showed that the density of rubrene islands decreases with time while the average island size increases. The process of island ripening is strongly temperature dependent. At 50°C, the process may be described by classical Ostwald ripening. In this case the limiting mechanism of the ripening process is detachment of molecules from the surface of the islands. At room temperature, the results showed that defects on the sapphire surface play a dominant role in the process of rubrene island ripening.

We demonstrated that the ability of the substrate surface to act as a template for organic thin film growth depends on the type of the organic molecule. Future studies should focus on finding suitable organic molecules

with the potential to form stable organic patterns on insulating surfaces. Electrical characterization of these structures could then be carried out using conductive atomic force microscopy. An alternative method, which is becoming very popular, is functionalization of the organic molecules. Since molecules are extended objects attaching specific groups e.g. to each end of a planar organic molecule may lead to growth of low-dimensional patterns on the substrate surface. On the other hand, electronic transport through these organic structures would in principle be altered by functionalization, which may present a disadvantage of this technique.

In order to take full advantage of mechanical flexibility of thin organic semiconductor films, these have to be deposited on plastic substrates. The second part of the work therefore focused on growth of ultrathin pentacene films on polymeric substrates. We studied the growth of sub-monolayer and monolayer thick films of pentacene on polystyrene, poly($\alpha$-methylstyrene), and poly(methyl methacrylate). The results were also compared with pentacene growth on $SiO_2$. We found that, in the sub-monolayer regime, pentacene nucleates in the form of two-dimensional islands on hydrophilic surfaces ( poly(methyl methacrylate), $SiO_2$ ), while on hydrophobic surfaces ( polystyrene, poly($\alpha$-methylstyrene) ) at higher temperatures (above $\approx 30°C$), a noticeable fraction of three-dimensional island nucleation is also observed. Our results showed a transition from the complete to the initially incomplete condensation regime at temperatures above $\approx 45°C$. We calculated the activation energies for surface diffusion of pentacene molecules from plots of island densities vs. temperature on all types of surfaces. Transverse shear microscopy images revealed that, at suitable deposition conditions, it is possible to grow smooth monolayer-thick polycrystalline pentacene films on all substrates. The hydrophilicity of the substrate surface was correlated with the growth mode of pentacene. We observed three-dimensional growth of pentacene on hydrophobic surfaces at temperatures above $\sim 50°C$, which resulted in non-continuous films. On the other hand, deposition of pentacene on hydrophilic surfaces yielded smooth films even at temperatures of $\approx 65°C$.

# Bibliography


[1] E. H. C. Parker, ed., *The Technology and Physics of Molecular Beam Epitaxy* (Plenum, New York, 1985).

[2] M. A. Herman and H. Sitter, *Molecular Beam Epitaxy: Fundamentals and Current Status* (Springer-Verlag, Berlin Heidelberg, 1996), 2nd ed.

[3] S. R. Forrest, Chem. Rev. **97**, 1793 (1997).

[4] T. Ito and S. Okazaki, Nature **406**, 1027 (2000).

[5] J. V. Barth, G. Costantini, and K. Kern, Nature **437**, 671 (2005).

[6] P. R. Ribič and G. Bratina, Surf. Sci. **601**, 44 (2007).

[7] P. R. Ribič and G. Bratina, Surf. Sci. **601**, L25 (2007).

[8] P. R. Ribič and G. Bratina, J. Vac. Sci. Technol. B **25**, 1152 (2007).

[9] P. R. Ribič and G. Bratina, Surf. Sci. **602**, 1368 (2008).

[10] P. R. Ribič and G. Bratina, J. Phys. Chem. C **111**, 18558 (2007).

[11] A. J. Lovinger, S. R. Forrest, M. L. Kaplan, P. H. Schmidt, and T. Venkatesan, J. Appl. Phys. **55**, 476 (1984).

[12] S. R. Forrest, M. L. Kaplan, and P. H. Schmidt, J. Appl. Phys. **56**, 543 (1984).

[13] K. Glöckler, C. Seidel, A. Soukopp, M. Sokolowski, E. Umbach, M. Böhringer, R. Berndt, and W.-D. Schneider, Surf. Sci. **405**, 1 (1998).

[14] B. Krause, A. C. Dürr, K. A. Ritley, F. Schreiber, H. Dosch, and D. Smilgies, Appl. Surf. Sci. **175-176**, 332 (2001).

[15] A. Das, G. Salvan, T. U. Kampen, W. Hoyer, and D. R. T. Zahn, Appl. Surf. Sci. **212-213**, 433 (2003).

[16] J. B. Gustafsson, E. Moons, S. M. Widstrand, and L. S. O. Johansson, Surf. Sci. **572**, 23 (2004).

[17] L. Kilian, E. Umbach, and M. Sokolowski, Surf. Sci. **573**, 359 (2004).

[18] S. Kera, H. Setoyama, M. Onoue, K. K. Okudaira, Y. Harada, and N. Ueno, Phys. Rev. B **63**, 115204 (2001).

[19] M. Möbus, N. Karl, and T. Kobayashi, J. Cryst. Growth **116**, 495 (1992).

[20] S. R. Forrest, M. L. Kaplan, and P. H. Schmidt, J. Appl. Phys. **55**, 1492 (1984).

[21] T. Ogawa, K. Kuwamoto, S. Isoda, T. Kobayashi, and N. Karl, Acta Cryst. B **55**, 123 (1999).

[22] H. Klauk, M. Halik, U. Zschieschang, G. Schmid, W. Radlik, and W. Weber, J. Appl. Phys. **92**, 5259 (2002).

[23] D. Knipp, R. A. Street, A. Völkel, and J. Ho, J. Appl. Phys. **93**, 347 (2003).

[24] R. G. Endres, C. Y. Fong, L. H. Yang, G. Witte, and C. Wöll, Comp. Mat. Sci. **29**, 362 (2004).

[25] E. A. Silinsh, V. A. Kolesnikov, I. J. Muzikante, and D. R. Balode, Phys. Status Solidi (B) **113**, 379 (1982).

[26] J. H. Kang and X.-Y. Zhu, Appl. Phys. Lett. **82**, 3248 (2003).

[27] L. Floreano, A. Cossaro, D. Cvetko, G. Bavdek, and A. Morgante, J. Phys. Chem. B **110**, 4908 (2006).

[28] W. J. Huang, B. Q. Li, and J. M. Zuo, Surf. Sci. **595**, 157 (2005).

[29] H. Yanagisawa, T. Tamaki, M. Nakamura, and K. Kudo, Thin Solid Films **464-465**, 398 (2004).

[30] S. Pratontep, F. Nüesch, L. Zuppiroli, and M. Brinkmann, Phys. Rev. B **72**, 085211 (2005).

[31] R. B. Campbell, J. M. Robertson, and J. Trotter, Acta Crystallogr. **14**, 705 (1961).

[32] C. C. Mattheus, A. B. Dros, J. Baas, A. Meetsma, J. L. de Boer, and T. T. M. Palstra, Acta Crystallogr., Sect. C: Cryst. Struct. Commun. **C57**, 939 (2001).

[33] K. Hummer and C. Ambrosch-Draxl, Phys. Rev. B **72**, 205205 (2005).

[34] V. C. Sundar, J. Zaumseil, V. Podzorov, E. Menard, R. L. Willett, T. Someya, M. E. Gershenson, and J. A. Rogers, Science **303**, 1644 (2004).

[35] R. W. I. de Boer, M. E. Gershenson, A. F. Morpurgo, and V. Podzorov, Phys. Status Solidi (A) **201**, 1302 (2004).

[36] D. Käfer, L. Ruppel, G. Witte, and C. Wöll, Phys. Rev. Lett. **95**, 166602 (2005).

[37] S. Kowarik, A. Gerlach, S. Sellner, F. Schreiber, J. Pflaum, L. Cavalcanti, and O. Konovalov, Phys. Chem. Chem. Phys. **8**, 1834 (2006).

[38] M. Haemori, J. Yamaguchi, S. Yaginuma, K. Itaka, and H. Koinuma, Jpn. J. Appl. Phys., Part 1 **44**, 3740 (2005).

[39] D. Käfer and G. Witte, Phys. Chem. Chem. Phys. **7**, 2850 (2005).

[40] D. A. D. S. Filho, E.-G. Kim, and J.-L. Brédas, Adv. Mater. **17**, 1072 (2005).

[41] D. E. Henn, W. G. Williams, and D. J. Gibbons, J. Appl. Crystallogr. **4**, 256 (1971).

[42] P. M. Borsenberger and D. S. Weiss, *Organic Photoreceptors for Xerography* (Marcel Dekker, New York, 1998).

[43] M. Strukelj, R. H. Jordan, and A. Dodabalapur, J. Am. Chem. Soc. **118**, 1213 (1996).

[44] J. K. nad P. Di Marco, M. Cocchi, V. Fattori, N. Camaioni, and J. Duff, Appl. Phys. Lett. **68**, 2317 (1996).

[45] C. Qiu, H. Chen, M. Wong, and H. S. Kwok, Synth. Met. **140**, 101 (2004).

[46] V. Bulovic, G. Gu, P. E. Burrows, S. R. Forrest, and M. E. Thompson, Nature **380**, 29 (1996).

[47] M. Knupfer, J. Fink, E. Zojer, G. Leising, and J. L. Bredas, Phys. Rev. B **61**, 1662 (2000).

[48] M. Malagoli and J. L. Brédas, Chem . Phys. Lett. **327**, 13 (2000).

[49] A. R. Kennedy, W. E. Smith, D. R. Tackley, W. I. F. David, K. Shankland, B. Brown, and S. J. Teat, J. Mater. Chem. **12**, 168 (2002).

[50] L. I. Maissel and R. Glang, eds., *Handbook of Thin Film Technology* (McGraw-Hill, New York, 1970).

[51] S. Dushmann, *Scientific Foundations of Vacuum Technique* (Wiley, New York, 1962).

[52] L. B. Loeb, *The Kinetic Theory of Gases* (McGraw-Hill, New York, 1934), 2nd ed.

[53] G. F. Weston, *Ultrahigh Vacuum Practice* (Butterworths, London, 1985).

[54] J. A. Venables, G. D. T. Spiller, and M. Hanbücken, Rep. Prog. Phys. **47**, 399 (1984).

[55] S. Pratontep, M. Brinkmann, F. Nüesch, and L. Zuppiroli, Phys. Rev. B **69**, 165201 (2004).

[56] E. Meyer, H. J. Hug, and R. Bennewitz, *Scanning Probe Microscopy: The Lab on a Tip* (Springer-Verlag, Berlin Heidelberg, 2004).

[57] D. Rugar, H. J. Mamin, and P. Guethner, Appl. Phys. Lett. **55**, 2588 (1989).

[58] I. Singer and H. Pollock, eds., *Fundamentals of Friction: Macroscopic and Microscopic Processes, NATO-ASI E, Vol. 220* (Kluwer Academic, Dordrecht, The Netherlands, 1992), p. 427.

[59] M. Tortonese, R. C. Barrett, and C. F. Quate, Appl. Phys. Lett. **62**, 834 (1993).

[60] V. Kalihari, E. B. Tadmor, G. Haugstad, and C. D. Frisbie, Adv. Mater. **20**, 1 (2008).

[61] J. A. Last and M. D. Ward, Adv. Mater. **8**, 730 (1996).

[62] K. Puntambekar, J. Dong, G. Haugstad, and C. D. Frisbie, Adv. Funct. Mater. **16**, 879 (2006).

[63] S. Morita, R. Wiesendanger, and E. Meyer, eds., *Noncontact Atomic Force Microscopy* (Springer-Verlag, Berling, 2002).

[64] M. Yoshimoto, T. Maeda, T. Ohnishi, H. Koinuma, O. Ishiyama, M. Shinohara, M. Kubo, R. Miura, and A. Miyamoto, Appl. Phys. Lett. **67**, 2615 (1995).

[65] J. O. Ossó, F. Schreiber, V. Kruppa, H. Dosch, M. Garriga, M. I. Alonso, and F. Cerdeira, Adv. Funct. Mater. **12**, 455 (2002).

[66] E. Barrena, J. O. Ossó, F. Schreiber, M. Garriga, M. I. Alonso, and H. Dosch, J. Mater. Res. **19**, 2061 (2004).

[67] R. W. G. Wyckoff, *Crystal Structures II* (Wiley, New York, 1964).

[68] J. R. Heffelfinger, M. W. Bench, and C. B. Carter, Surf. Sci. **343**, L1161 (1995).

[69] J. R. Heffelfinger and C. B. Carter, Surf. Sci. **389**, 188 (1997).

[70] J. R. Heffelfinger, M. W. Bench, and C. B. Carter, Surf. Sci. **370**, L168 (1997).

[71] L. Pham Van, O. Kurnosikov, and J. Cousty, Surf. Sci. **411**, 263 (1998).

[72] G. M. Whitesides, J. P. Mathias, and C. T. Seto, Science **254**, 1312 (1991).

[73] K. Kuhnke and K. Kern, J. Phys.: Condens. Matter **15**, S3311 (2003).

[74] T. Kato, T. Takeuchi, Y. Inoue, S. Hasegawa, K. Inoue, and H. Nakashima, Appl. Phys. Lett. **72**, 465 (1998).

[75] A. Ismach, L. Segev, E. Wachtel, and E. Joselevich, Angew. Chem. Int. Ed. **43**, 6140 (2004).

[76] K. Itaka, M. Yamashiro, J. Yamaguchi, S. Yaginuma, M. Haemori, and H. Koinuma, Appl. Surf. Sci. **252**, 2562 (2006).

[77] S. Yaginuma, J. Yamaguchi, K. Itaka, and H. Koinuma, Thin Solid Films **486**, 218 (2005).

[78] Y. H. Cha, Y. W. Lee, K.-H. Ko, E. C. Jung, G. Lim, J. Kim, T.-S. Kim, and D.-Y. Jeong, Appl. Opt. **44**, 7810 (2005).

[79] P. E. Dyer, S. R. Jackson, P. H. Key, W. J. Metheringham, and M. J. J. Schmidt, Appl. Surf. Sci. **96-98**, 849 (1996).

[80] F. Poser, A. Bhattacharya, S. Weeke, and W. Richter, J. Cryst. Growth **248**, 317 (2003).

[81] C. D. Dimitrakopoulos, A. R. Brown, and A. Pomp, J. Appl. Phys. **80**, 2501 (1996).

[82] R. Ruiz, B. Nickel, N. Koch, L. C. Feldman, R. F. Haglund, A. Kahn, and G. Scoles, Phys. Rev. B **67**, 125406 (2003).

[83] M. Carrara, *Thesis* (École Polytéchnique Fédérale de Lausanne, 2002).

[84] Figure prepared with the assistance of the jmol applet (www.jmol.org).

[85] M. Zinke-Allmang, L. C. Feldman, and M. H. Grabow, Surf. Sci. Rep. **16**, 377 (1992).

[86] A.-L. Barabási and H. E. Stanley, *Fractal Concepts in Surface Growth* (Cambridge University Press, 1995).

[87] W. Ostwald, Z. Phys. Chem. (Leipzig) **34**, 495 (1900).

[88] B. K. Chakraverty, J. Phys. Chem. Solids **28**, 2401 (1967).

[89] S. H. Xin, P. D. Wang, A. Yin, C. Kim, M. Dobrowolska, J. L. Merz, and J. K. Furdyna, Appl. Phys. Lett. **69**, 3884 (1996).

[90] M. Rabe, M. Lowisch, F. Kreller, and F. Henneberger, Phys. Status Solidi B **202**, 817 (1997).

[91] K. Pötschke, L. Müller-Kirsch, R. Heitz, R. L. Sellin, U. W. Pohl, D. Bimberg, N. Zakharov, and P. Werner, Physica E **21**, 606 (2004).

[92] J. Coraux, V. Favre-Nicolin, H. Renevier, M. G. Proietti, B. Amstatt, E. Bellet-Amalric, and B. Daudin, J. Appl. Phys. **101**, 056106 (2007).

[93] J. H. Park, C. H. Kang, Y. J. Kim, Y. S. Lee, and J. S. Choi, Mater. Sci. Eng., C **24**, 27 (2004).

[94] J. H. Lee, S. H. Kim, G. H. Kim, S. C. Lim, H. Lee, J. Jang, and T. Zyung, Mater. Sci. Eng., C **139**, 445 (2003).

[95] P. M. Borsenberger and D. S. Weiss, *Organic Photoreceptors for Imaging Systems* (Marcel Dekker, New York, 1993).

[96] J. Takeya, M. Yamagishi, Y. Tominari, R. Hirahara, Y. N. T. Nishikawa, T. Kawase, T. Shimoda, and S. Ogawa, Appl. Phys. Lett. **90**, 102120 (2007).

[97] R. Ruiz, B. Nickel, N. Koch, L. C. Feldman, R. F. Haglund, A. Kahn, F. Family, and G. Scoles, Phys. Rev. Lett. **91**, 136102 (2003).

[98] S. Pratontep, M. Brinkmann, F. Nüesch, and L. Zuppiroli, Synth. Met. **146**, 387 (2004).

[99] F.-J. M. zu Heringdorf, M. C. Reuter, and R. M. Tromp, Nature **412**, 517 (2001).

[100] T. A. Witten and L. M. Sander, Phys. Rev. Lett. **47**, 1400 (1981).

[101] L. Nony, R. Bennewitz, O. Pfeiffer, E. Gnecco, A. Baratoff, E. Meyer, T. Eguchi, A. Gourdon, and C. Joachim, Nanotechnology **15**, S91 (2004).

[102] M. Eremtchenko, J. A. Schaefer, and F. S. Tautz, Nature **425**, 602 (2003).

[103] S. R. Forrest, P. E. Burrows, E. I. Haskal, and F. F. So, Phys. Rev. B **49**, 11309 (1994).

[104] Y. Hirose, S. R. Forrest, and A. Kahn, Phys. Rev. B **52**, 14040 (1995).

[105] S. R. Forrest and Y. Zhang, Phys. Rev. B **49**, 11297 (1994).

[106] Y. Zhang and S. R. Forrest, Phys. Rev. Lett. **71**, 2765 (1993).

[107] P. Fenter, F. Schreiber, L. Zhou, P. Eisenberger, and S. R. Forrest, Phys. Rev. B **56**, 3046 (1997).

[108] G. Sazaki, T. Fujino, J. T. Sadowski, N. Usami, T. Ujihara, K. Fujiwara, Y. Takahashi, E. Matsubara, T. Sakurai, and K. Nakajima, J. Cryst. Growth **262**, 196 (2004).

[109] R. Hudej, G. Bratina, and M. Onellion, Thin Solid Films **515**, 1424 (2006).

[110] A. C. Mayer, R. Ruiz, H. Zhou, R. L. Headrick, A. Kazimirov, and G. G. Malliaras, Phys. Rev. B **73**, 205307 (2006).

[111] I. Lifshitz and V. Slyozov, J. Phys. Chem. Solids **19**, 35 (1961).

[112] S. Lee, I. Daruka, C. S. Kim, A.-L. Barabási, J. L. Merz, and J. K. Furdyna, Phys. Rev. Lett. **71**, 2765 (1998).

[113] Http://gwyddion.net.

[114] K. N. N. Unni, S. Dabos-Seignon, A. K. Pandey, and J.-M. Nunzi, Solid-State Electron. **52**, 179 (2008).

[115] C. Kim, A. Facchetti, and T. J. Marks, Science **318**, 76 (2007).

[116] T.-S. Huang, Y.-K. Su, , and P.-C. Wang, Appl. Phys. Lett. **91**, 092116 (2007).

[117] S. Lee, B. Koo, J. Shin, E. Lee, , H. Park, and H. Kim, Appl. Phys. Lett. **88**, 162109 (2006).

[118] M. Halik, H. Klauk, U. Zschieschang, T. Kriem, G. Schmid, , W. Radlik, and K. Wussow, Appl. Phys. Lett. **81**, 289 (2002).

[119] M. Daraktchiev, A. von Mühlenen, F. Nüesch, M. Schaer, M. Brinkmann, M.-N. Bussac, and L. Zuppiroli, New J. Phys. **7**, 133 (2005).

[120] F. Dinelli, M. Murgia, P. Levy, M. Cavallini, F. Biscarini, and D. M. de Leeuw, Phys. Rev. Lett. **92**, 116802 (2004).

[121] B. Stadlober, U. Haas, H. Maresch, and A. Haase, Phys. Rev. B **74**, 165302 (2006).

[122] S. E. Fritz, T. W. Kelley, and C. D. Frisbie, J. Phys. Chem. B **109**, 10574 (2005).

[123] D. K. Owens and R. C. Wendt, J. Appl. Polym. Sci. **13**, 1741 (1969).

[124] A. Pietak, S. Korte, E. Tan, A. Downard, and M. P. Staiger, Appl. Surf. Sci. **253**, 3627 (2007).

[125] S. Verlaak, S. Steudel, P. Heremans, D. Janssen, and M. S. Deleuze, Phys. Rev. B **68**, 195409 (2003).

[126] J. Israelachvili, *Intermolecular and Surface Forces* (Academic Press, London, 1992), 2nd ed.

[127] A. D. Carlo, F. Piacenza, A. Bolognesi, B. Stadlober, and H. Maresch, Appl. Phys. Lett. **86**, 263501 (2005).